Spring 2022

DISTRIBUTED FIBER-OPTIC TEMPERATURE SENSORS FOR APPLICATIONS IN THE STEEL INDUSTRY

Muhammad Roman
Missouri University of Science and Technology

Department: Electrical and Computer Engineering

DISTRIBUTED FIBER-OPTIC TEMPERATURE SENSORS FOR APPLICATIONS IN THE STEEL INDUSTRY

by

MUHAMMAD ROMAN

A DISSERTATION

Presented to the Graduate Faculty of the

MISSOURI UNIVERSITY OF SCIENCE AND TECHNOLOGY

In Partial Fulfillment of the Requirements for the Degree

DOCTOR OF PHILOSOPHY

in

ELECTRICAL ENGINEERING

2022

Approved by:

Dr. Jie Huang, Advisor
Dr. Steve Watkins
Dr. Jun Fan
Dr. Ronald O'Malley
Dr. Laura Bartlett

PUBLICATION DISSERTATION OPTION

This dissertation consists of the following three articles, formatted in the style used by the Missouri University of Science and Technology:

Paper I, found on pages 9–46, has been published in *Sensors*.

Paper II, found on pages 47–75, has been published in *IEEE Sensors Journal.*

Paper III, found on pages 76–105, has been published in *IEEE Transactions on Instrumentation and Measurement.*

ABSTRACT

Steelmaking facilities require continuous temperature measurements throughout the manufacturing process to ensure consistent product quality and high productivity. Motivated by the limitations of conventional temperature sensors, distributed fiber-optic sensors (DFOS) were developed and deployed for various applications in the steel industry. Fiber-optic sensors offer various advantages over conventional sensors, such as the miniaturized size of the optical fiber, immunity to electromagnetic interferences, capability for multiplexing and distributed sensing, and the ability to withstand harsh environments.

Firstly, high-resolution Rayleigh backscattering-based DFOS were demonstrated as potential solutions for temperature measurements in steelmaking processes by performing experimental simulations. Additionally, aluminum casting experiments were conducted to demonstrate the measurement capability of DFOS in solidifying metal alloys. Temperatures exceeding 700 °C were measured at sub-millimeter spatial resolution (~ 0.65 mm) and at milliseconds sampling speeds. Moreover, a novel dip testing paddle was developed employing a copper mold instrumented with optical fiber. The instrumented mold was used to perform steel dip tests in a 200 lb induction furnace in a foundry laboratory. The results obtained from temperature measurements provided strong evidence that the dip testing paddle can be a useful apparatus for the investigation of the fundamental reactions occurring in a continuous casting mold. The present study demonstrated that DFOS can be transformative to the steel industry by enabling efficient process control, reducing energy and maintenance costs, improving the safety of equipment and workers, and enhancing the quality and yield of metal products.

ACKNOWLEDGMENTS

I am thankful to my advisor, Dr. Jie Huang, for his kindness, inspiration, guidance, and encouragement throughout my doctoral studies. I want to express my deepest gratitude to Dr. Rex Gerald for his relentless support and mentorship. I owe a great deal of thanks to Dr. Ronald O'Malley for his supervision throughout my research endeavor. I'm grateful to Dr. Laura Bartlett for her support and guidance. I would also like to thank my committee members, Dr. Steve Watkins and Dr. Jun Fan, for providing their time and feedback during my research. To my fellow graduate student and project collaborator, Damilola Balogun, thank you so much for your contribution. I enjoyed working with you. My gratitude also goes to fellow graduate students/lab members: Wassana, Dinesh, Chen, Yiyang, Bohong, Collins, Arik, Deva, and Hanok. I'm thankful to all the members of Lightwave Technology Laboratory and Peaslee Steel Manufacturing Research Center (PSMRC) for their help. I'm indebted to my family and friends for their endless support during my academic pursuit.

Finally, I appreciate the sponsors of the project: Peaslee Steel Manufacturing Research Center (PSMRC) at Missouri S&T, Leonard Wood Institute, and the U.S. Army Research Laboratory.

TABLE OF CONTENTS

Page

LIST OF ILLUSTRATIONS

PAPER I Page

PAPER III

LIST OF TABLES

PAPER II Page

1. INTRODUCTION

1.1. BACKGROUND

Temperature measurement is an integral part of steelmaking processes. Real-time temperature measurements provide data that can be used to optimize energy usage across various steelmaking facilities. A few examples of steel industry equipment that can benefit greatly from continuous temperature measurements include furnace, ladle, tundish, continuous casting mold, and rolling mill. Temperature monitoring in the furnace, ladle, and tundish linings provides data that can be used to detect refractory wear and reduce heat losses. Temperature monitoring in the ladle linings can be useful for improving the ladle preheating process. Improvements in the ladle preheating process can significantly reduce tap temperatures in steel foundries. Reductions in tap temperatures can save a huge amount of energy. Energy optimization of steelmaking processes can significantly lower operating costs. Temperature monitoring is also important to achieve consistent product quality and high productivity. Various operating faults and quality defects can be detected by continuous temperature monitoring. Temperature measurements in rolling mills help to control surface temperature and shape, thereby ensuring product quality. Temperature measurements in the tundish provide feedback to control temperature variations of the steel, to ensure a stable caster operation in the continuous casting of steel. A mold instrumented with a temperature measurement system deployed in a continuous casting process provides data that can be used to detect crack formations in the solidifying shell, avoid breakouts, and provide the opportunity to monitor and control heat transfer during solidification. Temperature measurements enable the use of advanced control strategies

which can improve operating stability, efficiency, and product yield. These improvements result in large energy cost savings. According to the American Iron and Steel Institute (AISI), approximately 88 million tons of steel was produced in the United States in 2016, with a weighted average energy intensity of approximately 18 MBTU/ton [1]. The U.S. steel industry can save 600 million dollars per year by achieving a 10% improvement in energy efficiency. The world's largest steel producer, ArcelorMittal, reported that 0.2% savings in yield, achieved by reducing defects, is equivalent to savings of 90 million dollars per year for the U.S. steel industry. The 0.2% savings in yield can also save 2.68 PJ energy per year, which is sufficient to power ~ 70,000 American houses for the entire year [2].

Owing to the significance of continuous temperature measurements in steelmaking processes, an accurate, information-rich, fast, and minimally invasive temperature measurement system is highly desirable. Conventionally, thermocouples are used to perform temperature measurements in steelmaking processes [3–7]. However, the inability of thermocouples to easily perform distributed temperature measurements limits their utility in many important applications. Thermocouples are also affected by electromagnetic interferences. The measurements from thermocouples are also affected by electromagnetic systems, such as electromagnetic braking and stirring used for flow control in the continuous casting process. Infrared (IR) cameras are also employed for thermal mapping in various steelmaking settings [8, 9]. However, the target surface is not always accessible to IR cameras. Moreover, the measurement accuracy of IR cameras is also affected by variations in the emissivity of the target surface. Due to the limitations of existing sensing technologies, fiber-optic sensors were explored for various steelmaking applications.

In recent years, fiber-optic sensors made their way into various fields including structural health monitoring [10–12], chemicals [13–15], aerospace [16–18], military [19, 20], medical [21–23], etc. The increasing popularity of fiber-optic sensors is attributed to their advantages over conventional electronic sensors. The advantages of fiber optic sensors over conventional sensors include the miniaturized size of the optical fiber, low thermal capacity, immunity to electromagnetic interferences, little intrusion into the system, capability for multiplexing and distributed sensing, and the ability to withstand harsh environments. Fiber-optic sensors achieved modest commercial success, with high price being a deterrent in their market growth. Fiber-optic sensors are fairly expensive compared to conventional sensors. However, fiber-optic sensors are making headway in areas where the capabilities of fiber-optic sensors cannot be replicated by conventional sensors. For example, fiber-optic sensors are becoming increasingly popular in biomedical applications because of their biocompatible nature [21, 22]. The small size and chemically inert nature of optical fibers pose less risk to the human body compared to conventional invasive biomedical sensors. Structural health monitoring is another area where fiber optic sensors are growing rapidly. The miniaturized size of optical fiber, immunity to electromagnetic interferences, and the capability for distributed measurements over distances of several kilometers are some of the key advantages of fiber optic sensors which are highly desirable for structural health monitoring. Fiber optic sensors have been successfully deployed in structures like dams, bridges, and tunnels for measuring various structural properties and deformations such as inclination, cracks, and corrosion [11, 12]. Similarly, distributed sensing capability of fiber-optic sensors makes them a very exciting prospect in steelmaking applications. Temperatures in most of the steelmaking processes

are spatially distributed while thermocouples can only afford single-point measurements. The mismatch of applications' requirements and sensors' capabilities motivated steelmakers to seek alternative sensing technologies, such as fiber-optic sensing. The fiber optic sensors are capable of providing spatially continuous temperature measurements along the length of optical fibers. Understanding temperature profiles in steelmaking processes can improve process control, reduce energy and maintenance costs, and improve the quality and productivity of castings. The information-rich measurement capability of fiber-optic sensors could provide the basis for their commercial success in the steelmaking industry.

1.2. DISTRIBUTED FIBER-OPTIC SENSORS

A variety of fiber-optic sensors have been reported for temperature measurements that provide either point, quasi-distributed, or fully distributed measurements. Interferometers are the most commonly employed fiber-optic sensors for single-point temperature measurements [24–26]. Various configurations of interferometers include Fabry-Perot [24], Michelson [27], Mach-Zehnder [28], and Sagnac [29]. Some of the key characteristics of interferometers are small size, simple fabrication, high sensitivity, high resolution, and fast response time. However, single-point interferometers are not suited for applications that require distributed measurements. Fiber Bragg gratings (FBGs) are the most widely used quasi-distributed fiber-optic sensors for temperature measurements [30–32]. An FBG is fabricated by creating index modifications in the core of an optical fiber. The enormous developments in the fabrication methods of FBGs enabled the mass production of FBGs, and hence paved the way for their commercial success. FBGs attracted

considerable interest for various industrial applications due to quasi-distributed sensing capability with a reasonable spatial resolution (~1 cm), high temperature resolution (~0.1 °C), and fast measurement rates (up to a few kHz). FBGs have been deployed in some commercial mold monitoring systems in the steelmaking industry [33–36]. However, various applications in steelmaking require spatially continuous measurements. FBGs are less suited for such applications due to measurement dead zones along optical fibers that contain FBGs.

Contrary to the interferometers and FBGs where optical fibers are modified to create sensors, the fully distributed fiber-optic sensors (DFOS) are based on light scattering in unaltered optical fibers. Raman, Brillouin, and Rayleigh are the three types of scattering in optical fibers that are exploited to achieve fully distributed sensing. DFOS are commonly interrogated using optical time-domain and frequency-domain reflectometry techniques [37–39]. The sensors based on Raman and Brillouin optical time-domain reflectometry (OTDR) offer an extended sensing range (kilometers). Due to the extended range of the sensors, Raman and Brillouin OTDR systems have been successfully used for temperature and strain measurements in large structures, such as dams and bridges. However, the spatial resolution of the aforementioned sensors is of the order of one meter, which is not suitable for applications in steelmaking that require thermal mapping in compact structures.

In contrast to Raman and Brillouin OTDR systems, Rayleigh optical frequency-domain reflectometry (OFDR) systems provide much higher spatial resolution (sub-millimeter) [40–42]. The working principle of the Rayleigh OFDR system is based on acquiring and interpreting RBS signals from single-mode optical fibers. Optical fibers have intrinsic in-homogeneities in their material that give rise to microscopic fluctuations in the

refractive index profile. The light scattered from in-homogeneities in the core of a single-mode optical fiber results in a unique Rayleigh signature for the fiber. The unique and stable Rayleigh signature in a single-mode optical fiber, under steady-state conditions, is the basis for RBS-based sensing. Temperature variations cause changes in both the refractive index and the length of an optical fiber, which result in shifts in the RBS spectra. Changes in temperature can be measured by measuring shifts in RBS spectra. The reference RBS signals from the fibers under test are recorded, employing the interrogation technique of OFDR, after the fiber placement in the test setup at room temperature. Rayleigh signals at elevated temperatures are compared (using cross-correlation) with the reference signals to obtain spectrum shift measurements, which are then converted to temperature measurements using temperature coefficients. Rayleigh OFDR systems provide temperature measurements along optical fibers at sub-millimeter spatial resolution over distances of up to a few tens of meters. The high spatial resolution (~0.5 mm), fast measurement rates (a few hundred Hz), and a reasonable sensing length of optical fiber (a few tens of meters) make Rayleigh backscattering-based (RBS-based) DFOS a very promising prospect for applications in the steel industry.

1.3. CURRENT ACHIEVEMENTS

Recently, we investigated, developed, and deployed RBS-based DFOS for various applications in the steel industry [43-45]. We performed metal casting experiments with embedded sensors and measured temperature profiles in the mold walls and castings during metal solidification. The results obtained from the temperature measurements provided

useful insights into the solidification behaviors of metals, which otherwise were not achievable.

Moreover, we investigated that the single-mode optical fiber, commonly employed in RBS-based OFDR systems, is not suitable for thermal mapping in compact structures due to high bending loss of the fiber and low signal-to-noise ratio (SNR) of the measurements. We employed a thin-core high-numerical aperture (TC-HNA) optical fiber in an RBS-based OFDR system to improve the SNR of the measurements. We also investigated and demonstrated the high bending loss-resistance of the proposed TC-HNA [46]. We demonstrated, through a series of experiments, that the high SNR and low bending loss of the TC-HNA could extend the range of RBS-based measurements to compact structures where sharp bending of the test optical fiber is unavoidable.

Furthermore, we developed a novel dip testing paddle employing a compact copper mold plate [47]. The mold was instrumented using a single continuous TC-HNA fiber for temperature measurements. We devised an instrumentation technique that provided good thermal contact of embedded optical fibers with the hotface of the mold plate and eliminated thermally induced strains. The embedding technique also ensured that optical fiber was protected from direct exposure to molten metal. The dip testing apparatus was designed to perform steel dip tests in a 200 lb induction furnace in a foundry laboratory. We successfully performed dip tests for different steel compositions and generated thermal maps of the mold plate during immersion and solidification. The thermal maps of the mold, combined with thickness maps of the solidified shells, were used to study the solidification behavior of various steel grades [48]. The dip testing paddle can be a useful apparatus for the investigation of the fundamental reactions occurring in a continuous casting mold. The

present study demonstrated that DFOS can be transformative to the steel industry by enabling efficient process control, reducing energy and maintenance costs, improving the safety of equipment and workers, and enhancing the quality and yield of metal products.

PAPER

I. A SPATIALLY DISTRIBUTED FIBER-OPTIC TEMPERATURE SENSOR FOR APPLICATIONS IN THE STEEL INDUSTRY

Muhammad Roman [1], Damilola Balogun [2], Yiyang Zhuang [1], Rex E. Gerald, II [1], Laura Bartlett [2], Ronald J. O'Malley [2], and Jie Huang [1, *]

[1]Department of Electrical and Computer Engineering, Missouri University of Science and Technology, Rolla, MO 65409, USA; mrhmc@mst.edu (M.R.); yz8r4@mst.edu (Y.Z.); geraldr@mst.edu (R.E.G.)

[2]Department of Material Science and Engineering, Missouri University of Science and Technology, Rolla, MO 65409, USA; dsbcrh@mst.edu (D.B.); lnmkvf@mst.edu (L.B.); omalleyr@mst.edu (R.J.O.)

*****Correspondence: jieh@mst.edu; Tel.: +1-573-341-4836

ABSTRACT

This paper presents a spatially distributed fiber-optic sensor system designed for demanding applications, like temperature measurements in the steel industry. The sensor system employed optical frequency domain reflectometry (OFDR) to interrogate Rayleigh backscattering signals in single-mode optical fibers. Temperature measurements employing the OFDR system were compared with conventional thermocouple measurements, accentuating the spatially distributed sensing capability of the fiber-optic system. Experiments were designed and conducted to test the spatial thermal mapping capability of the fiber-optic temperature measurement system. Experimental simulations provided evidence that the optical fiber system could resolve closely spaced temperature features, due to the high spatial resolution and fast measurement rates of the OFDR system.

The ability of the fiber-optic system to perform temperature measurements in a metal casting was tested by monitoring aluminum solidification in a sand mold. The optical fiber, encased in a stainless-steel tube, survived both mechanically and optically at temperatures exceeding 700 °C. The ability to distinguish between closely spaced temperature features that generate information-rich thermal maps opens up many applications in the steel industry.

Keywords: temperature sensor; Rayleigh scattering; optical frequency domain reflectometry; distributed sensing; optical fiber; peritectic behavior; metal casting; aluminum alloy

1. INTRODUCTION

Steelmaking facilities require continuous temperature measurements throughout the manufacturing process, to ensure consistent product quality and high productivity. Real-time temperature monitoring in processes like furnace reheating, furnace annealing, continuous casting, rolling, and hot forming enables the use of advanced control strategies and provide process control feedback for the aforementioned processes. Temperature measurements in rolling mills help to control surface temperature and shape, thereby ensuring product quality. Temperature measurements in the tundish provide feedback to control temperature variations of the steel, to ensure a stable caster operation in the continuous casting of steel. A mold instrumented with a temperature measurement system deployed in a continuous casting process provides data that can be used to detect crack

formations in the solidifying shell, avoid breakouts, and provides the opportunity to monitor and control heat transfer during solidification.

In addition to the quality assurance of various metal products, temperature measurements are also a means of detecting process faults, to ensure the safety of equipment and workers. Temperature monitoring of material transfer conveyors can mitigate safety risks. Monitoring temperature in the refractory linings can help detect hot spots caused by refractory failures, to avoid catastrophic breakouts, thus enabling timely maintenance.

Monitoring temperature also leads to cost-effective production by providing more control over energy expenditures and providing the means for improving production efficiency. Processes like furnace annealing and reheating can benefit greatly from continuously monitoring temperatures at high spatial resolution.

Owing to the significance of continuous temperature measurements in steelmaking, an accurate, information-rich, fast, and minimally invasive temperature measurement system is highly desirable. A measurement system with such characteristics would be helpful in achieving safe and cost-effective steelmaking with good product quality and high productivity. Temperature measurements in steel industry applications are commonly performed with thermocouples [1–4]. Thermocouples provide reliable and fast temperature measurements with good accuracy and high-temperature resolution; however, they have several limitations. For instance, thermocouples provide single-point measurements, which make them less suited for applications that exhibit closely spaced temperature features. Therefore, the inability of thermocouples to easily perform distributed temperature measurements limits their utility in many important applications. Temperature mapping

using multiple thermocouples makes the system cumbersome, due to the large number of lead wires needed to interrogate them. Moreover, the size of the thermocouple probe often requires a significant modification to the device being measured, possibly interfering with the desired measurement or compromising the structural integrity of the device. Thermocouples, due to their electrical conducting nature, are also affected by electromagnetic interference in applications that involve electromagnetic phenomena, such as magnetic stirrers, arc furnaces, and radiofrequency transmitters.

The aforementioned limitations of thermocouples motivated researchers to seek alternative sensing technologies. In this quest, fiber-optic sensing technologies were explored as potential solutions for temperature measurements. Optical fiber technologies have emerged as promising sensing solutions, due to the miniaturized size of the optical waveguide, immunity to electromagnetic interferences, and ability to withstand harsh environments. In addition, optical fibers afford the innate capability for distributed sensing [5]. Several optical fiber-based sensors for temperature measurements were reported. Fiber-optic interferometers are commonly exploited for temperature measurements [6]. Interferometers offer high sensitivity and good temperature resolution, but they can only provide point measurements, similar to thermocouples. Fiber-optic distributed temperature sensors based on optical time-domain reflectometry (OTDR) are widely studied [7–10]. These OTDR-based sensors offer a spatial resolution of the order of a few meters, which is not suitable for steel industry applications due to the closely spaced temperature features in the steelmaking processes. Fiber Bragg gratings (FBGs) are also used for distributed temperature sensing [11–14]. FBGs attracted considerable interest in the steelmaking industry, due to a quasi-distributed sensing capability with a reasonable spatial resolution

(~1 cm), high-temperature sensitivity (~10 pm/°C), and a fast measurement rate (~5 kHz). Thomas and Okelman reported results using a casting mold with embedded FBG sensors for temperature and strain measurements [15]. The FBG sensors were embedded in a copper mold, using a nickel electroplating process. Temperature variations were recorded 1 mm away from the hotface, in a laboratory simulation of the continuous casting process. Lieftucht et al. developed a mold embedded with FBGs for temperature measurements in a continuous casting process of steel [16]. Temperature profiles were used to calculate mold levels and local heat flux readings. Spierings et al. designed a mold by embedding FBGs in the upper half of a copper mold plate with 2660 temperature measurement points [17]. The instrumented mold was tested on different steel grades. Temperature measurements were used to observe fluid flow and mold thermal behavior. Currently, there are several companies offering commercial systems for thermal monitoring of a mold, based on fiber Bragg gratings.

Although FBGs offer better spatial resolution than OTDR, they have other limitations. For example, FBGs are not truly distributed and they only afford quasi-distributed sensing. Moreover, FBGs require modifications to single-mode fibers to create the gratings, which add to the cost of the fiber. Another known disadvantage of FBGs is their inability to withstand temperatures exceeding 700 °C, as the gratings are erased at elevated temperatures. Optical frequency domain reflectometry (OFDR) based on Rayleigh scattering is another fiber-optic distributed sensing solution [18–22]. OFDR systems employ un-modified single-mode optical fibers as sensor devices. Moreover, OFDR systems offer spatial resolution in the range of submillimeter to a few millimeters, with fast measurement rates. The distributed sensing capability with a high spatial resolution and

fast update rates (few hundred Hz) make OFDR an exciting prospect for the characterization of phenomena that involve closely spaced static and transient temperature features. Various fiber-optic distributed temperature sensors, based on the OFDR technology, were reported [23–26]. Yan et al. reported Rayleigh scattering-based fiber-optic sensors for real-time temperature monitoring of solid oxide fuel cells [24]. The spatially distributed temperature measurements were performed at up to 800 °C, with a 5-mm spatial resolution. Boyd et al. demonstrated a Rayleigh scattering-based fiber-optic sensor system to monitor distributed temperatures, along superconducting degaussing cables, in cryogenic environments [25]. Temperature measurements were performed along a 10 m long optical fiber, with a 7-mm spatial resolution.

In this work, spatially distributed fiber-optic temperature sensors based on Rayleigh scattering are proposed for applications in the steel industry. The temperature measurements can be performed along optical fibers, over distances of up to 50 m. The proposed sensor system can perform spatially distributed temperature measurements at up to 750 °C. Although the temperatures in some steelmaking processes can exceed 1600 °C, there are several applications in the steel industry where the maximum temperature is well below the maximum temperature measurement capability of the proposed system. One such example for a steel industry application is temperature measurements in a continuous caster mold. The studies reported in [15–17] showed that the temperatures inside the copper molds used in the continuous casting of steel are well below 500 °C. The maximum measurable temperature of the proposed sensor system is limited by the degradation of the Rayleigh backscattering signals at elevated temperatures. It was demonstrated in [27,28] that Rayleigh scattering-based sensing using the standard single-mode fiber could be used

for temperature measurements of up to 750 °C. As the system temperature approached 750 °C, the Rayleigh backscattering signals degraded, possibly due to the increased mobility of the intrinsic defects in the optical fiber material. Another study demonstrated that the temperature measurement range of the Rayleigh scattering-based sensor system could be extended to 850 °C, using gold-coated single-mode fibers [29].

In this work, OFDR systems were employed to perform fiber-optic distributed temperature measurements. The fiber-optic temperature measurements were compared with conventional thermocouple measurements, validating the accuracy of the former and manifesting its distributed sensing capability. Moreover, experiments were designed and conducted to provide evidence that Rayleigh scattering-based fiber-optic temperature sensors, due to the high spatial resolution and the fast measurement rates of OFDR systems, are suitable candidates for thermal mapping of phenomena that involve closely spaced temperature features. The measurement capability and survivability of a fiber-optic temperature sensor in a metal casting was also tested. The temperature profile across the cavity of a sand mold was monitored during an aluminum pour and solidification. The experimental results showed that the distributed fiber-optic temperature sensor could be a potential candidate for temperature measurements in metal casting applications.

2. SENSING PRINCIPLE AND INTERROGATION SYSTEM

2.1. RAYLEIGH-SCATTERING-BASED TEMPERATURE MEASUREMENTS

The proposed system of distributed temperature measurements is based on Rayleigh scattering in a single-mode optical fiber. Rayleigh scattering originates when

light strikes an inhomogeneity in a continuum of matter, with dimensions smaller than the wavelength of light. In an optical fiber, random fluctuations in the refractive index of the optical fiber material (glass) cause Rayleigh scattering. Temperature variations cause changes in both the refractive index and the length of the optical fiber, which result in shifts in the Rayleigh backscattering (RBS) spectra. The RBS shift Δλ caused by a temperature change ΔT can be expressed as:

$$\frac{\Delta\lambda}{\lambda} = (\alpha + \xi)\Delta T \quad (1)$$

where α is the thermal expansion coefficient and ξ is the thermo-optic coefficient of the optical fiber material. The value of the thermal expansion coefficient is 0.55 × 10–6 /°C, while that of the thermo-optic coefficient is 8.5×10^{-6} /°C. As the value of the thermal expansion coefficient is approximately an order of magnitude smaller than the thermo-optic coefficient, the spectrum shift due to a temperature change is usually attributed to the change in the refractive index.

2.2. OPTICAL FREQUENCY DOMAIN REFLECTOMETRY

An OFDR interrogator system was used to acquire, process, and analyze backscattered light. In an OFDR system, light from a tunable laser source was launched into an optical fiber network containing an interferometer. The interference signal from the interferometer was detected and analyzed. As shown in the schematic of the OFDR system we developed in our laboratory (Figure 1), light from a tunable laser source (LUNA PHOENIXTM 1200) with a 50 nm tuning range (1515 nm–1565 nm) and a 1000 nm/s tuning speed was launched into an optical fiber network. The first coupler split the incident light between the two arms—one beam going into an auxiliary interferometer and the other

beam going into the main interferometer. The auxiliary interferometer was used as a clock generator for the data acquisition card, in order to compensate for the nonlinear sweep of the laser. The main interferometer was a Mach-Zehnder interferometer with two arms, one used as a reference arm and the other as a sensing arm. Backscattered light from the sensing arm combined with the reference signal in a 50–50 coupler and generated an interference signal, which was collected by a data acquisition card and then transmitted to a computer. Temperatures metered along the longitudinal spatial dimension of the optical fiber were retrieved through a series of signal processing steps.

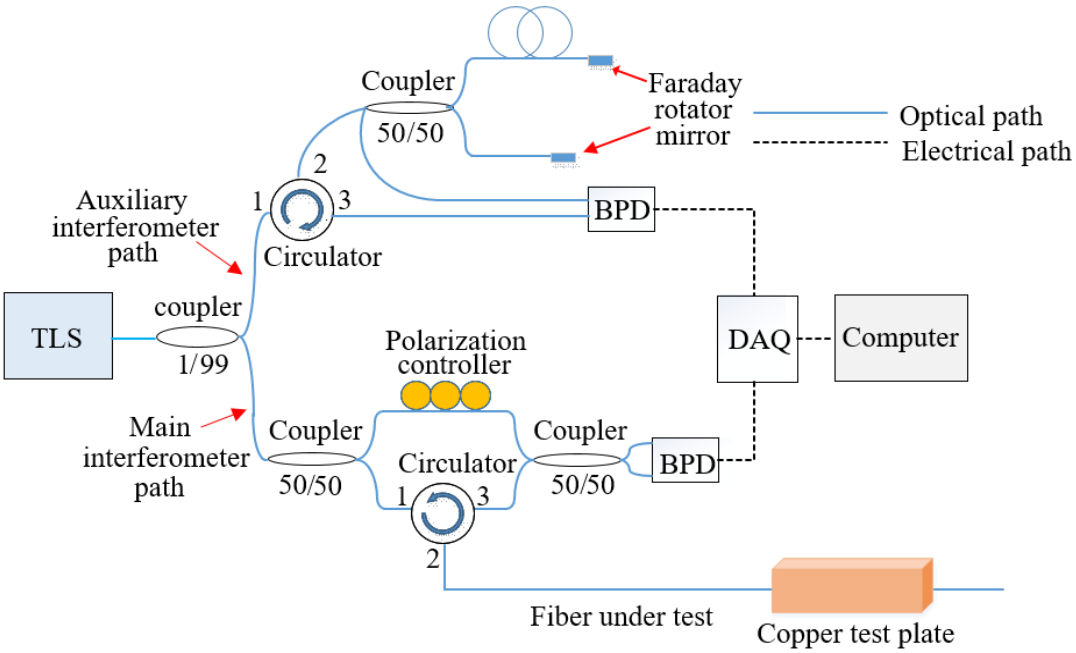

Figure 1. A schematic diagram of the optical frequency domain reflectometry system. TLS—tunable laser source, BPD—balanced photodetector, and DAQ—data acquisition card.

3. DISTRIBUTED TEMPERATURE SENSING EXPERIMENTS

The purpose of this project was to develop a fiber-optic distributed temperature sensor system for applications in the steel industry. Preliminary tests were performed to demonstrate the distributed sensing capability of the fiber-optic temperature measurement system. In many such experiments, optical fibers were nested in metal tubes. Metal tubes were used as potential casings, anticipating the deployment of optical fibers in the steel industry processes. Moreover, to validate the accuracy of the Rayleigh-scattering-based fiber-optic temperature sensor, fiber-optic temperature measurements were compared with thermocouple measurements. As discussed earlier, the capability of distributed temperature measurement with high spatial resolution could be very useful for applications in the steel industry. The high spatial resolution of the sensing system makes it possible to measure localized temperature features. The ability to measure spatial variations in temperature adds great value for applications in the steel industry. Control experiments were performed to map closely spaced fluctuating temperature features. The closely spaced temperature variations were achieved by heating the test objects. The test objects were created by machining an air cavity into a copper plate. The copper plates were used as test objects due to their resemblance to copper molds, used in continuous steel casting. Results obtained from the thermal mapping experiments provided initial evidence that the fiber-optic system had the ability to distinguish between closely spaced temperature features. Furthermore, an aluminum solidification experiment was conducted to demonstrate the measurement capability and survivability of optical fibers in metal casting applications.

3.1. OPTICAL FIBER ENCASED IN A COPPER TUBE EQUIPPED WITH HEATING COILS

A test experiment for distributed temperature measurements was performed by placing a single-mode optical fiber (o.d. = 250 μm) in a 0.8 m long copper tube (i.d. = 660 μm; o.d. = 1800 μm), as shown in Figure 2. The optical fiber was connected to the OFDR interrogator. Three heating elements, connected to a DC power supply, were used to locally heat three distinct regions of the copper tube. The heating elements used in the experiment were nichrome resistance wires. The heating elements were simultaneously powered by a DC power supply (Agilent E3616A), drawing approximately 1 A of current at a voltage of 15 V. When the power was turned on, the temperatures recorded by the fiber-optic system increased with an average ramp-up rate of 10–11 °C/min for the heating elements, before reaching a steady-state temperature profile. Temperature gradients were generated along the copper tube, due to the interplay between the heat generated by the heating elements and the radiation heat loss to the ambient environment. Distributed (longitudinal) temperature profiles along the optical fiber nested in the copper tube were recorded with a measurement period of 10 s, throughout the electric heating process.

The temperature distribution along the optical fiber encased in the copper tube revealed three distinct regions of elevated temperatures in the center sections and lower temperatures at the end sections of the copper tube, as shown in Figure 3. At any one point along the copper tube, temperature measurements were made with a temperature measurement resolution of ±1 °C. Temperature measurements were recorded every 5 mm, along the length of the copper tube.

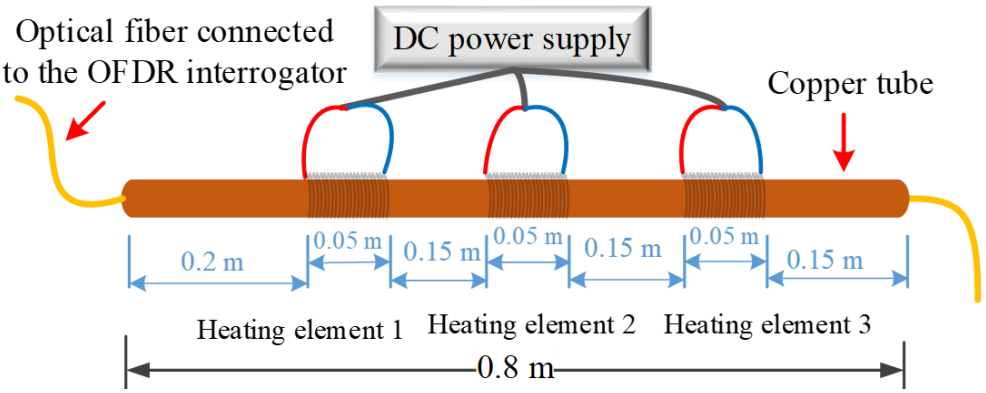

Figure 2. A schematic diagram of the optical frequency domain reflectometry (OFDR) system setup used for the distributed temperature measurements. The copper tube-encased optical fiber was connected to the OFDR interrogator. Three heating coils were used to create temperature gradients along the length of the copper tube.

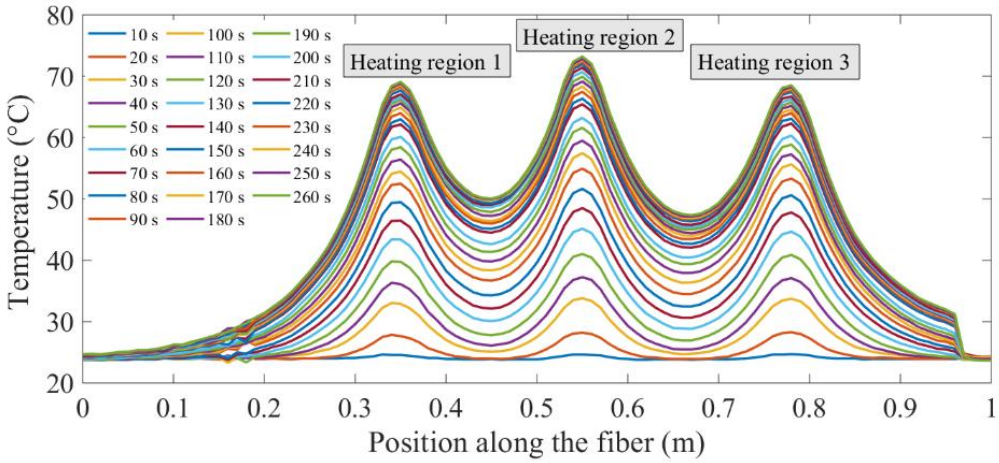

Figure 3. Spatial (longitudinal) temperature profile along the length of an optical fiber nested in a copper tube. Three peak temperature regions correspond to the location of the three heating coils placed along the length of the copper tube. A spatial temperature profile was recorded every 10 s during heating.

3.2. COMPARISON OF FIBER-OPTIC TEMPERATURE MEASUREMENT SYSTEM WITH THERMOCOUPLES

After demonstrating the spatially-distributed sensing capability of the optical fiber sensor and interrogator system, experiments were carried out to compare fiber-optic

temperature measurements with thermocouple measurements. In one of the experiments, an optical fiber (o.d. = 0.25 mm) was placed inside a 100-mm long steel tube (i.d. = 2 mm; o.d. = 3 mm), and a 40-mm long heating coil was used to heat the steel tube, as shown in Figure 4. A K-type thermocouple (probe diameter = 0.5 mm), connected to a data logger (Graphtec GL220), was placed inside the tube and positioned at the center location of the heating element, as shown in Figure 4a. The heating coil was powered by a DC power supply (Mastech HY3005D). Three temperature ramp-up experiments were performed to compare the temporal temperature profiles of fiber-optic and the thermocouple measurements. In the first experiment, when the power was turned on, the temperature increased with an average ramp-up rate of 84 °C/min, before reaching a steady-state temperature of 400 °C in 4.5 min. Temperature readings from both the fiber-optic and the thermocouple systems were recorded simultaneously at a measurement rate of one sample per second. Both the fiber-optic and the thermocouple systems performed temperature measurements with a resolution of less than ±1 °C. As discussed earlier, the maximum temperature measurement capability of the developed fiber-optic system was ~750 °C. The thermocouple system, on the other hand, could be used for temperature measurements of up to 1300 °C. Since the fiber-optic system provided distributed measurements along the length of the fiber, a single position on the optical fiber that was closest to the thermocouple was selected to compare the fiber-optic measurements with the thermocouple measurements. The position on the optical fiber, closest to the tip of the thermocouple probe, was identified using localized point heating, before the start of the experiment. The comparison of temperature measurements from both systems, over time, is shown in Figure 4b. The results demonstrated good agreement between the fiber-optic and thermocouple

temperature measurements. The differences in temperature readings between the fiber-optic and the thermocouple systems at the early stages of the heating experiment, as depicted in Figure 4b, were due to the relative position of the thermocouple junction, with respect to the optical fiber inside the tube. However, both systems registered similar temperatures when the steady-state was reached, where a constant temperature was maintained inside the tube. The experiment was repeated an additional two times, with average ramp-up rates of 82 °C/min and 356 °C/min, respectively. The results from the experiments are shown in Figure 4c,d. The results demonstrated good agreement between the fiber-optic and thermocouple temperature measurements. In addition to the difference in the spatial positions of both sensors, temperature readings recorded with both systems could be different due to the different thermal responses of the optical fiber and the thermocouple probes. During the heating process, the fiber-optic system registered slightly lower temperatures than the thermocouple system, as evident from Figure 4b–d. The temperature differences between the two sensors, shown in the inset plots in Figure 4b–d, might be due to the fact that the thermal conductivity of the optical fiber was lower than that of the thermocouple. Therefore, the thermocouple responded more quickly to the changes in temperatures. More detailed work needs to be done to improve the apparatus used to compare fiber-optic with thermocouple measurements.

As discussed earlier, the inability of single-point thermocouples to perform distributed temperature measurements limits their application. This limitation was illustrated in an experiment where a spatial temperature profile obtained from a single continuous optical fiber nested in a metal tube was compared with a discrete spatial

temperature profile that resulted from sequentially moving a thermocouple along the length of the same tube-encased fiber, as shown in Figure 5.

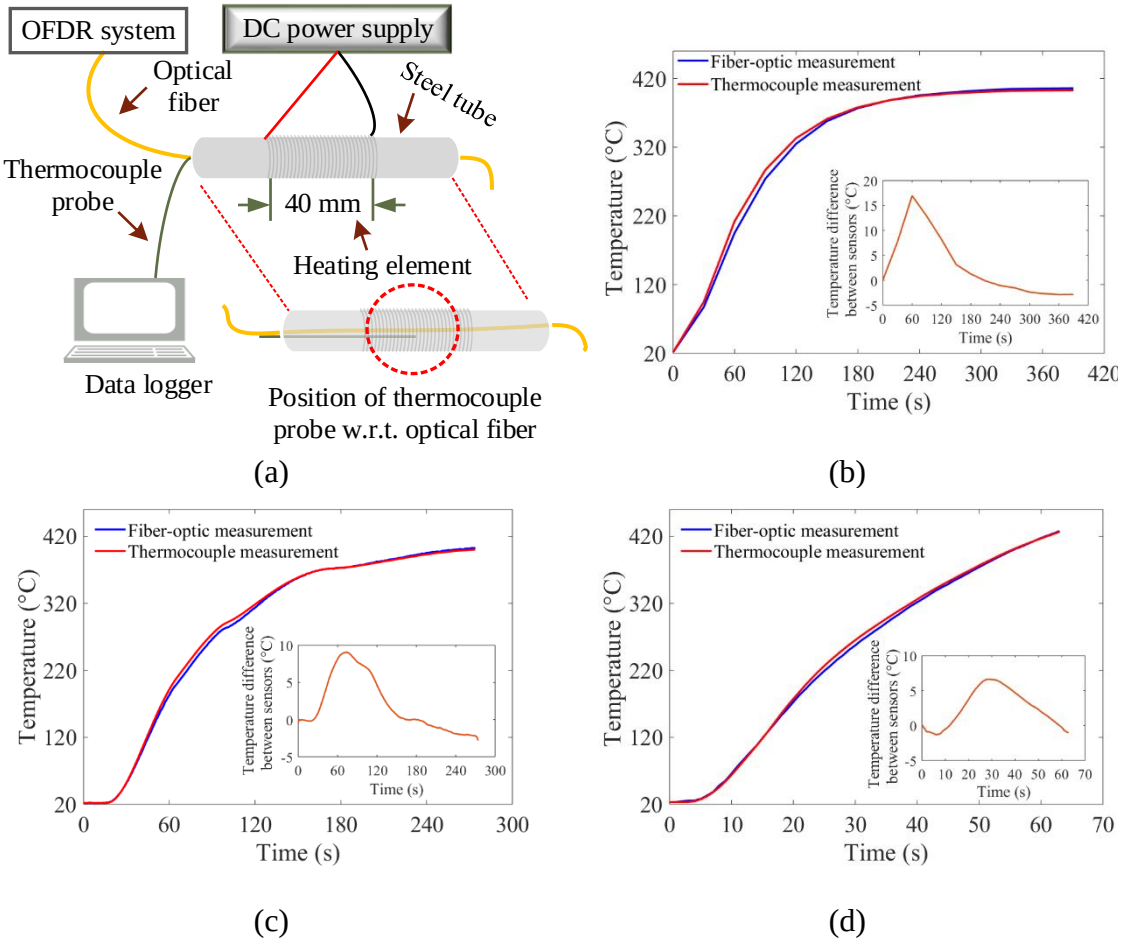

Figure 4. Test apparatus and single-point temperature measurement comparisons from fiber-optic and thermocouple measurements for a temperature-ramp experiment. (a) A schematic of the experimental setup used to compare fiber-optic with thermocouple measurements. The thermocouple junction was placed at the center of the heating coil. The corresponding position of the optical fiber was identified using localized point heating. (b) Temporal temperature profiles of fiber-optic and the thermocouple measurements. The setup was heated with an average ramp-up rate of 84 °C/min. The inset plot shows temperature differences between the two sensors over time. (c) Temporal temperature profiles of fiber-optic and thermocouple measurements. The setup was heated with an average ramp-up rate of 82 °C/min. (d) Temporal temperature profiles of fiber-optic and thermocouple measurements. The setup was heated with an average ramp-up rate of 356 °C/min.

In order to measure a spatial temperature profile using a conventional thermocouple, a sheathed K-type thermocouple was re-positioned from one end of the tube to the other in 1-cm steps, as illustrated in Figure 5a. The thermocouple readings, recorded under steady-state conditions, were compared with the corresponding fiber-optic temperature measurements. The two sets of temperature measurements were separated by small and variable temperature offsets, as shown in Figure 5b. Since the thermocouple probe was manually moved and re-positioned inside the tube, it was difficult to ensure that the corresponding position on the optical fiber was exactly the same as the location where the thermocouple junction (probe tip) was positioned.

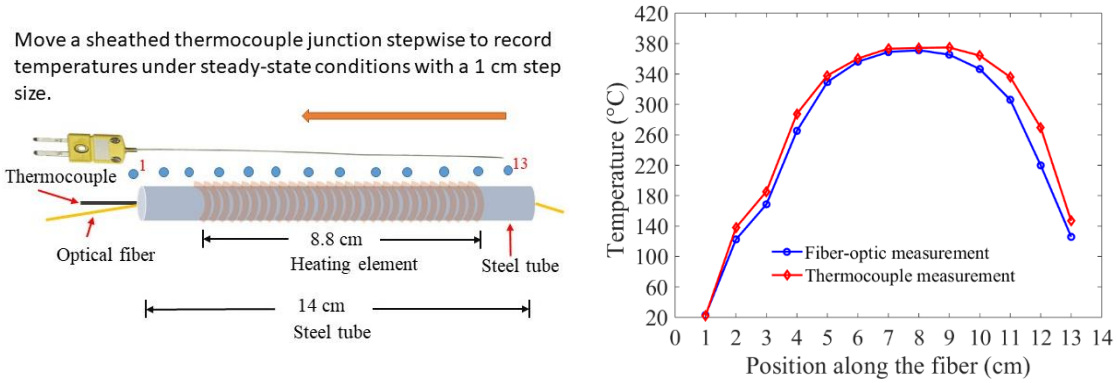

(a) (b)

Figure 5. Comparison of a spatial temperature profile derived from fiber-optic measurements with corresponding thermocouple measurements. (a) Schematic of the setup used for spatial temperature mapping of fiber-optic measurements and thermocouple measurements. The optical fiber, connected to the OFDR interrogator, was nested in a steel tube. A K-type thermocouple was re-positioned, within the steel tube and adjacent to the optical fiber, from one end of the tube to the other, to record steady-state temperature readings at 13 different positions. (b) Superposition of the spatial temperature mapping of the fiber-optic measurements and thermocouple measurements. The fiber-optic temperature measurements at 13 different positions were compared with the corresponding thermocouple measurements and showed close agreements.

Therefore, the offsets that separated the two sets of temperature measurements were due to the variable relative positions of the thermocouple, with respect to the optical fiber. However, similar spatial temperature profiles were observed with both temperature measurement systems. This experiment reiterated the fact that measuring spatially-distributed temperatures with thermocouples require moving a single thermocouple stepwise to map out a series of spatially-disposed temperature measurements or; alternatively, using multiple thermocouples with a large number of signal wires would be required. In contrast, a single continuous fixed-position optical fiber can provide distributed temperature measurements along its length.

3.3. THERMAL MAPPING OF TEST OBJECTS WITH LOCALIZED TEMPERATURE VARIATIONS

The ability to measure closely spaced temperature features is of great value for applications in the steel industry. Many steelmaking process configurations exhibit localized spatial and temporal variations in temperature. Information-rich temperature measurements would be very useful to characterize such phenomena. One such example for a steel industry application is spatial temperature measurements in a continuous caster mold. Inadequate mold lubrication, non-uniform shell growth, or crack formation in the shell can cause air gaps between a steel shell and the hotface of the mold, which leads to temperature fluctuations on the hotface of the mold [30]. Measuring these temperature fluctuations can be helpful in detecting and characterizing non-uniform shell growth events during casting. Several attempts were made to measure temperature variations on the exposed surface of the mold, caused by non-uniform shell growths using thermocouples and fiber-optic FBGs. However, the inability of thermocouple systems to measure closely

spaced temperature features and the limited spatial resolution of the quasi-distributed FBGs are a big hurdle to map closely spaced temperature variations [2,16]. The present research demonstrates that Rayleigh-backscattering-based fiber-optic temperature sensors could be a potential solution to measure temperature fluctuations in the continuous casting mold.

3.3.1. One-Dimensional (1D) Thermal Mapping. In an attempt to mimic the thermal behavior of a metal casting mold and demonstrate how well the fiber-optic system distinguishes closely spaced temperature features, hot and cold spots of known dimensions were created on a copper tube, as shown in Figure 6. An optical fiber, connected to the OFDR interrogator, was threaded through the copper tube. A ceramic tube located between two wire-wrapped copper regions was used to mimic an air gap similar to a gap caused by a non-uniform shell growth. The formation of an air gap at the metal–mold interface during casting caused reduced heat flux from the metal to the mold. Heat flux anomalies yield localized temperature features on the surface of the mold. Similarly, in the copper/ceramic tube arrangements, the ceramic tube encased regions should exhibit lower temperatures, due to reduced heat transfer from the heating coil to the fiber. To achieve localized variations in temperature along the length of a copper tube, the heat source (heater coil) needs to generate heat at a high rate. If the heat output rate of the coil is low, closely spaced temperature features can disappear due to the good thermal conductivity of the copper tube. In this experiment, an average temperature ramp-up rate of 15 °C/s was achieved and employed for conducting spatially-distributed temperature measurements. The copper tube assembly was heated using a heater coil connected to a DC power supply (Mastech HY3005D), drawing 2.6 A current at a voltage of 26 V (~65 W). The spatial temperature profile during heating was measured with the fiber-optic system.

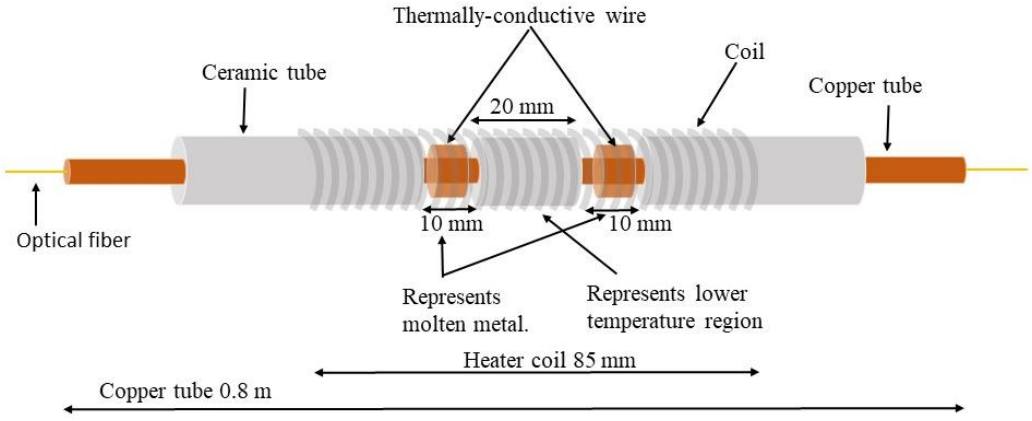

Figure 6. Copper tube assembly employed to create hot and cold spots along the long axis of an embedded optical fiber. An optical fiber was threaded through the copper tube. The ceramic tube in the middle was intended to create a low-temperature region by reducing heat flux from the heater coil to the optical fiber.

The measured spatially distributed temperature profile revealed a dip in temperature, as a result of the ceramic barrier between the heater coil and the copper tube, which contained the encased optical fiber sensor, as shown in Figure 7.

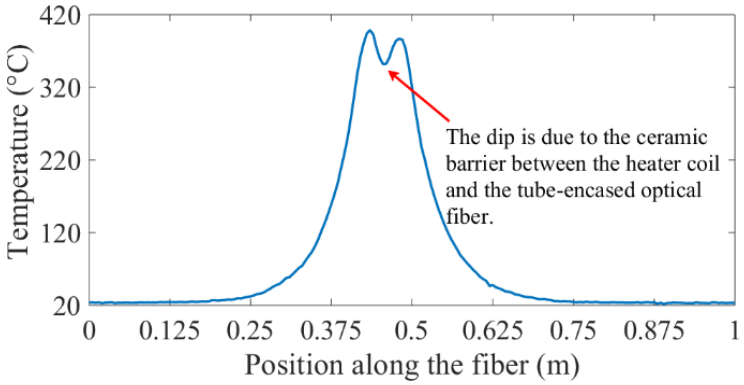

Figure 7. Spatially distributed temperature profile along the length of an optical fiber contained within a copper tube. The dip at the center of the temperature profile corresponded to a ceramic tube-encased region.

The plot in Figure 7 shows an obvious temperature feature, but quantifying the physical dimensions of the temperature feature from the plotted temperature data was not easy to carry out. The spatial derivative of the metered temperature versus position plot was calculated to address the limitations on facile interpretations of spatially distributed temperature profiles. Figure 8 shows the spatial derivative of temperature, along a sensor point position axis, which was configured with hot and cold spots, resulting in positive and negative peak features, due to sharp increases and decreases in temperature at the edges of the feature zones. The absolute value of the rectified spatial derivative yielded all positive peaks, which corresponded to the edges of the hot and cold spots. In this analysis, absolute-value rectified derivative plots were used to quantify the length of the lower temperature region, due to the easily identifiable sharp temperature changes at the ends of the lower temperature regions.

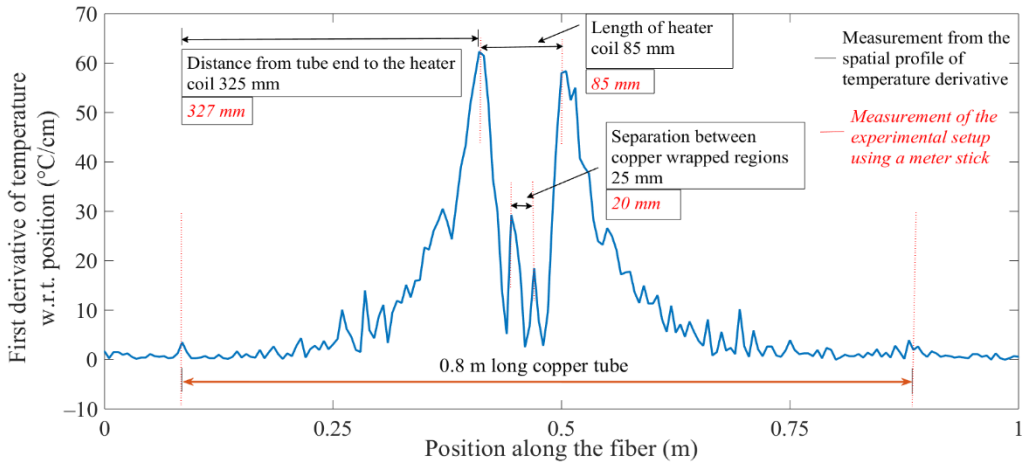

Figure 8. A plot of the absolute-value rectified spatial derivative of temperature versus position. Temperature features extracted from the plot are compared with the dimensions of the copper tube test setup with hot and cold spot features.

Furthermore, the features extracted from the spatial derivative profiles of temperature were in good agreement with the dimensions of the test setup, as shown in Figure 8. This revelation demonstrated that the fiber-optic temperature sensor could distinguish between closely spaced hot and cold spots in a heated tube structure.

3.3.2. Two-Dimensional (2D) Thermal Mapping. A series of experiments were conducted to demonstrate the 2D thermal mapping capability of the fiber-optic temperature measurement system. As discussed earlier, the capability of Rayleigh-backscattering-based fiber-optic temperature sensors to perform 2D thermal mapping could be useful for many applications in the steel industry. Real-time thermal mapping of the casting mold surface is an important process that can be used to determine the structural and mechanical properties of the solidifying shell. Information about various properties of the shell, such as surface roughness, cracks, shell buckling, and the resulting air gap formation at the metal–mold interface, could be obtained from the surface temperature of the mold [4,31]. Based on the temperature data of the mold, appropriate actions can be taken to improve the quality of the casting. There are many phenomena in steel casting that cause irregularities in shell growth. Peritectic behavior is one such phenomenon that leads to surface defects and breakouts in continuous casting. Peritectic behavior occurs during solidification of certain alloy systems, in which a secondary phase grows on the periphery of a primary phase. During the solidification of steel, for example, the primary phase–ferrite (δ) precipitates first from the molten metal. This pre-existing ferrite phase then reacts with the residual liquid metal to form the secondary solid phase–austenite (γ). The two solid phases formed during solidification have different thermal contractions, due to their different packing densities, which makes peritectic steel grades susceptible to shrinkage during

solidification. The shrinkage caused by the δ/γ phase transformation during the initial solidification of peritectic steel grades can induce shell buckling, which in turn causes uneven shell formation, non-uniform shell and mold temperatures, and an average decrease in heat flux from shell to the mold [30]. Measuring closely spaced temperature features on the mold surface can be useful in the characterization of peritectic behavior.

In order to experimentally simulate the peritectic behavior in a lab environment, temperature mapping experiments were conducted using a peritectic plate model and a copper block equipped with optical fibers, as shown in Figure 9. The peritectic plate model (50 mm × 50 mm × 6 mm thick) with localized temperature variations was machined to mimic the behavior of a shell with non-uniform features. The copper plate of uniform thickness was modified by milling out a cubical bubble to simulate an air gap caused by non-uniform shell growth, as shown in Figure 9a.

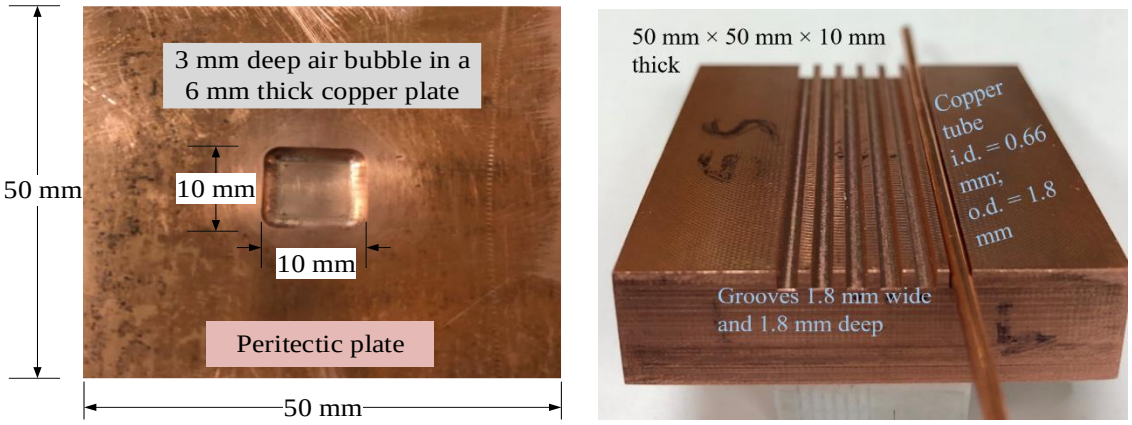

(a) (b)

Figure 9. The arrangement of a peritectic plate model and a copper block with embedded optical fibers. (a) A peritectic plate model with an air bubble. The peritectic plate exhibits a lower temperature in the middle due to the presence of an air bubble. (b) A copper block equipped with fiber-optic temperature sensors. The grooves are machined on the surface of the block. The copper tube-encased optical fibers were press-fitted in the grooves.

Another copper block was equipped with optical fibers (OF). Optical fibers were placed in copper tubes (i.d. = 0.66 mm; o.d. = 1.8 mm), which in turn were fitted in grooves (1.8 mm wide and 1.8 mm deep) machined on the surface of the copper block, as shown in Figure 9b. The OF-equipped block had copper-tube-encased optical fibers in two grooves. In one of the experiments, the pre-heated peritectic plate with localized temperature variations was mated with the copper block equipped with optical fibers. When the block mated with the pre-heated peritectic plate, one of the sensor-equipped grooves was placed on the continuous flat metal surface of the peritectic plate, while the other groove had a section laid over the air bubble. The temperature distribution over the OF-equipped copper block, as a result of heat transfer from the peritectic plate to the OF equipped block, was measured. The section of the optical fiber laid over the air bubble was expected to show a dip in the spatial temperature profile. As shown in Figure 10, the temperature features were not prominent enough to reveal the physical dimensions of the test setup.

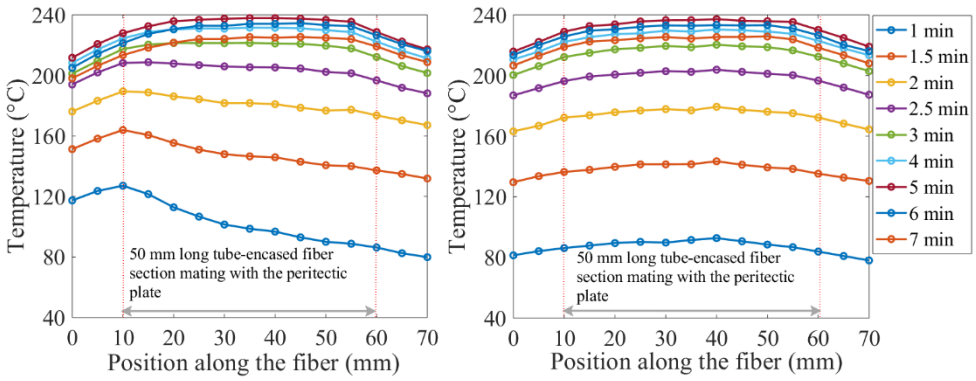

Figure 10. Temperature profiles from two sections of the optical fiber metered by mating the OF-equipped block with a peritectic plate model. Temperature features were subdued because the optical fiber was free-floating inside the copper tube. The copper tube was in contact with the hotface of the copper block.

The free-floating fiber inside the copper tube was suspected to be the cause of ambiguities in temperature measurements, due to the poor thermal contact between the optical fiber and the copper tube that was in contact with the hotface of copper block. To test the hypothesis that temperature features were subdued due to poor thermal contact between the free-floating optical fibers and the hotface of the copper block, another 1D thermal simulation experiment was performed using the same peritectic plate model into which a cubical bubble was machined, as shown in Figure 11. A bare optical fiber was taped onto the peritectic plate bridging the air bubble, as shown in Figure 11a. The peritectic plate was then heated on a hot plate. Temperature measurements were conducted with a 1.3 mm spatial resolution.

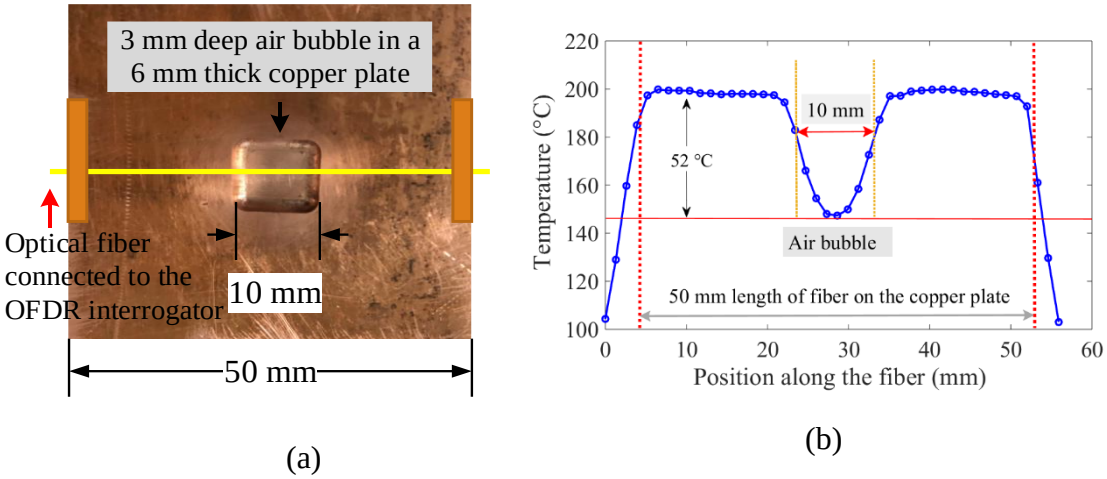

Figure 11. 1D thermal modeling experiment using the peritectic plate model. (a) A section of an optical fiber taped on the surface of the peritectic plate. The dimensions of the air bubble were 10 mm × 10 mm × 3 mm deep. A 10 mm-long bubble in the center of the 50-mm long plate creates a low-temperature region. (b) Distributed temperature profile with a temperature dip in the middle. The 10 mm section of the optical fiber in the middle of the cavity does not make physical contact with the peritectic plate and registers lower temperatures.

The temperature profile measured in this experiment, as shown in Figure 11b, exhibited a low-temperature feature that corresponded well to the length dimension of the rectangular air bubble on the model sheet. This experiment demonstrated that the high thermal conductivity of a copper tube used in the earlier experiment most likely eradicated temperature gradients, making it difficult for the optical fiber to distinguish closely spaced temperature features. On the other hand, the bare fiber worked very well because the optical fibers were fabricated from glass, a thermally insulating material.

Another test was carried out to mimic the 2D thermal behavior of the mold surface with non-uniform shell growth. A 2D array, constructed using a single fiber-optic sensor, was attached to the peritectic plate model. The bottom side of the optical fiber-equipped peritectic plate arrangement was heated on a hot plate, and spatial temperature profiles along the fiber sections were recorded with the OFDR system, as shown in Figure 12. A continuous optical fiber was used to arrange eight parallel paths, each separated by 2 mm, on the peritectic plate model, as shown in Figure 12a. The peritectic plate was heated on a hot plate, and spatially distributed temperature data sets were recorded at constant time intervals. The temperature distribution along the sections of the optical fiber positioned on the flat surface registered a uniform temperature, while the sections of the optical fiber positioned along the top of the air bubble exhibited dips in the temperature profiles, as depicted in Figure 12b. Figure 13 illustrates a cropped view of the peritectic plate overlaid with fiber-optic temperature sensors and a thermal map of the plate recorded with the OFDR system. The thermal map of the peritectic plate matched well with the dimensions of the plate. The air bubble on the peritectic plate shown in Figure 13a appeared as a low-temperature feature on the thermal map of the plate. The dimensions of the low-

temperature region shown in Figure 13b corresponded to the physical dimensions of the air bubble on the peritectic plate.

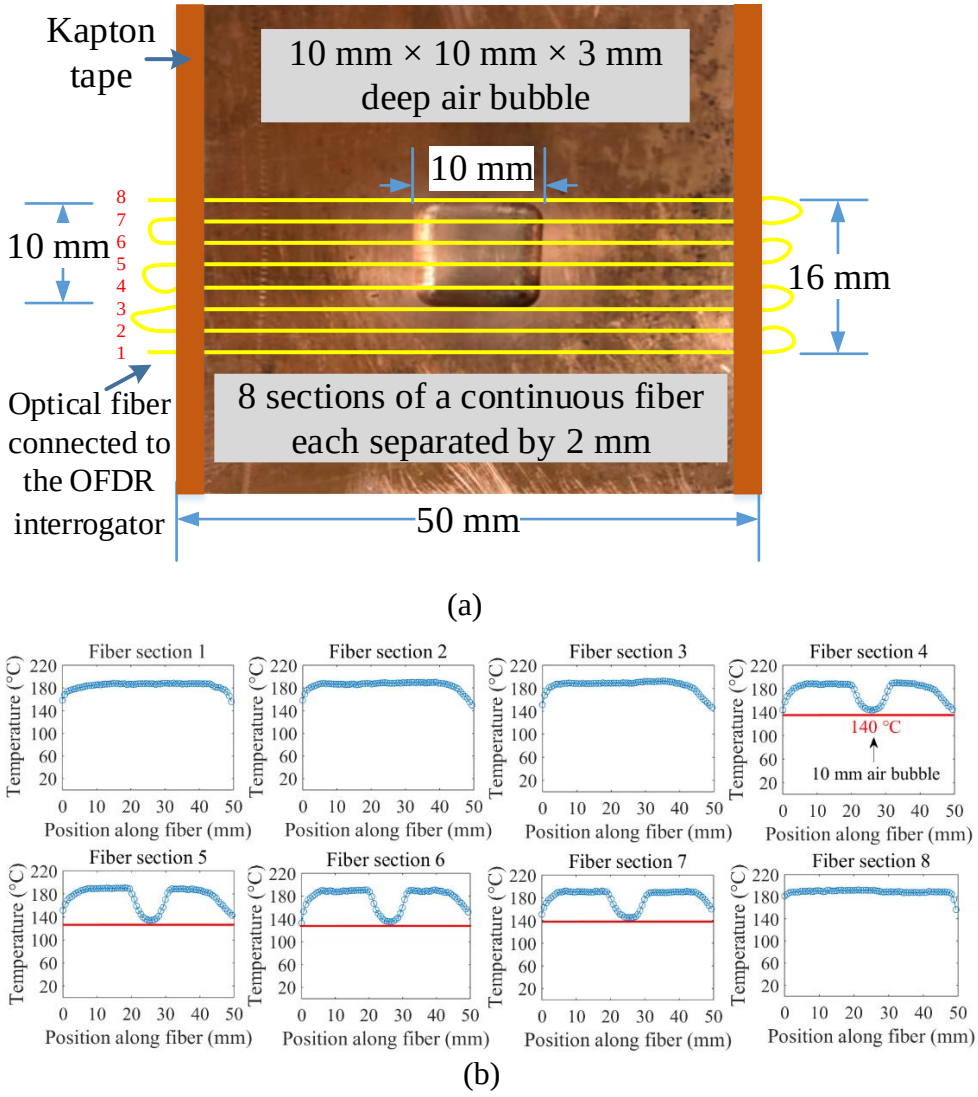

Figure 12. An arrangement of eight sections of an optical fiber on the peritectic plate and spatial temperature profiles along the sections of the fiber. (a) Arrangement of eight sections of a looped continuous optical fiber on the surface of the peritectic plate model. Four sections (1–3, 8) of the optical fiber were laid on the flat surface, while the other four sections (4–7) were laid over the air bubble. (b) Temperature distributions along eight 50 mm-sections of the optical fiber. The sections of the optical fiber laid over the air bubble exhibited a dip in the spatial temperature profile.

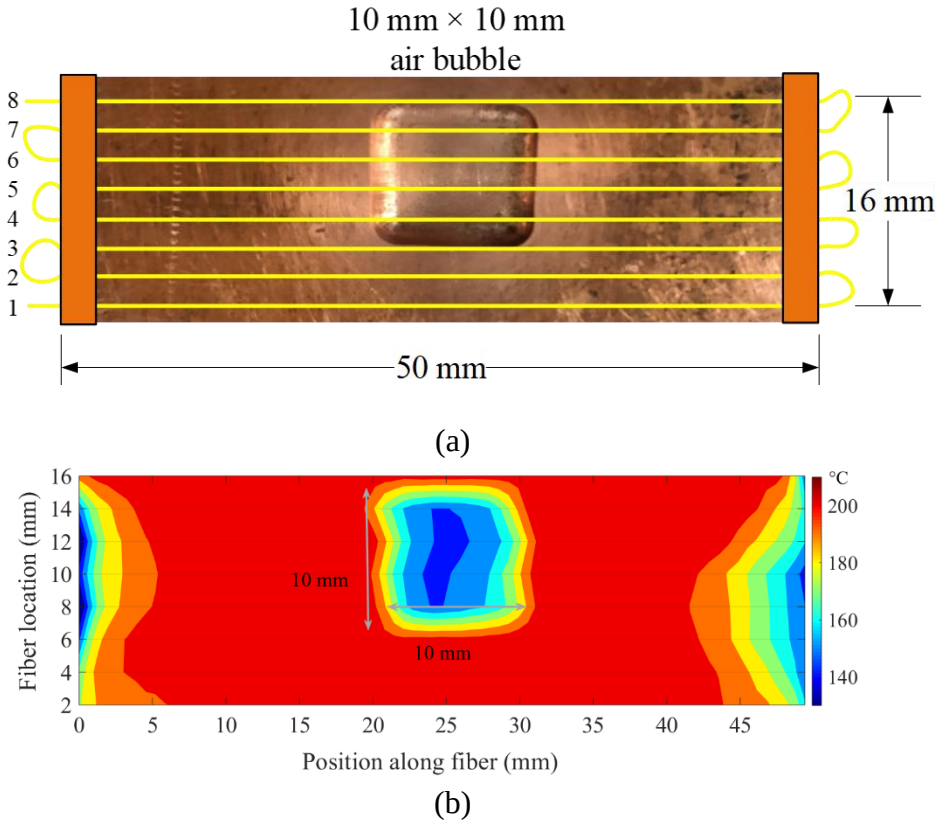

Figure 13. A cropped view of the peritectic plate overlaid with fiber-optic temperature sensors and a thermal map of the plate. (a) Arrangement of optical fibers on the peritectic plate with an air bubble in the center (10 mm × 10 mm). (b) Thermal map of the peritectic plate. The low-temperature feature is due to the air bubble.

As discussed earlier, absolute-value rectified spatial derivatives of temperature are useful to quantify the dimensions of hot and cold spots. Similarly, a contour plot of absolute-value rectified spatial derivative of temperature with respect to the position along the optical fiber could also be used to quantify the dimensions of the temperature features. In the aforementioned test, absolute-value rectified spatial derivatives of temperature, with respect to fiber position, resulted in peaks at the edges of the air bubble, due to sharp changes in temperature at those positions. The contour of absolute-value rectified spatial derivatives should give lines, one at each edge. The distance between these lines should be

the length of the low-temperature region. The contour of the absolute-value rectified spatial derivative of temperature is given in Figure 14. The peak features in the contour plot appeared as two lines, which were in register with the edges of the low-temperature region. The width of each line was caused by the width of the derivative peak.

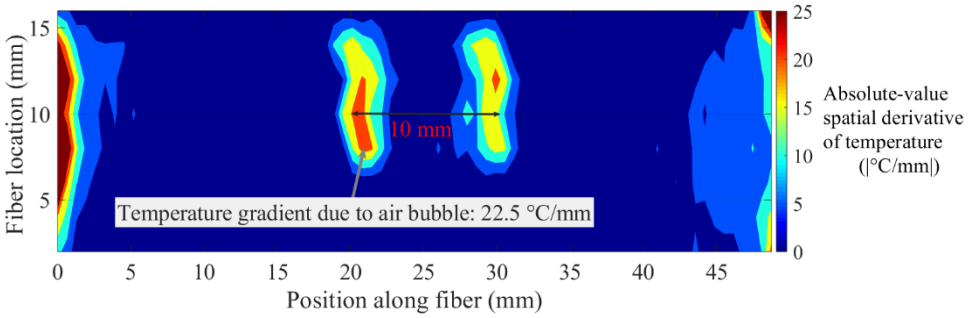

Figure 14. Contour plot of the absolute-value rectified spatial derivative of 2D temperatures. The two contour lines in the middle of the plot were caused by peaks in the absolute-value derivative plot. The separation between the two line features was the actual length of the low-temperature region.

To demonstrate the sensitivity of the Rayleigh-backscattering-based temperature measurement, another peritectic plate model was machined by milling a bubble smaller than the one presented in the previous experiment (see Figure 11). A cylindrical air bubble, 3 mm in depth, 5 mm in width, and 10 mm in length, was milled out from the surface of a copper plate. Figure 15 illustrates a top view of the peritectic plate, overlaid with fiber-optic temperature sensors and a thermal map of the plate, recorded with the OFDR interrogator. A 2D sensor array, composed of seven sections of a continuous optical fiber, was laid on the peritectic plate model, as shown in Figure 15a. The bottom side of the optical fiber-equipped peritectic plate arrangement was heated on a hot plate, and a 2D

thermal map of the plate was recorded. The low-temperature feature, shown in Figure 15b, matched well with the actual dimensions of the air bubble on the peritectic plate.

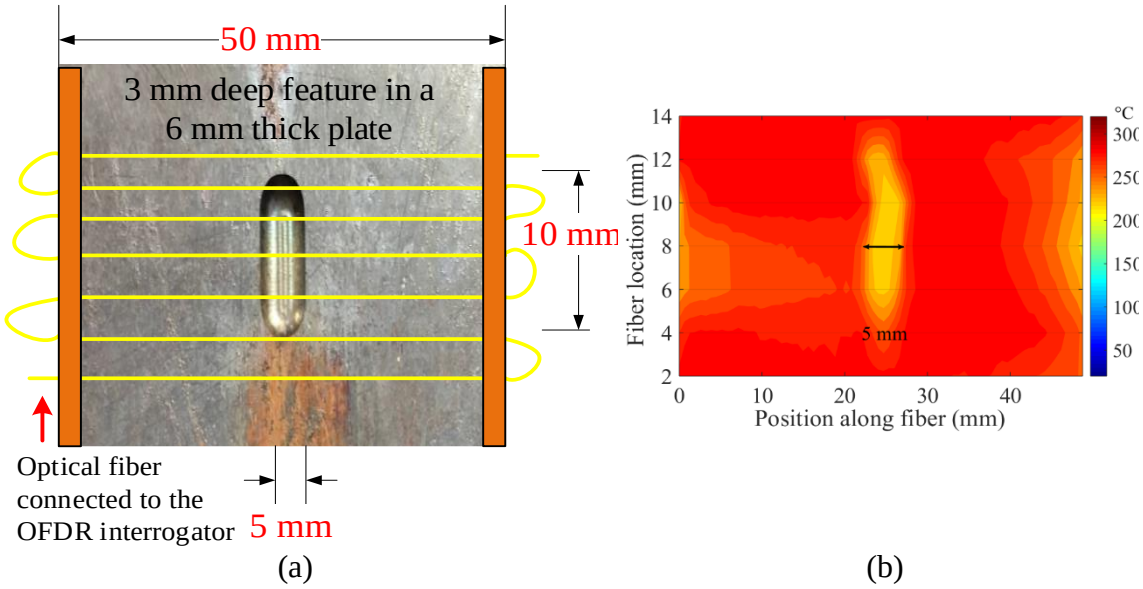

Figure 15. A top view of the peritectic plate overlaid with fiber-optic temperature sensors and a thermal map of the plate recorded with the OFDR interrogator. (a) Arrangement of a continuous optical fiber on a peritectic plate with a 5 mm-wide cylindrical air bubble. Seven sections of a continuous optical fiber were laid on the plate side-by-side, with 2-mm spacing between the adjacent sections of the optical fiber. (b) The thermal map of the peritectic plate model showed a low-temperature feature, due to an air cavity on the plate. The temperature feature matched well with the actual dimensions of the air cavity.

The experimental simulation of the peritectic-like phenomenon provided strong evidence that the Rayleigh-scattering-based fiber-optic temperature sensors could measure temperature features in a mold associated with peritectic behavior. The spatially continuous thermal maps of the mold during solidification could help monitor rapid and closely spaced thermal events at the meniscus and over the entire mold surface, which were attributed to the peritectic reaction.

3.4. DISTRIBUTED TEMPERATURE MEASUREMENTS ACROSS A MOLD CAVITY DURING ALUMINUM CASTING

The temperature measurement capabilities of the Rayleigh-scattering-based fiber-optic sensor were demonstrated in an aluminum casting experiment. Figure 16 illustrates a schematic and photographs of a test setup that employed the Rayleigh-scattering-based fiber-optic sensor to investigate the spatial and temporal temperature features in the process of aluminum casting. Temperature measurements were performed in a sand mold, during mold filling and solidification, using the apparatus illustrated in Figure 16a. An optical fiber temperature sensor was encased in a stainless steel tube (i.d. = 0.5 mm, o.d. = 0.8 mm). The rigid stainless steel tube protected the optical fiber and prevented it from kinking during the mold filling process. The tube-encased fiber was placed laterally in a 60-mm wide mold cavity, across the melt-flow direction, as illustrated in Figure 16b. An aluminum alloy (Al 90.062%, Si 7.350%, Cu 1.346%, Fe 0.457%, Mg 0.341%, Zn 0.289%, Mn 0.056%, and Ti 0.010%) was induction melted, heated to 730 °C, and hand ladled, to bottom-fill the instrumented sand mold, as shown in Figure 16c.

Figure 17 illustrates temperature measurements across the mold cavity during mold filling and solidification. The spatially distributed temperature profiles along the width of the mold cavity and through the mold wall, at different times, are shown in Figure 17a. The metered temperatures along the tube-encased optical fiber jumped to approximately 710 °C, when the tube came in direct contact with the molten aluminum. The spatial temperature profile then dropped to about 500 °C where it exhibited a thermal arrest. The cool-down process was monitored down to 450 °C.

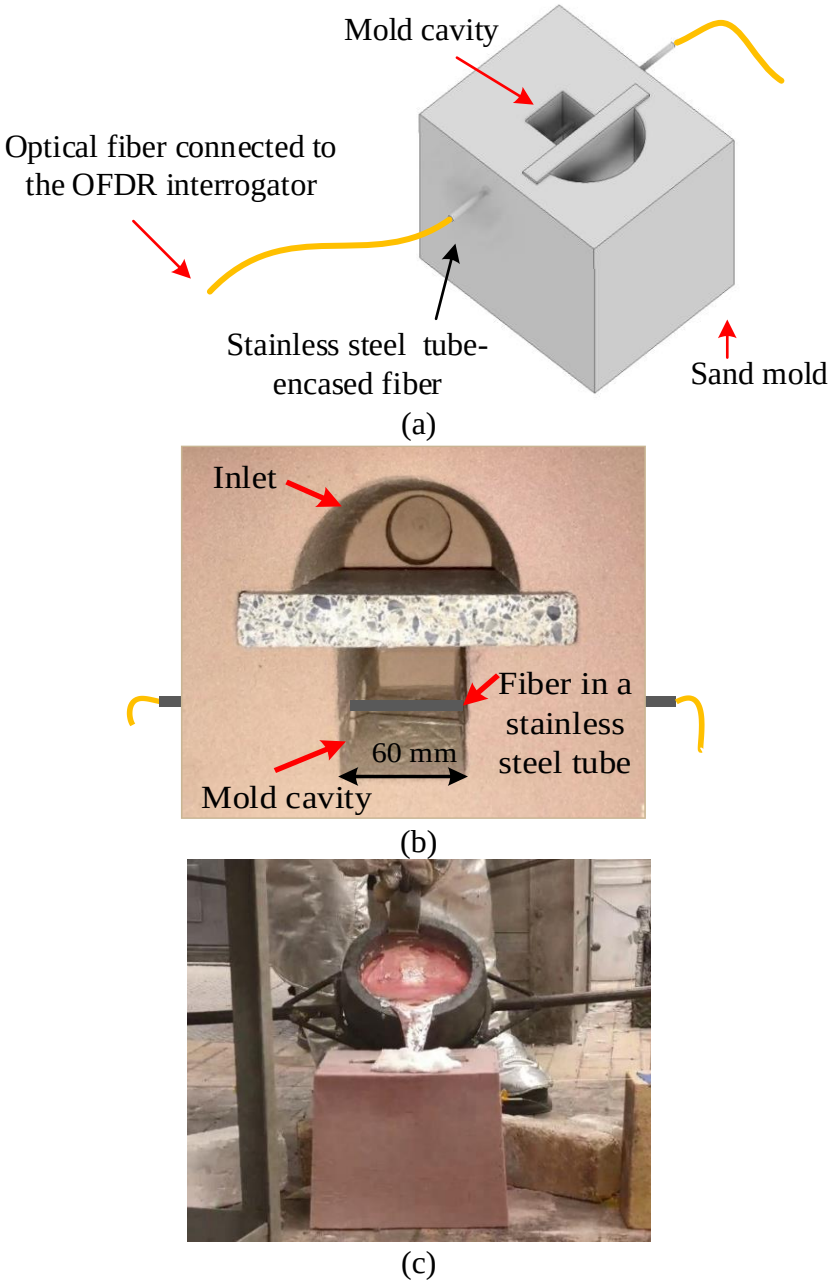

Figure 16. A schematic and photographs of a test setup that employed the Rayleigh-scattering-based fiber-optic sensor to investigate spatial and temporal temperature features in the process of an aluminum casting. (a) A schematic diagram of the experimental setup used for monitoring temperature across the mold cavity at a location approximately in the middle of the mold, during the process of pouring aluminum and subsequent solidification. (b) A top-view photograph of the sand mold used in the experiment, illustrating the location of the transverse fiber-optic temperature sensor. Molten metal was poured into the sand mold through an inlet, and the mold cavity was filled from the bottom using a baffle. (c) A photograph of the molten aluminum being poured into the mold.

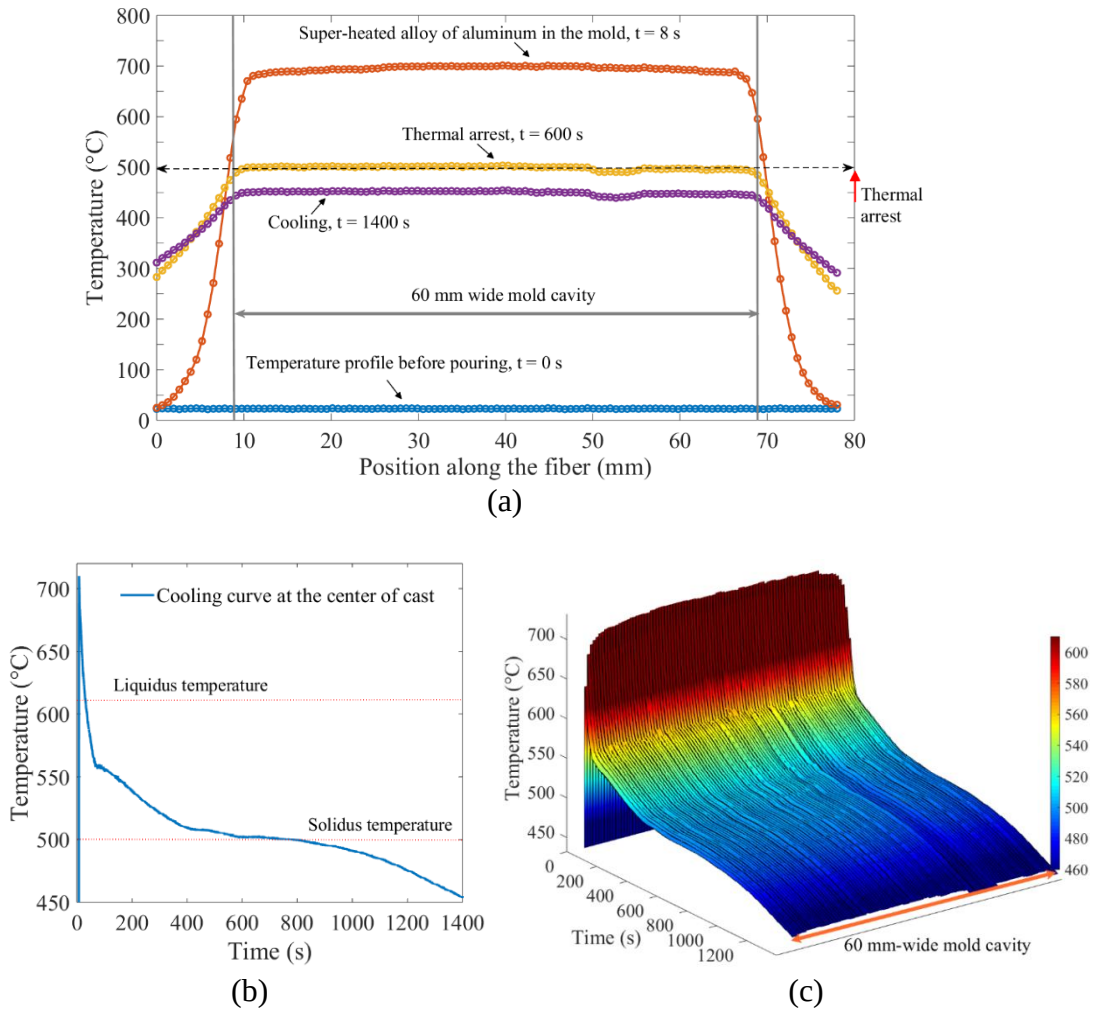

Figure 17. Temperature measurements across the mold cavity recorded with the OFDR interrogator, during the process of pouring aluminum and the subsequent solidification. (a) Spatially-distributed temperature profile across the mold cavity. The time t = 0 s marked the moment just before the molten metal was poured into the mold cavity. At time t = 8 s, the mold was completely filled with the molten aluminum. At time t = 600 s, the thermal arrest temperature profile was observed at 500 °C. The time t = 1400 s corresponded to the last recorded measurement during the cooling process. (b) The cooling curve recorded at the center of the cast. Different temperatures, such as liquidus and solidus, could be observed from the cooling curve. (c) Spatial-temporal thermal map showing cooling curves at 92 equally spaced positions, across the 60 mm-wide mold cavity.

Figure 17b shows a cooling curve obtained at a location approximately at the center of the cast. The solidification started at the liquidus temperature (~610 °C) with the

formation of primary (α-Al) dendrites, followed by eutectic reactions. The solidification ended at the solidus temperature (~500 °C). The multiple stages of solidification between liquidus (~610 °C) and solidus (~500 °C) could be distinguished by different gradients, during the phase transformations. After the completion of solidification, cooling resumed at a steady rate. The steady cooling rate after the solidification process indicated the uniform cooling of the solid.

As demonstrated earlier, Rayleigh-scattering-based fiber-optic sensors offer spatially continuous temperature measurements. The capability of fiber-optic sensors to perform distributed measurements cannot be easily replicated by conventional thermocouples. The obvious advantages of fiber-optic measurement are illustrated in Figure 17c, where the cooling curves across the entire mold cavity dimension are shown. Given the 0.65 mm spatial resolution of the fiber-optic measurement system, a single section of optical fiber 60 mm in length provided temperature profile measurements equivalent to temperature measurements from 92 thermocouples along the 60 mm-wide mold cavity. Such information-rich measurements can be helpful in investigating the internal temperature state of melts, during the solidification process. The heating and cooling curves at different locations within the mold could be obtained. The interfacial thermal resistance at the metal–mold interface could also be quantified using spatially distributed temperature profiles.

4. CONCLUSIONS

A Rayleigh-backscattering-based fiber-optic temperature sensing system employing an optical frequency domain reflectometry (OFDR) interrogator was developed. The distributed sensing capability of the system was tested in a foundry laboratory. The robust sensor head, composed of an unmodified single-mode fiber, survived temperatures up to 710 °C. The fiber-optic sensor produced accurate temperature measurements comparable to a standard thermocouple. Moreover, the spatially distributed sensing capability of an optical fiber enabled mapping of localized variations in temperatures. Spatially distributed fiber-optic temperature measurements provided a clear advantage over conventional thermocouples, due to the minimally invasive and information-rich distributed sensing capabilities of optical waveguides. Experiments were designed to provide evidence that the fiber-optic sensor was a viable candidate for temperature measurements in steel industry applications. Spatially-localized temperature variations were created on copper tube and plate test objects. Spatially localized temperature variations were successfully measured with the fiber-optic distributed temperature sensor with a 0.65-mm resolution. Temperature features were used to specify the dimensions of hot and cold spots. High spatial resolution and fast measurement rates (~250 measurements per second) by the fiber-optic system were useful in determining thermal maps of the copper test objects. Moreover, experiments revealed that optical fibers require continuous thermal contact with the copper test object, for reliable temperature measurements. In addition to experimental simulations using copper test objects, a metal casting experiment was conducted to test the measurement capability and survivability of optical fibers in

harsh environments. The temperature profile across the cavity of a sand mold was successfully monitored, during an aluminum pour and solidification process. The aluminum solidification experiment provided a glimpse into how useful distributed fiber-optic temperature measurements could be for metal casting. Given the aforementioned advantages of distributed sensing with a high spatial resolution and a fast measurement rate, Rayleigh-backscattering-based fiber-optic sensors offer practical advantages for temperature measurement profiles in steel industry applications.

ACKNOWLEDGMENTS

This research was funded by the Kent D. Peaslee Steel Manufacturing Research Center (PSMRC) at Missouri S&T.

REFERENCES

1. Suzuki, M.; Cho, J.W.; Sato, H.; Shibata, H.; Emi, T. Analysis of Heat Transfer and Solidifying Shell Deformation in Mold in High Speed Continuous Casting of Peritectic Medium Carbon Steels. In Proceedings of the Steelmaking Conference, Toronto, Canada, 22–24 March 1998.

2. Xia, G.; Narzt, H.P.; Fürst, C.; Mörwald, K.; Moertl, J.; Reisinger, P.; Lindenberger, L. Investigation of mould thermal behaviour by means of mould instrumentation. *Ironmak. Steelmak.* 2004, *31*, 364–370.

3. Thomas, B.G.; Wells, M.; Li, D. Monitoring of Meniscus Thermal Phenomena with Thermocouples in Continuous Casting of Steel. In *Sensors, Sampling, and Simulation for Process Control*; John Wiley & Sons, Inc.: Hoboken, NJ, USA, 2011.

4. Natarajan, T.T.; Story, S.R.; Piccone, T.J.; van Ness, K.D. Peritectic Range Study Using Mold Thermocouple Data. In Proceedings of the 2017 AISTech Conference, 2017; Nashville, TN, USA, 8–11 May 2017.

5. Lee, B. Review of the present status of optical fiber sensors. *Opt. Fiber Technol.* 2003, *9*, 57–79.

6. Zhu, C.; Zhuang, Y.; Zhang, B.; Muhammad, R.; Wang, P.P.; Huang, J. A Miniaturized Optical Fiber Tip High-Temperature Sensor Based on Concave-Shaped Fabry-Perot Cavity. *IEEE Photonics Technol. Lett.* 2019, *31*, 35–38.

7. Lecoeuche, V.; Hathaway, M.; Webb, D.; Pannell, C.; Jackson, D. 20-km distributed temperature sensor based on spontaneous Brillouin scattering. *IEEE Photonics Technol. Lett.* 2000, *12*, 1367–1369.

8. Bao, X.; Dhliwayo, J.; Heron, N.; Webb, D.; Jackson, D.A. Experimental and theoretical studies on a distributed temperature sensor based on Brillouin scattering. *J. Lightwave Technol.* 1995, *13*, 1340–1348.

9. Shimizu, K.; Horiguchi, T.; Koyamada, Y. Measurement of distributed strain and temperature in a branched optical fiber network by use of Brillouin optical time-domain reflectometry. *Opt. Lett.* 1995, *20*, 507–509.

10. Weng, Y.; Ip, E.; Pan, Z.; Wang, T. Single-end simultaneous temperature and strain sensing techniques based on Brillouin optical time domain reflectometry in few-mode fibers. *Opt. Express* 2015, *23*, 9024–9039.

11. Guan, B.-O.; Tam, H.Y.; Tao, X.-M.; Dong, X.-Y. Simultaneous strain and temperature measurement using a superstructure fiber Bragg grating. *IEEE Photonics Technol. Lett.* 2000, *12*, 675–677.

12. Patrick, H.; Williams, G.; Kersey, A.; Pedrazzani, J.; Vengsarkar, A. Hybrid fiber Bragg grating/long period fiber grating sensor for strain/temperature discrimination. *IEEE Photonics Technol. Lett.* 1996, *8*, 1223–1225.

13. Jung, J.; Nam, H.; Lee, B. Fiber Bragg grating temperature sensor with controllable high sensitivity. In Proceedings of the 11th Annual Meeting—IEEE Lasers and Electro-Optics Society 1998 Annual Meeting, Orlando, FL, USA, 1–4 December 1998.

14. Zhang, B.; Kahrizi, M. High-Temperature Resistance Fiber Bragg Grating Temperature Sensor Fabrication. *IEEE Sens. J.* 2007, *7*, 586–591.

15. Thomas, B.G.; Okelman, M. Implementation of Temperature and Strain Micro-Sensors into a Casting Mold Surface. In *Sensors, Sampling, and Simulation for Process Control*; John Wiley & Sons, Inc.: Hoboken, New Jersey, USA, 2011.

16. Lieftucht, D.; Reifferscheid, M.; Schramm, T.; Krasilnikov, A.; Kirsch, D. HD Mold—A New Fiber-Optical-Based Mold Monitoring System. *Iron Steel Technol.* 2013, *10*, 87–95.

17. Spierings, T.; Kamperman, A.; Hengeveld, H.; Kromhout, J.; Dekker, E. Development and Application of Fiber Bragg Gratings for Slab Casting. In Proceedings of the 2017 AISTech Conference, Nashville, TN, USA, 8–11 May 2017.

18. Du, Y.; Jothibasu, S.; Zhuang, Y.; Zhu, C.; Huang, J. Rayleigh backscattering based macrobending single mode fiber for distributed refractive index sensing. *Sens. Actuators B Chem.* 2017, *248*, 346–350.

19. Du, Y.; Yang, Q.; Huang, J. Soft Prosthetic Forefinger Tactile Sensing via a String of Intact Single Mode Optical Fiber. *IEEE Sens. J.* 2017, *17*, 7455–7459, doi:10.1109/JSEN.2017.2759907.

20. Jothibasu, S.; Du, Y.; Anandan, S.; Dhaliwal, G.S.; Gerald, R.E.; Watkins, S.E.; Chandrashekhara, K.; Huang, J. Spatially continuous strain monitoring using distributed fiber optic sensors embedded in carbon fiber composites. *Opt. Eng.* 2019, *58*, 072004.

21. Du, Y.; Jothibasu, S.; Zhuang, Y.; Zhu, C.; Huang, J. Unclonable Optical Fiber Identification Based on Rayleigh Backscattering Signatures. *J. Lightwave Technol.* 2017, *35*, 4634–4640.

22. Zhu, C.; Zhuang, Y.; Chen, Y. Distributed fiber-optic pressure sensor based on Bourdon tubes metered by optical frequency-domain reflectometry. *Opt. Eng.* 2019, *58*, 072010.

23. Du, Y.; Liu, T.; Ding, Z.; Han, Q.; Liu, K.; Jiang, J.; Chen, Q.; Feng, B. Cryogenic Temperature Measurement Using Rayleigh Backscattering Spectra Shift by OFDR. *IEEE Photonics Technol. Lett.* 2014, *26*, 1150–1153.

24. Yan, A.; Huang, S.; Li, S.; Chen, R.; Ohodnicki, P.; Buric, M.; Lee, S.; Li, M.-J.; Chen, K.P. Distributed Optical Fiber Sensors with Ultrafast Laser Enhanced Rayleigh Backscattering Profiles for Real-Time Monitoring of Solid Oxide Fuel Cell Operations. *Sci. Rep.* 2017, *7*, 1–9.

25. Boyd, C.D.; Dickerson, B.D.; Fitzpatrick, B.K. Monitoring distributed temperatures along superconducting degaussing cables via Rayleigh backscattering in optical fibers. In Proceedings of the Intelligent Ships Symposium IX, PA, USA, 25–26 May 2011.

26. Kwon, Y.-S.; Naeem, K.; Jeon, M.-Y.; Kwon, I.-B. Enhanced sensitivity of distributed-temperature sensor with Al-coated fiber based on OFDR. *Opt. Fiber Technol.* 2019, *48*, 229–234.

27. Wood, T.W.; Blake, B.; Blue, T.E.; Petrie, C.M.; Hawn, D. Evaluation of the Performance of Distributed Temperature Measurements With Single-Mode Fiber Using Rayleigh Backscatter up to 1000 °C. *IEEE Sens. J.* 2013, *14*, 124–128.

28. McCary, K.; Wilson, B.; Birri, A.; Blue, T.E. Response of Distributed Fiber Optic Temperature Sensors to High-Temperature Step Transients. *IEEE Sens. J.* 2018, *18*, 8755–8761.

29. Sang, A.K.; Froggatt, M.E.; Gifford, D.K.; Dickerson, B.D. One centimeter spatial resolution temperature measurements from 25 to 850 C using Rayleigh scatter in gold coated fiber. In Proceedings of the Conference on Lasers and Electro-Optics/Quantum Electronics and Laser Science Conference and Photonic Applications Systems Technologies, Baltimore, MD, USA, 6–11 May 2007.

30. Suzuki, M.; Yu, C.H.; Sato, H.; Tsui, Y.; Shibata, H.; Emi, T. Origin of Heat Transfer Anomaly and Solidifying Shell Deformation of Peritectic Steels in Continuous Casting. *ISIJ Int.* 1996, *36*, S171–S174.

31. Abraham, S.; Bodnar, R.; Lonnqvist, J.; Shahbazian, F.; Lagerstedt, A.; Andersson, M. Investigation of Peritectic Behavior of Steel Using a Thermal Analysis Technique. *Met. Mater. Trans. A* 2019, *50*, 2259–2271.

II. DISTRIBUTED FIBER-OPTIC SENSING WITH LOW BENDING LOSS BASED ON THIN-CORE FIBER

Muhammad Roman [1], Chen Zhu [1, *], Ronald J. O'Malley [2], Rex E. Gerald II [1], and Jie Huang [1, *]

[1]Department of Electrical and Computer Engineering, Missouri University of Science and Technology, Rolla, MO 65409, USA.

[2]Department of Material Science and Engineering, Missouri University of Science and Technology, Rolla, MO 65409, USA.

*Correspondence: cznwq@mst.edu, jieh@mst.edu

ABSTRACT

This paper presents a thin-core high-numerical aperture (TC-HNA) optical fiber with low macrobending loss for Rayleigh backscattering-based (RBS-based) temperature and strain measurements. The standard single-mode optical fiber (SMF), commonly used in RBS-based sensing, has low macrobending loss-resistance, making the fiber less suited for sensing applications that require sharp bending of the fiber under test. The TC-HNA fiber, on the other hand, offers high macrobending loss-resistance. Experiments were designed and conducted to demonstrate the reliability of a TC-HNA fiber for RBS-based temperature and strain measurements. The macrobending losses in a standard SMF and a TC-HNA fiber were compared in many experiments conducted with different bending radii ranging from 12.5 mm down to 0.9 mm. The RBS signal for a standard SMF, with a single turn of a 5 mm bending radius, degraded severely, exhibiting a 75% drop (6 dB) in signal power. Notably, the RBS signal for a similar test configuration of a TC-HNA fiber did not exhibit any observable loss. We demonstrated that a TC-HNA fiber could be used for RBS-

based measurements with a single turn of ~1 mm bending radius. Moreover, an experiment was conducted to demonstrate the spatial thermal mapping capability of the TC-HNA fiber configured with multiple tight bends with radii in the range ~2–3 mm. The high macrobending loss-resistance of the TC-HNA fiber could extend the range of applications for RBS-based measurements to compact structures, such as batteries, robotic fingers, and printed circuit boards, where sharp bending of the test optical fiber is unavoidable.

Keywords: Fiber-optic sensor, macrobending loss, numerical aperture, optical frequency domain reflectometry, Rayleigh scattering, thin-core fiber, tight bends.

1. INTRODUCTION

Fiber-optic sensors have seen tremendous growth due to several significant advantages over conventional sensors, such as miniaturization, immunity to electromagnetic interferences, and the capability to perform spatially distributed measurements. Several fiber-optic sensors were reported that provide quasi-distributed or distributed measurements for various parameters, including temperature [1], strain [2], pressure [3], and humidity [4], to name a few. Among the sensors that provide quasi-distributed measurements, the most widely used sensor is fiber Bragg grating (FBG). Other than measuring temperature and strain [5], FBGs were successfully demonstrated for humidity sensing [4], chemical detection [6], and measurement of displacement and torque [7]. However, the introduction of measurement dead zones, due to the quasi-distributed sensing capability of FBGs, could be a limitation in applications that require spatially continuous measurements. Moreover, special methods are required to create Bragg gratings

in optical fibers, such as creating index modification in the core employing a femtosecond laser or exposing the core to UV light. These fabrication methods increase the cost per sensor. Another limitation of FBGs is that a limited number of FBGs can be interrogated along a single continuous optical fiber. Therefore, to achieve the desired number of measurement points, multiple optical fibers connected to multiple light sources and detectors may be required to perform the desired measurements.

In contrast to quasi-distributed sensors that require special methods to create sensors in optical fibers, truly distributed sensors exploit light scattering in unaltered optical fibers. Distributed fiber-optic sensing (DFOS) is mainly based on three phenomena—Raman, Brillouin, and Rayleigh scattering. The two commonly used techniques to interrogate light scattering in optical fibers are optical time-domain reflectometry (OTDR) [8] and optical frequency-domain reflectometry (OFDR) [9], [10]. Various sensors based on Raman scattering, employing the interrogation technique of OTDR, were reported, primarily for temperature measurements [11], [12]. The sensors based on Raman OTDR offer an extended sensing range (several kilometers) with a spatial resolution of ~1 m. DFOS based on Brillouin scattering has attracted considerable interest for temperature and strain measurements in large structures, such as dams, oil and gas pipelines, and bridges [13]. The sensors based on Brillouin OTDR offer an extended sensing range (>50 km) and reasonable spatial resolution for large structures (~ 1 m). The low spatial resolution of the sensors based on Brillouin OTDR was improved to a few centimeters by another interrogation technique called optical time-domain analysis (OTDA) [14]. A frequency-domain analysis technique was reported to reduce the cost of the systems based on Brillouin scattering for distributed temperature and strain

measurements [15]. The proposed technique offers a sensing range of 5 km with a spatial resolution of 5 m. Moreover, a different approach based on coherent OTDR was proposed to interrogate Rayleigh backscattering in single-mode fibers for distributed temperature and strain measurements [16]. The proposed approach offered a spatial resolution of ~1 m and a temperature resolution of 0.01 °C. Another low-cost alternative to the techniques of OTDR and OFDR was reported, which was based on Transmission-Reflection Analysis (TRA) [17]. The typical spatial resolution of the systems based on TRA was ~1 m. However, efforts were made to improve the spatial resolution of the TRA system to 0.15 m by replacing standard single-mode fibers with magnesium and erbium co-doped fibers [18].

Although the aforementioned DFOS showed great potential for distributed measurements, the low spatial resolution makes them less suited for distributed temperature and strain measurements in compact structures, such as batteries, robotic fingers, and printed circuit boards. Alternatively, Rayleigh backscattering-based (RBS-based) sensing, employing the interrogation technique of OFDR, showed tremendous potential for distributed temperature and strain measurements in compact structures [19] due to high spatial resolution (from a few centimeters to the sub-millimeter range), fast acquisition rate (a few hundred hertz) and reasonable sensing length (a few tens of meters). The RBS-based sensing technology showed considerable growth due to ongoing efforts on the development of the OFDR interrogation technique. Froggatt et al. demonstrated that distributed strain measurements could be performed with a spatial resolution of 6 mm [2]. Gifford et al. presented a distributed temperature sensor that performed measurements with

a spatial resolution of 2 mm [1]. Gifford et al. also investigated the relationship between the spatial resolution and the measurement accuracy of the proposed RBS-based sensor.

Rayleigh backscattering-based (RBS-based) fiber-optic sensors have emerged as a promising sensing solution, primarily for distributed temperature and strain measurements. The RBS-based temperature and strain sensors have been reported for a range of applications, including but not limited to energy generation systems [20]–[22], high-temperature steel industry applications [23], [24], health monitoring of mechanical and civil engineering structures [25], robotics [19], and medical instruments [26]. The concept of distributed sensing using RBS has been extended to the measurement of refractive index [27]–[29], vibration [30], and pressure [3]. The sensing method exploits RBS signals in single-mode optical fibers. Optical fibers have intrinsic in-homogeneities in their material that give rise to microscopic fluctuations in the refractive index profile. The light scattered from in-homogeneities in the core of a single-mode optical fiber results in a unique Rayleigh signature for the fiber [31]. The unique and stable Rayleigh signature in a single-mode optical fiber, under steady-state conditions, is the basis for RBS-based sensing.

The standard single-mode optical fiber (SMF) used in RBS-based sensing is an off-the-shelf optical fiber designed for long-distance optical communications. The weak RBS (~1 ppm) in a SMF is a significant contributor to the transmission loss and is considered an undesirable phenomenon for long-distance communication applications. However, the RBS has been exploited to perform distributed fiber-optic sensing. The weak Rayleigh signals require a sophisticated interrogation technique, such as OFDR [9], [32]. The highlight of the OFDR technique is the capability of performing spatially distributed measurements along the length of optical fibers with sub-millimeter spatial resolution. A

single continuous optical fiber can replace thousands of point sensors by providing thousands of measurement points along its length [23], [33].

In order to measure spatially distributed temperature or strain, optical fibers need to be glued on the surface of or embedded inside the target structures. The deployment of optical fibers for sensing often requires bending, unavoidable in a number of applications, such as healthcare assistive devices [34], [35], thermal mapping during tumor heat treatments, temperature measurements in metal casting molds, temperature or strain mapping in batteries, and structural health monitoring [36]. Bending optical fibers during deployment reduces the strength of the already weak Rayleigh signals and results in a reduced signal-to-noise ratio (SNR) for the OFDR measurements. The low SNR reduces measurement accuracy and degrades spectral shift resolution. The degradation in spectral shift resolution deteriorates measurement resolutions of temperature and strain. Although the spatial resolution of the OFDR system is primarily determined by the tuning range of the tunable laser source (TLS) in the system, the low SNR also has adverse effects on the spatial resolution of the system. A lower SNR forces the selection of a wider data window (more data samples) for the cross-correlation process to produce a measurement point, reducing the spatial resolution. Therefore, improving the SNR is pivotal for temperature and strain measurements with reliable measurement resolution and high spatial resolution.

Various attempts have been made to enhance the RBS signals in SMFs. One of the methods employed involves making index modifications within the core of the SMF using femtosecond laser micromachining techniques [21]. Another approach to enhance RBS signals consists of exposing the core of the SMF to UV light [37]. Yan et al. reported distributed fiber-optic sensors for real-time monitoring of solid oxide fuel cells using the

femtosecond laser micromachining technique [21]. The RBS signals in SMFs were enhanced by more than 40 dB by making index modifications in the core using laser pulses. Loranger et al. demonstrated that RBS signals in SMFs could be enhanced by exposing the core of the fiber to UV light [37]. The hydrogen-loaded core of an SMF-28 was exposed to UV light, and a ten-fold enhancement in RBS signals was achieved. Another approach to enhance RBS signals involves doping the core with MgO, such that stronger scattering centers are created inside the core of the optical fiber [38]. Beisenova et al. demonstrated an enhancement of 36.5 dB in RBS signals using a fiber doped with MgO nanoparticles [38]. The aforementioned techniques enhance RBS signals, but they also introduce high transmission losses and require special treatments of standard SMFs.

Another approach to address the limitations caused by weak RBS signals is to reduce the macrobending loss of the fiber. The improved bending performance would protect RBS signals during fiber deployment and would ensure that the SNR is high enough to be used in an OFDR system. The macrobending loss in an optical fiber is related to the refractive index (RI) contrast between the core and cladding of the fiber. The RI contrast is also defined in terms of the numerical aperture (NA). The macrobending loss in SMFs will be reduced by increasing the NA of the fiber [39]. However, in order to achieve single-mode operation with a high-NA fiber, the diameter of the core must be reduced. Therefore, we propose a thin-core high-NA (TC-HNA) fiber as a promising candidate for sensing applications that require sharp permanent bends in deployed optical fibers.

Previous studies have exploited the feasibility of using a photonic crystal fiber (PCF) and a ring-core fiber for bending-loss-resistant distributed sensing [40], [41]. Naeem et al. reported a Ge-doped-core PCF for bending-loss-resistant temperature and strain

measurements in RBS-based sensing [40]. A bending radius down to 1-mm was achieved. Distributed temperature sensing was demonstrated up to 120 ℃ using the proposed fiber. The stability of a Ge-doped-core PCF at elevated temperatures is yet to be reported. Another drawback of realizing distributed sensing using a PCF could be the high cost of the fiber. Nevertheless, the proposed fiber demonstrated that temperature and strain measurements could be performed with minimal bending-loss. Shen et al. reported a ring-core fiber (RCF) for distributed curvature sensing using Brillouin optical time-domain interrogation [41]. A sharp bending radius down to 5-mm was achieved with the RCF. However, the RCF exhibits several modes, and the performance of the fiber for RBS-based sensing has yet to be investigated.

For the first time to the best of our knowledge, a TC-HNA fiber was investigated as a potential sensor device for RBS-based sensing systems. The TC-HNA fiber not only exhibits superior bending performance but also offers a 6 dB enhancement in RBS signals. The experiments revealed that the RBS signals from the TC-HNA fiber, with a single turn of ~1 mm bending radius, could be employed for sensing applications. The temperature and strain measurements performed using the TC-HNA fiber provided evidence that the fiber could be used for reliable measurements. The bending performance of the TC-HNA fiber was compared with that of a standard SMF. The results demonstrated that the macrobending loss in the TC-HNA fiber was significantly lower than that of a standard SMF. A temperature mapping experiment was also performed to illustrate the measurement capability of the TC-HNA fiber when configured with multiple sharp bends. The resistance of the TC-HNA fiber to reductions in signal transmissions from sharp bending allows temperature and strain mapping of small and irregular objects using a single continuous

looped fiber. The capability of the TC-HNA fiber to undergo sharp bends without losing significant signal power could be very useful in compact fiber packaging and other useful deployments.

2. MACROBENDING LOSS IN SINGLE-MODE OPTICAL FIBERS

Macrobending loss is the attenuation in optical signal as a result of light coupling from guided core modes to radiated cladding modes due to bending in an optical fiber. The macrobending loss in a SMF is often modeled as a tilt in the apparent RI profile of the optical fiber. As the bending radius is reduced, the tilt in the RI profile increases [21]. The increased tilt in the RI profile reduces the RI contrast between the core and cladding of an optical fiber in the bent section. The narrow contrast deteriorates the ability of an optical fiber to effectively guide light and leads to light leakage in the bending region. The macrobending loss increases with a decrease in the bending radius of optical fiber. The signal attenuation caused by macrobending rises exponentially below a bending radius called the critical radius of curvature. The critical radius of curvature for a step-index single-mode optical fiber (R_{cs}) can be estimated as [42]:

$$R_{cs} \simeq \frac{20\lambda}{(n_1 - n_2)^{3/2}} \left(2.748 - 0.996 \frac{\lambda}{\lambda_c} \right)^{-3} \tag{1}$$

where λ is the operating wavelength, n1 is RI of the core, n2 is RI of the cladding, and λc is the cutoff wavelength. The smaller the value of Rcs, the higher the ability of an optical fiber to mitigate macrobending loss. Eq. (1) suggests that Rcs could be decreased by adjusting parameters like n_1, n_2, and λ_c. The most common way to improve macrobending

loss-resistance is to increase the RI contrast between the core and cladding of an optical fiber, or in other words, to increase the NA of the optical fiber [39]. The increased RI contrast improves light confinement in the core by reducing R_{cs} of the fiber.

As discussed earlier, the standard SMF, commonly exploited in RBS-based sensing, is an off-the-shelf fiber designed for optical communications. The standard SMF has a narrow RI contrast between the core and cladding. Typically, the standard SMF exhibits a significant transmission loss for a bending radius below 10 mm [43]. A high-NA fiber, on the other hand, could bend sharper without experiencing significant loss due to bending. Therefore, a high-NA single-mode fiber with a reduced core diameter (to maintain single-mode operation) is a promising candidate for RBS-based spatially distributed sensing where sharp bending of the test optical fiber is unavoidable.

3. PRINCIPLE OF RBS-BASED MEASUREMENTS AND EXPERIMENTAL SETUP

3.1. RBS-BASED TEMPERATURE AND STRAIN MEASUREMENTS

RBS-based sensing is a truly distributed sensing technique that provides spatially continuous temperature and strain measurements along the length of optical fibers. Rayleigh scattering originates due to the scattering of light by in-homogeneities in optical fibers. Temperature and strain variations cause changes in both the refractive index and the length of an optical fiber, which result in shifts in the Rayleigh backscattering (RBS) spectra. Changes in temperature and strain can be measured by measuring shifts in RBS spectra. The RBS shift $\Delta\lambda$ caused by changes in temperature (ΔT) and strain ($\Delta\varepsilon$) is given as:

$$\Delta\lambda = \lambda[(\alpha + \zeta)\Delta T + (1 + P_\varepsilon)\Delta\varepsilon] \quad (2)$$

where λ is the operating wavelength; α is the thermal expansion coefficient (0.55×10^{-6} /°C); ζ is the thermo-optic coefficient (8.5×10^{-6} /°C); and, $P\varepsilon$ is the photoelastic coefficient of the optical fiber.

3.2. THE OFDR INTERROGATOR

A commercially available OFDR interrogator (LUNA ODiSI 6100) was employed to interrogate RBS signals obtained from standard SMF and TC-HNA fibers in demonstration experiments. The OFDR interrogator used a TLS with a 50 nm tuning range (1515–1565 nm) and a 1000 nm/s tuning speed. The interrogator can perform distributed temperature and strain measurements along a single-mode optical fiber over distances of up to 50 m. The system offers a maximum spatial resolution of 0.65 mm. The measurement rate can be as high as 250 Hz.

3.3. STANDARD SINGLE-MODE OPTICAL FIBER AND THIN-CORE HIGH-NA FIBER

The standard single-mode optical fiber (SMF) used in the experiments was the SMF-28 Ultra Optical Fiber from Corning (Corning, NY). The thin-core high-NA (TC-HNA) fiber was the UHNA1 from Nufern (East Grandby, CT). Figure 1 shows microscope images of a standard SMF and a TC-HNA fiber. The standard SMF has a core diameter of 8.2 μm (as shown in Figure 1(a)), NA of 0.14, mode field diameter (MFD) of 10.4 ± 0.8 μm at the wavelength of 1550 nm, and a cladding diameter of 125 ± 0.7 μm. The TC-HNA fiber has a core diameter of 2.5 μm (as shown in Figure 1(b)), NA of 0.28, MFD of 4.8 ± 0.3 μm at the wavelength of 1550 nm, and a cladding diameter of 125 ± 1 μm. The high

NA and small MFD of the TC-HNA fiber provide superior macrobending performance, as discussed in Section 2.

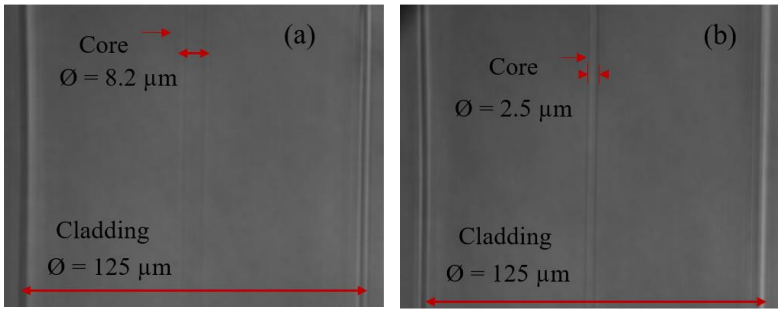

Figure 1. Microscope images of a standard SMF and a TC-HNA fiber. (a) An image of a standard SMF showing diameters (denoted by ⌀) of the core and cladding. (b) An image of a TC-HNA fiber showing diameters (denoted by ⌀) of the core and cladding.

4. EXPERIMENTS

4.1. TEMPERATURE AND STRAIN CALIBRATIONS

Experiments were designed and conducted to compare the performance of the standard SMF and the TC-HNA fiber for RBS-based distributed temperature and strain measurements. The standard SMF has been successfully used as a sensing device for distributed temperature and strain measurements in our laboratory over the past several years. A temperature-ramp experiment was performed to demonstrate the reliability of the TC-HNA fiber as a sensing device in RBS-based temperature measurements. The standard SMF and TC-HNA fiber, both connected to the eight-channel OFDR interrogator, were placed in a tube furnace (Thermo scientific TF55030A-1). Both fibers were terminated outside the furnace using a coreless fiber to reduce end reflections. A K-type thermocouple was also centrally placed in the furnace, parallel to the optical fibers. The thermocouple

was connected to a data logger (Graphtec GL220). The furnace was heated from room temperature (22 ℃) to 400 ℃ with an average ramp-up rate of ~20 ℃/min. The shifts in Rayleigh spectra along the standard SMF and the TC-HNA fiber were measured with a 1.3-mm spatial resolution. The measurements were recorded with an update rate of 1 Hz. The thermocouple system measured temperature at a single location with an update rate of 1 Hz. Figure 2 shows shifts in Rayleigh spectra along the standard SMF and the TC-HNA fiber. Both fibers exhibited similar spectrum shift profiles for the entire duration of the temperature ramp-up experiment, as evident from Figure 2(a) and (b). The TC-HNA fiber exhibited a slightly higher spectrum shift than the spectrum shift registered by the standard SMF. The spectrum shift measurements were converted into temperatures using the temperature data obtained by the thermocouple. The locations on the standard SMF and the TC-HNA fiber, close to the tip of the thermocouple probe, were identified using localized heating before the start of the experiment. Figure 3 shows the spectrum shift at a single location of the standard SMF and the TC-HNA fiber at various temperatures, ranging from room temperature (22 ℃) to 400 ℃. Second-order polynomials were fitted to the data in order to generate calibration curves for the standard SMF and the TC-HNA fiber. The relationship between the spectrum shift and the temperature is given below as:

$$f(T) = A + B \times T + C \times T^2 \tag{3}$$

where f is the spectrum shift in GHz, T is the temperature in ℃, and A, B, and C are fit parameters. The fit parameters for both the standard SMF and the TC-HNA fiber are provided in Table 1. The spectrum shift for the TC-HNA fiber is slightly higher than that of the standard SMF, as evident from Figure 3. The higher spectrum shift is possibly due

to the higher thermo-optic coefficient of TC-HNA fiber. The TC-HNA fiber has more doping in the core that could contribute to the higher value of the thermo-optic coefficient.

Table 1. The fit parameters for standard SMF and TC-HNA fiber.

	A (GHz)	*B* (GHz/°C)	*C* (GHz/°C^2)
Standard SMF	-21.82	1.272	0.0007788
TC-HNA fiber	-18.19	1.293	0.0008507

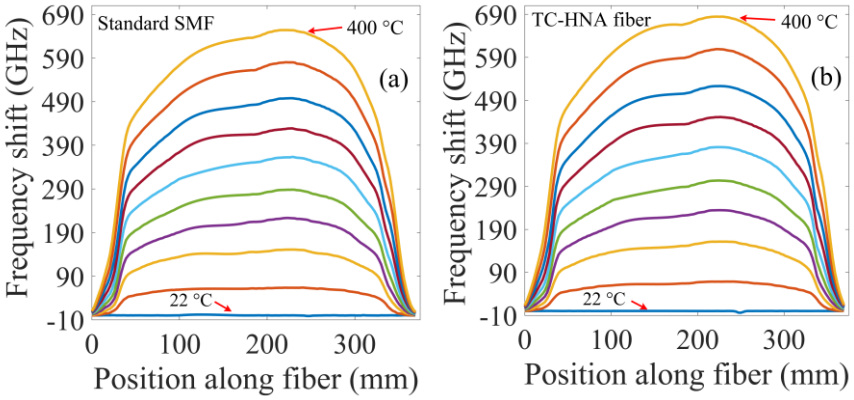

Figure 2. Comparison of frequency shift profiles along a standard SMF and a TC-HNA fiber obtained during a temperature-ramp experiment. Both a standard SMF and a TC-HNA fiber were heated in a tube furnace with an average temperature ramp-up rate of ~20 °C/min. The frequency shift profiles were recorded using an OFDR interrogator. (a) The shifts in Rayleigh spectra along a standard SMF during the temperature ramp-up. (b) The shifts in Rayleigh spectra along a TC-HNA fiber during the same temperature ramp-up.

Next, an experiment was conducted to test the RBS-based spatially distributed strain measurement capability of the TC-HNA fiber. Two positions of the TC-HNA fiber (10 cm apart) were fixed on two translation stages. A 10-cm section of a standard SMF was also fixed to the same translation stages, parallel to the TC-HNA fiber. Stress was

applied to both fibers by moving one of the translation stages outwards, simultaneously stretching both fibers. The applied stress increased the measured strain from 0–1000 με with a step-size of 100 με.

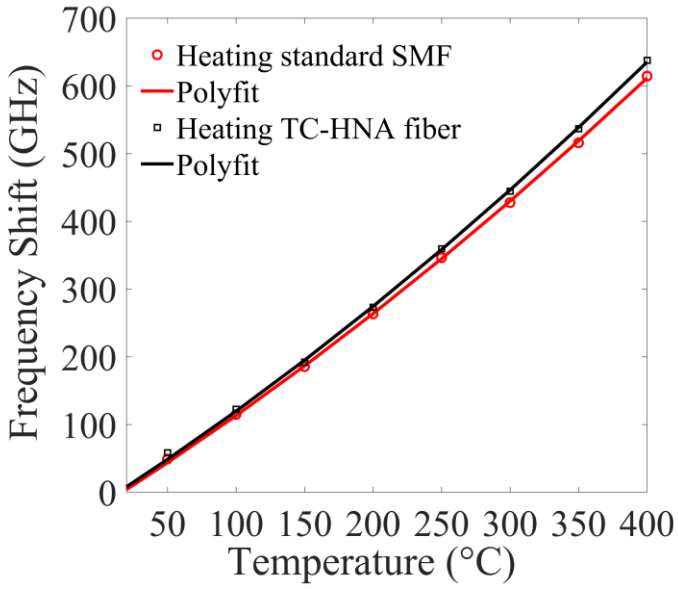

Figure 3. Frequency shift at a single location of the standard SMF and the TC-HNA fiber at various temperatures. Second-order polynomials were fitted to the data.

Figure 4 presents a comparison of frequency shift profiles along the standard SMF and the TC-HNA fiber obtained for various strains. Figure 4(a) and (b) show shifts in Rayleigh spectra along the standard SMF and the TC-HNA fiber, respectively, for various strains. Figure 5 shows spectrum shift as a function of strain, at a single location, for both the standard SMF and the TC-HNA fiber. Linear relationships between spectrum shift and strain were observed for both the fibers. However, as evident from Figure 5, the strain sensitivity for the TC-HNA fiber (0.178 GHz/ με) was significantly higher than that for the standard SMF (0.129 GHz/ με). The higher strain sensitivity for the TC-HNA fiber could

possibly be due to the higher photoelastic coefficient of the TC-HNA fiber. The experiments performed for the temperature and strain calibrations of the TC-HNA fiber demonstrated that the TC-HNA fiber works well for RBS-based temperature and strain measurements.

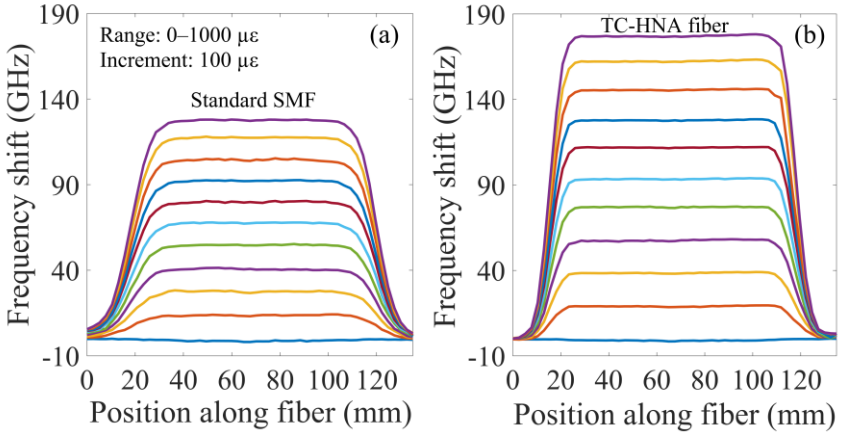

Figure 4. Comparison of frequency shift profiles along a standard SMF and a TC-HNA fiber obtained for various strains. (a) The shifts in Rayleigh spectra along a standard SMF for various strains ranging from 0 με to 1000 με (b) The shifts in Rayleigh spectra along a TC-HNA fiber for various strains ranging from 0 με to 1000 με.

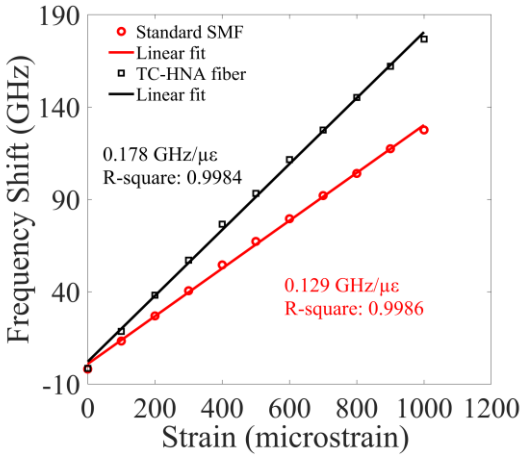

Figure 5. Frequency shift at a single location on a standard SMF and a TC-HNA fiber for various strains. Linear fittings were applied to the data.

4.2. COMPARISON OF MACROBENDING LOSS IN STANDARD SMF AND TC-HNA FIBER

The purpose of this study is to demonstrate the superior macrobending performance of TC-HNA fibers in RBS-based sensing systems. As discussed earlier, the low macrobending loss of TC-HNA fibers could make possible temperature and strain maps of objects where sharp bends are required for placement of the fiber. Despite the moderate success of RBS-based sensing, the range of applications is still limited due to the fact that standard SMF cannot maintain sharp bends in functional deployments. The high macrobending loss in standard SMFs severely deteriorate RBS signals and lead to the failure of RBS-based sensing. A single-mode optical fiber that offers low macrobending loss would significantly extend the range of applications for RBS-based sensing.

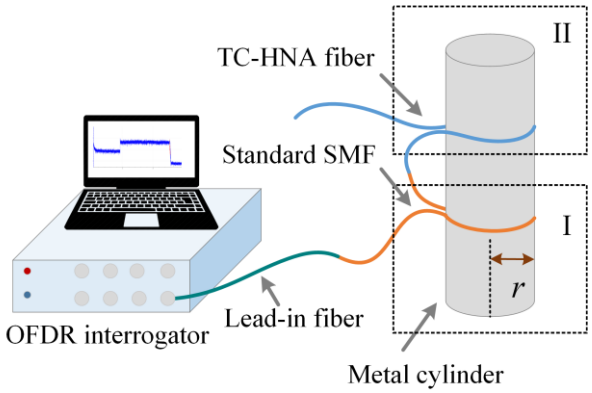

Figure 6. A schematic illustration of the test configuration used to compare macrobending loss in a standard SMF and a TC-HNA fiber. A lead-in optical fiber, connected to the OFDR interrogator, was spliced to a standard SMF, which was then spliced to a TC-HNA fiber. In a series of experiments, the standard SMF and TC-HNA fiber were wound (one test fiber at a time) around metal cylinders of radii 12.5 mm, 9 mm, 7 mm, 5 mm, 3 mm, 1.5 mm, and 0.9 mm in turn. When the standard SMF was wound around one of the cylinders, the TC-HNA fiber was kept straight, and vice versa. r: radius of the metal cylinder, I: test configuration for standard SMF, II: test configuration for TC-HNA fiber.

Experiments were conducted to compare the macrobending loss in a standard SMF and in a TC-HNA fiber for various fiber bending radii. A lead-in optical fiber, connected to the OFDR interrogator, was spliced to a 0.9-meter section of a standard SMF. The other end of the standard SMF was spliced to a 1.6-meter section of a TC-HNA fiber. The other end of the TC-HNA fiber was spliced to a coreless fiber to reduce end reflections. Figure 6 illustrates the test configuration used to compare macrobending loss in both fibers. Short sections of the contiguous standard SMF and the TC-HNA fiber were wound (one test fiber at a time) around metal cylinders with different radii. When the standard SMF was wound around a cylinder, the TC-HNA was kept straight, and vice versa. The RBS signal for each bending experiment was recorded. Figure 7 shows side-by-side RBS signals for different bending radii from the standard SMF and the TC-HNA fiber. An enhancement of 6 dB in the RBS signal was observed for the TC-HNA fiber. Figure 7(a)–(d) show that both the standard SMF and the TC-HNA fiber did not exhibit any observable macrobending loss for bending radii of 12.5 mm and 9 mm. The standard SMF experienced a macrobending loss of ~3 dB and ~6 dB at bending radii of 7 mm and 5 mm, respectively, as shown in Figure 7(e) and (g), respectively. However, the TC-HNA fiber showed no observable deterioration in RBS signal strength at bending radii of 7 mm and 5 mm, as evident from Figure 7(f) and (h), respectively. At the bending radius of 3 mm, the RBS signal from the standard SMF degraded so adversely that the signal became unusable by the OFDR interrogator, as shown in Figure 7(i). The TC-HNA fiber, on the other hand, did not exhibit any sign of signal degradation at the bending radius of 3 mm, as shown in Figure 7(j). This comparative demonstration provided strong evidence about the superior macrobending loss-resistance of the TC-HNA fiber. To further test the capability of sharp bending of the

TC-HNA fiber, two more experiments were performed at bending radii of 1.5 mm and 0.9 mm.

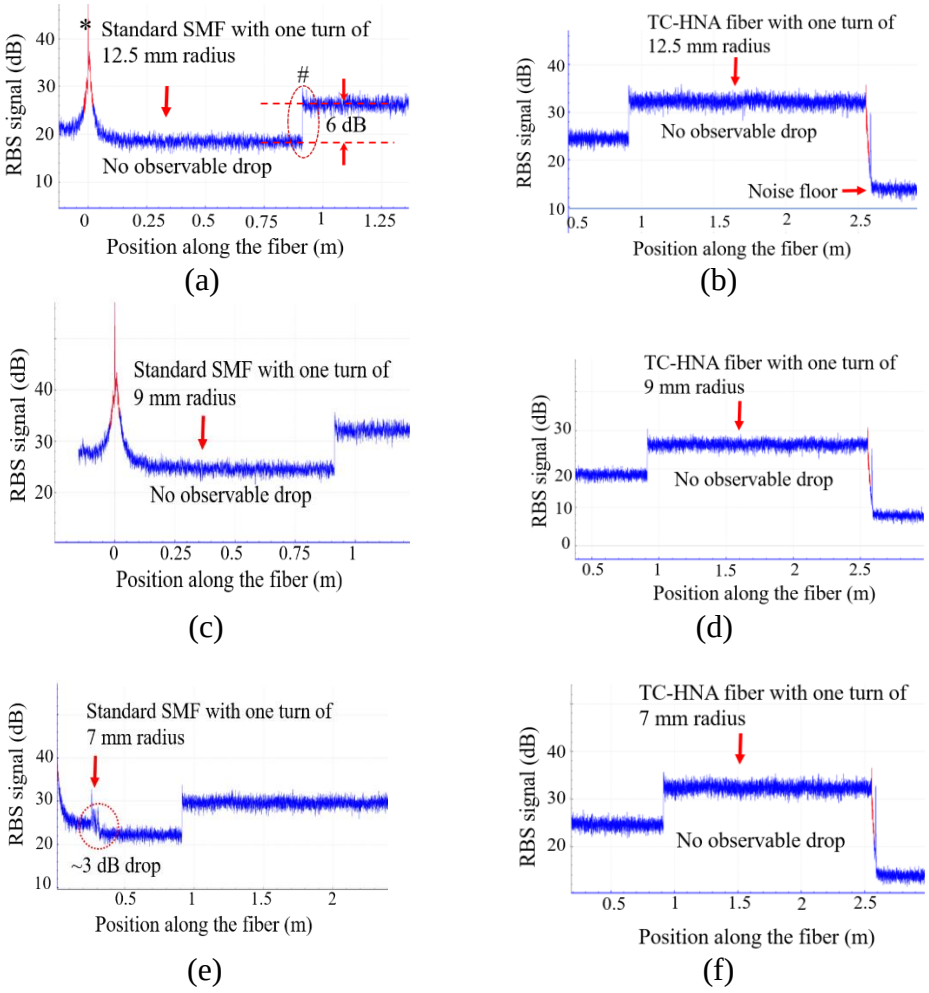

Figure. 7. Comparison of macrobending loss in a standard SMF and a TC-HNA fiber under static conditions of various bending radii. Relative intensities of RBS signal vs. position along a standard SMF and a TC-HNA fiber configured with a single turn of bending radius of (a)–(b) 12.5 mm, (c)–(d) 9 mm, (e)–(f) 7 mm, (g)–(h) 5 mm, and (i)–(j) 3 mm. Only a TC-HNA fiber was tested with bending radii of (k) 1.5 mm and (l) 0.9 mm. The asterisk sign (*) in (a) indicates the starting position of the standard SMF, and the number sign (#) marks the position where the standard SMF was spliced to the TC-HNA fiber. An enhancement of 6 dB was observed in the RBS signal obtained from the TC-HNA fiber.

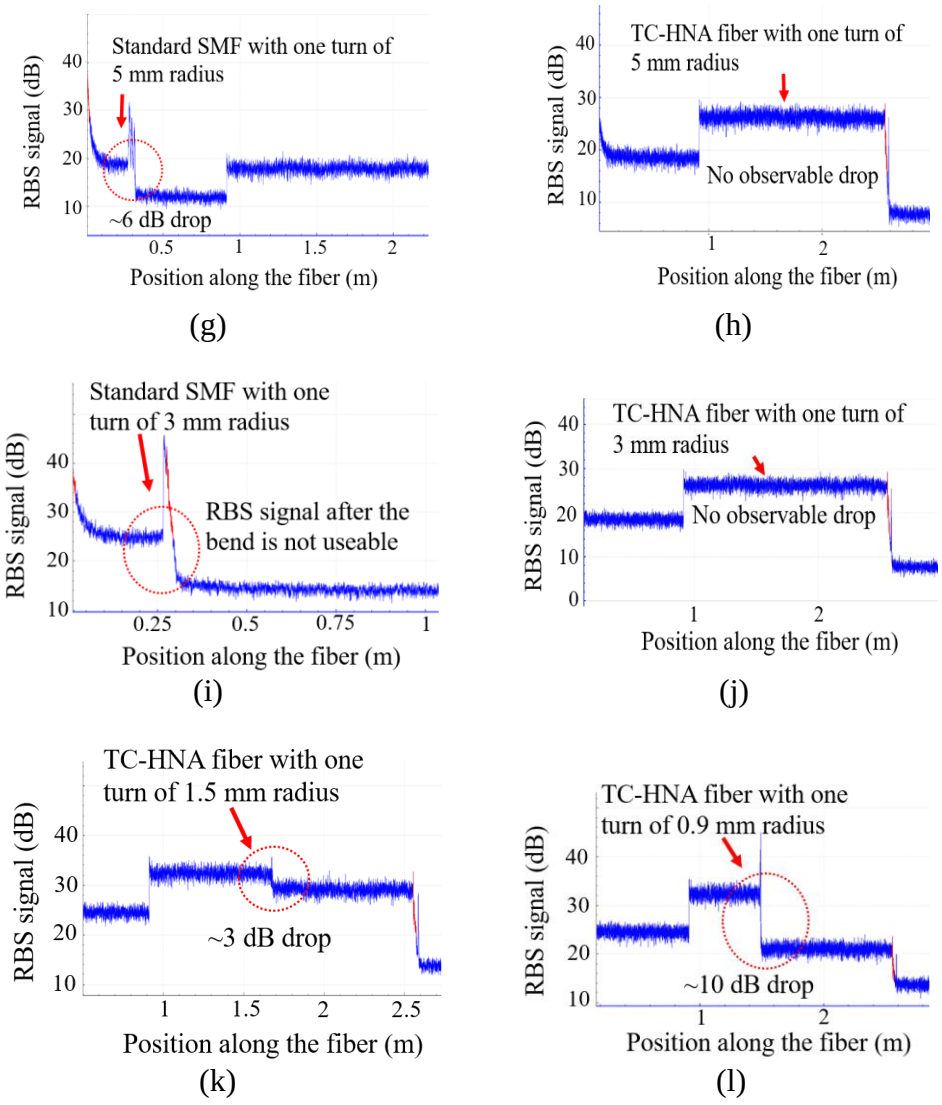

Figure. 7. Comparison of macrobending loss in a standard SMF and a TC-HNA fiber under static conditions of various bending radii. Relative intensities of RBS signal vs. position along a standard SMF and a TC-HNA fiber configured with a single turn of bending radius of (a)–(b) 12.5 mm, (c)–(d) 9 mm, (e)–(f) 7 mm, (g)–(h) 5 mm, and (i)–(j) 3 mm. Only a TC-HNA fiber was tested with bending radii of (k) 1.5 mm and (l) 0.9 mm. The asterisk sign (*) in (a) indicates the starting position of the standard SMF, and the number sign (#) marks the position where the standard SMF was spliced to the TC-HNA fiber. An enhancement of 6 dB was observed in the RBS signal obtained from the TC-HNA fiber. (cont.)

The RBS signal showed a drop of ~3 dB at the bending radius of 1.5 mm (see Figure 7(k)) and ~10 dB at the bending radius of 0.9 mm (see Figure 7(l)). Notably, the RBS signal

from the TC-HNA fiber, configured with the smallest bending radii, was still useable for the OFDR interrogator to perform distributed temperature and strain measurements. The significant improvement in the macrobending loss-resistance makes the TC-HNA fiber an exciting prospect for RBS-based temperature and strain measurements in a variety of applications that require sharp bends in the fiber.

Table 2 summarizes the distributed sensing capability of a standard SMF and a TC-HNA fiber for various fiber bending radii.

Table 2. Distributed sensing capability of a standard SMF and a TC-HNA fiber for a single turn of various fiber bending radii*.

Bending radius (mm)	Standard SMF	TC-HNA fiber
12.5	✓	✓
9	✓	✓
7	✓	✓
5	✓	✓
3	✗	✓
1.5	✗	✓
0.9	✗	✓[#]

[*] A green checkmark indicates that the fiber can be used for RBS-based sensing under conditions of the indicated bending radius, and a red cross mark indicates the failure of RBS-based sensing due to a high macrobending loss.

[#] Although the TC-HNA fiber exhibited a macrobending loss of ~10 dB at the bending radius of 0.9 mm, the RBS signal was still useable because an enhancement of 6 dB in the RBS signal was achieved for the TC-HNA fiber.

4.3. THERMAL MAPPING USING A CONTINUOUS TC-HNA FIBER WITH MULTIPLE LOOPS WITH SHARP BENDS

There are many applications that require temperature and strain mapping of compact objects. Several examples include thermal mapping of printed circuit boards and batteries [44], [45]. RBS-based sensing using a standard SMF for such applications is very challenging due to the low-bending requirement of the fiber. Replacing a standard SMF with a TC-HNA fiber would make deployment of the fiber easier due to the low macrobending loss demonstrated for TC-HNA fibers. An experiment was conducted to demonstrate the thermal mapping capability of a TC-HNA fiber configured with multiple loops with sharp bends. Figure 8 shows the test configuration used to perform thermal mapping of a metal plate and a corresponding representative plot of the spatial temperature profile recorded with an OFDR interrogator. Figure 8(a) illustrates a schematic of the test configuration where a continuous looped TC-HNA fiber was used to arrange six parallel passes of the fiber on the surface of a metal plate. Each parallel pass of the fiber was separated by a distance of 2 mm. The radius of each return bend of the fiber loop was ~2–3 mm. The other side of the metal plate was heated by placing it on a hot plate. Figure 8(b) shows a representative plot of spatially distributed temperatures along the fiber strands placed on the metal plate and the sections of fiber looped between consecutive parallel passes. The spatially distributed temperatures were recorded with a spatial resolution of 1.3-mm. The temperature profile plot demonstrated that temperature measurements could be successfully performed with a TC-HNA fiber despite multiple loops with sharp bends. The temperature mapping experiment provided strong evidence that the TC-HNA fiber could be useful in applications that require thermal mapping of compact objects.

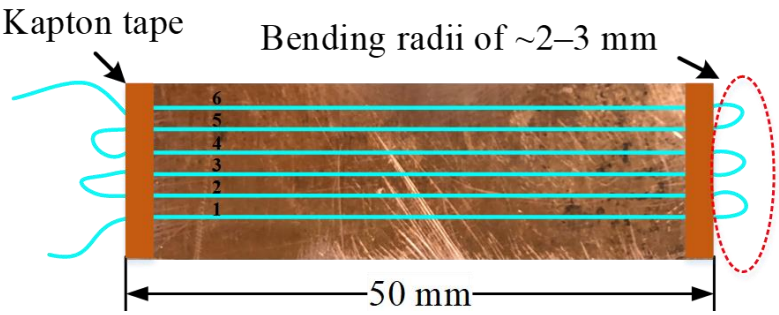

(a)

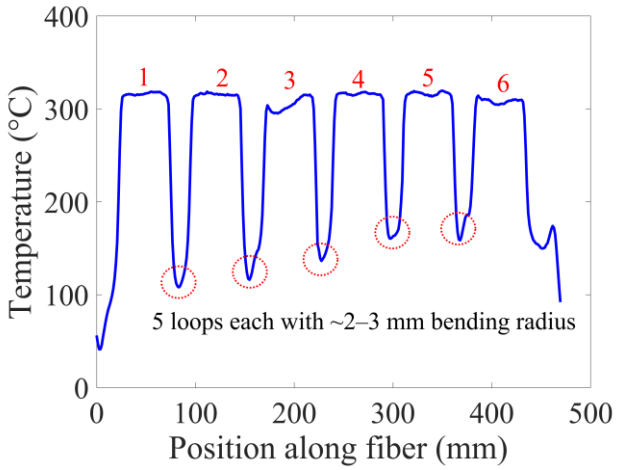

(b)

Figure. 8. A thermal mapping experiment of a block of copper metal employing a continuous single TC-HNA fiber attached to the plate and configured with multiple return loops with sharp bends. (a) Schematic of an arrangement of six sections of a continuous single TC-HNA fiber mounted on a metal plate and configured with multiple return loops at both ends of the plate. (b) Plot of spatially distributed temperature measurements along straight sections of the fiber placed on the metal plate. Red circles indicate the looped sections of the TC-HNA fiber between consecutive parallel passes on the plate surface.

Table 3 summarizes and compares a few significant features and measurement capabilities of the TC-HNA fiber and other low bending-loss fibers reported for distributed sensing—Ge-doped-core PCF [38] and ring-core fiber [39].

Table 3. Comparison of significant features and measurement capabilities of the TC-HNA fiber and other low bending-loss fibers reported for distributed sensing.

	TC-HNA fiber	Ge-doped-core PCF	Ring-core fiber
Sensing method employed	Rayleigh OFDR	Rayleigh OFDR	Brillouin OTDA
Minimum bending radius demonstrated	1 mm	1 mm	5 mm
Demonstrated measured temperatures	up to 400 ℃	up to 120 ℃	up to 60 ℃
Commercial availability	available	not available	available
Cost per meter	~$8	~$800 (for PCF)	~$10

5. CONCLUSION

A thin-core high-numerical-aperture (TC-HNA) fiber was employed to demonstrate the concept of bending loss-resistant temperature and strain measurements using Rayleigh backscattering-based (RBS-based) sensing methods. Experiments were designed and conducted to compare the temperature and strain measurement capabilities of a TC-HNA fiber with those of a standard single-mode fiber (SMF). The TC-HNA fiber provided reliable measurements. The macrobending loss in a standard SMF and a TC-HNA fiber were compared for different bending radii ranging from 12.5 mm down to 0.9 mm. The RBS signal for a standard SMF, with a single turn of 5 mm bending radius, degraded

severely, exhibiting 6 dB loss. The RBS signal was not useable for bending radii less than 3 mm. In contrast to a standard SMF, a TC-HNA fiber did not exhibit any loss with a single turn of bending radii of 5 mm and 3 mm. Due to superior macrobending performance, the TC HNA fiber could be used for RBS-based measurements with a single turn of 0.9 mm bending radius. An experiment was designed and conducted to demonstrate the thermal mapping of the surface of a metal plate employing the capability of a single continuous TC-HNA fiber with multiple return loops with sharp bends. A TC-HNA fiber, due to its low macrobending loss, provides significant benefits in RBS-based temperature and strain measurements of compact structures.

ACKNOWLEDGMENTS

This research was funded by the Kent D. Peaslee Steel Manufacturing Research Center (PSMRC) at Missouri S&T.

REFERENCES

[1] D. K. Gifford, B. J. Soller, M. S. Wolfe, and M. E. Froggatt, "Distributed fiber-optic temperature sensing using Rayleigh backscatter," *IET Conf. Publ.*, vol. 2005, no. CP502, pp. 511–512, 2005.

[2] M. Froggatt and J. Moore, "High-spatial-resolution distributed strain measurement in optical fiber with Rayleigh scatter," *Appl. Opt.*, vol. 37, no. 10, pp. 1735–1740, 1998.

[3] C. Zhu, Y. Zhuang, and Y. Chen, "Distributed fiber-optic pressure sensor based on Bourdon tubes metered by optical frequency-domain reflectometry," *Opt. Eng.*, vol. 58, no. 07, p. 1, 2019.

[4] M. Shao, Y. Zang, X. Qiao, H. Fu, and Z. A. Jia, “Humidity Sensor Based on Hybrid Fiber Bragg Grating/Abrupt Fiber Taper,” *IEEE Sens. J.*, vol. 17, no. 5, pp. 1302–1305, 2017.

[5] B. Guan, H. Tam, X. Tao, and X. Dong, “Simultaneous Strain and Temperature Measurement Using a Superstructure Fiber Bragg Grating,” in *IEEE Photonics Technology Letters*, vol. 12, no. 6, pp. 675-677, June 2000, doi: 10.1109/68.849081.

[6] X. Zhou, Y. Dai, F. Liu, and M. Yang, “Highly Sensitive and Rapid FBG Hydrogen Sensor Using Pt-WO3 with Different Morphologies,” *IEEE Sens. J.*, vol. 18, no. 7, pp. 2652–2658, 2018.

[7] A. G. Leal-Junior *et al.*, “Quasi-Distributed Torque and Displacement Sensing on a Series Elastic Actuator’s Spring Using FBG Arrays Inscribed in CYTOP Fibers,” *IEEE Sens. J.*, vol. 19, no. 11, pp. 4054–4061, 2019.

[8] M. K. Barnoski and S. M. Jensen, “Fiber waveguides: a novel technique for investigating attenuation characteristics,” *Appl. Opt.*, vol. 15, no. 9, p. 2112, 1976.

[9] W. Eickhoff and R. Ulrich, “Optical frequency domain reflectometry in single-mode fiber,” *Appl. Phys. Lett.*, vol. 39, no. 9, pp. 693–695, 1981.

[10] H. Barfuss and E. Brinkmeyer, “Modified Optical Frequency Domain Reflectometry with High Spatial Resolution for Components of Integrated Optic Systems,” *J. Light. Technol.*, vol. 7, no. 1, pp. 3–10, 1989.

[11] G. Bolognini and A. Hartog, “Raman-based fibre sensors: Trends and applications,” *Opt. Fiber Technol.*, vol. 19, no. 6 PART B, pp. 678–688, 2013.

[12] J. Park *et al.*, “Raman-based distributed temperature sensor with simplex coding and link optimization,” *IEEE Photonics Technol. Lett.*, vol. 18, no. 17, pp. 1879–1881, 2006.

[13] A. Barrias, J. Casas, and S. Villalba, “A Review of Distributed Optical Fiber Sensors for Civil Engineering Applications,” *Sensors*, vol. 16, no. 5, p. 748, 2016.

[14] T. Horiguchi, K. Shimizu, T. Kurashima, M. Tateda, and Y. Koyamada, “Development of a Distributed Sensing Technique Using Brillouin Scattering,” *J. Light. Technol.*, vol. 13, no. 7, pp. 1296–1302, 1995.

[15] A. Wosniok, N. Nöther, and K. Krebber, “Distributed Fibre Optic Sensor System for Temperature and Strain Monitoring Based on Brillouin Optical-Fibre Frequency-Domain Analysis,” *Procedia Chem.*, vol. 1, no. 1, pp. 397–400, 2009.

[16] Y. Koyamada, Y. Eda, S. Hirose, S. Nakamuka, and K. Hogari, “Novel fiber-optic distributed strain and temperature sensor with very high resolution,” *IEICE Trans. Commun.*, vol. E89-B, no. 5, pp. 1722–1725, 2006.

[17] M. Cen, V. Moeyaert, P. Mégret, and M. Wuilpart, “Localization and quantification of reflective events along an optical fiber using a bi-directional TRA technique,” *Opt. Express*, vol. 22, no. 8, p. 9839, 2014.

[18] M. Silveira *et al.*, “Transmission–Reflection Analysis in high scattering optical fibers: A comparison with single-mode optical fiber,” *Opt. Fiber Technol.*, vol. 58, no. June, p. 102303, 2020.

[19] Y. Du, Q. Yang, and J. Huang, “Soft Prosthetic Forefinger Tactile Sensing via a String of Intact Single Mode Optical Fiber,” *IEEE Sens. J.*, vol. 17, no. 22, pp. 7455–7459, 2017.

[20] S. Rizzolo *et al.*, “Vulnerability of OFDR-based distributed sensors to high γ-ray doses,” *Opt. Express*, vol. 23, no. 15, p. 18997, 2015.

[21] A. Yan *et al.*, “Distributed Optical Fiber Sensors with Ultrafast Laser Enhanced Rayleigh Backscattering Profiles for Real-Time Monitoring of Solid Oxide Fuel Cell Operations,” *Sci. Rep.*, no. January, pp. 1–9, 2017.

[22] S. Rizzolo *et al.*, “Real time monitoring of water level and temperature in storage fuel pools through optical fibre sensors,” *Sci. Rep.*, vol. 7, no. 1, pp. 1–10, 2017.

[23] M. Roman *et al.*, “A Spatially Distributed Fiber-Optic Temperature Sensor for Applications in the Steel Industry,” *Sensors*, vol. 20, no. 14, p. 3900, Jul. 2020.

[24] M. Roman, D. Balogun, R. E. Gerald II, L. Bartlett, J. Huang, and R. J. O’malley, “Peritectic Behavior Detection in the Fe-C-Mn-Al-Si Steel System Using Fiber Optic Temperature Mapping,” *AISTech - Iron Steel Technol. Conf. Proc.*, 2020

[25] S. Jothibasu *et al.*, “Spatially continuous strain monitoring using distributed fiber optic sensors embedded in carbon fiber composites,” *Opt. Eng.*, vol. 58, no. 07, p. 1, 2019.

[26] F. Parent *et al.*, “Enhancement of accuracy in shape sensing of surgical needles using optical frequency domain reflectometry in optical fibers,” Biomed. Opt. Express vol. 8, no. 4, pp. 2210–2221, 2017.

[27] Y. Du, S. Jothibasu, Y. Zhuang, C. Zhu, and J. Huang, “Rayleigh backscattering based macrobending single mode fiber for distributed refractive index sensing,” *Sensors Actuators, B Chem.*, vol. 248, pp. 346–350, 2017.

[28] Z. Ding *et al.*, "Distributed refractive index sensing based on tapered fibers in optical frequency domain reflectometry," *Opt. Express*, vol. 26, no. 10, pp. 13042–13054, 2018.

[29] G. Y. Chen *et al.*, "Short-Range Non-Bending Fully Distributed Water/Humidity Sensors," *J. Light. Technol.*, vol. 37, no. 9, pp. 2014–2022, 2019.

[30] Z. Ding *et al.*, "Long-range vibration sensor based on correlation analysis of optical frequency-domain reflectometry signals," Opt. Express vol. 20, no. 27, pp. 28319–28329, 2012.

[31] Y. Du, S. Jothibasu, Y. Zhuang, C. Zhu, and J. Huang, "Unclonable Optical Fiber Identification Based on Rayleigh Backscattering Signatures," *J. Light. Technol.*, vol. 35, no. 21, pp. 4634–4640, 2017.

[32] Z. Ding, T. Liu, K. Liu, Y. Du, and D. Li, "Monitoring optical fiber sensor networks by optical frequency-domain reflectometry," *2012 Photonics Glob. Conf. PGC 2012*, pp. 1–3, 2012.

[33] C. Zhu, Y. Zhuang, B. Zhang, R. Muhammad, P. P. Wang, and J. Huang, "A Miniaturized Optical Fiber Tip High-Temperature Sensor Based on Concave-Shaped Fabry-Perot Cavity," *IEEE Photonics Technol. Lett.*, vol. 31, no. 1, pp. 35–38, 2019.

[34] A. G. Leal-Junior *et al.*, "Polymer optical fiber strain gauge for human-robot interaction forces assessment on an active knee orthosis," *Opt. Fiber Technol.*, vol. 41, no. February, pp. 205–211, 2018.

[35] A. G. Leal-Junior, C. R. Díaz, C. Leitão, M. J. Pontes, C. Marques, and A. Frizera, "Polymer optical fiber-based sensor for simultaneous measurement of breath and heart rate under dynamic movements," *Opt. Laser Technol.*, vol. 109, no. July 2018, pp. 429–436, 2019.

[36] P. Lu *et al.*, "Distributed optical fiber sensing: Review and perspective," *Applied Physics Reviews*, vol. 6, no. 4. American Institute of Physics Inc., p. 041302, 01-Dec-2019.

[37] S. Loranger, M. Gagné, V. Lambin-Iezzi, and R. Kashyap, "Rayleigh scatter based order of magnitude increase in distributed temperature and strain sensing by simple UV exposure of optical fibre," *Sci. Rep.*, vol. 5, no. May, pp. 1–7, 2015.

[38] A. Beisenova *et al.*, "Multi-fiber distributed thermal profiling of minimally invasive thermal ablation with scattering-level multiplexing in MgO-doped fibers," *Biomed. Opt. Express*, vol. 10, no. 3, p. 1282, 2019.

[39] M. J. Li *et al.*, “Ultra-low bending loss single-mode fiber for FTTH,” *Opt. InfoBase Conf. Pap.*, vol. 27, no. 3, pp. 376–382, 2008.

[40] K. Naeem, Y. S. Kwon, Y. Chung, and I. B. Kwon, “Bend-Loss-Free Distributed Sensor Based on Rayleigh Backscattering in Ge-Doped-Core PCF,” *IEEE Sens. J.*, vol. 18, no. 5, pp. 1903–1910, 2018.

[41] Li Shen *et al.*, “Distributed curvature sensing based on a bending loss-resistant ring-core fiber," Photon. Res. 8, 165-174 (2020)

[42] J. Senior, *Optical Fiber Communications: Principles and Practice*. GBR: Prentice Hall International (UK) Ltd., 1985.

[43] Q. Wang, G. Farrell, and T. Freir, “Theoretical and experimental investigations of macro-bend losses for standard single mode fibers,” *Opt. Express*, vol. 13, no. 12, p. 4476, 2005.

[44] L. H. J. Raijmakers, D. L. Danilov, R. A. Eichel, and P. H. L. Notten, “A review on various temperature-indication methods for Li-ion batteries,” *Appl. Energy*, vol. 240, no. July 2018, pp. 918–945, 2019.

[45] M. Nascimento, T. Paixão, M. S. Ferreira, and J. L. Pinto, “Thermal mapping of a lithium polymer batteries pack with FBGs network,” *Batteries*, vol. 4, no. 4, 2018.

III. THERMAL MAPPING OF METAL CASTING MOLD USING HIGH RESOLUTION DISTRIBUTED FIBER-OPTIC SENSORS

Muhammad Roman [1], Damilola Balogun [2], Chen Zhu [1], Laura Bartlett [2], Ronald J. O'Malley [2], Rex E. Gerald II [1], and Jie Huang [1, *]

[1]Department of Electrical and Computer Engineering, Missouri University of Science and Technology, Rolla, MO 65409, USA.

[2]Department of Material Science and Engineering, Missouri University of Science and Technology, Rolla, MO 65409, USA.

*Correspondence: jieh@mst.edu

ABSTRACT

This article reports a technique to embed optical fiber into a copper mold plate for generating high-density thermal maps of the mold during the process of metal casting. The temperature measurements were based on acquiring and interpreting Rayleigh backscattering (RBS) signals from embedded fiber, employing the interrogation technique of optical frequency domain reflectometry (OFDR). The instrumented mold plate was used to perform a cast-iron dip test and a steel dip test in a 200 lb induction furnace. The maximum temperatures recorded by the embedded fiber-optic sensors were 469 ℃ and 388 ℃ in the cast-iron and steel dip tests, respectively. The closely-spaced and rapidly fluctuating temperature features that were imparted to the mold wall during solidification were successfully mapped with a high spatial resolution (0.65 mm) and a fast measurement rate (25 Hz) using a commercial OFDR interrogator (LUNA ODiSI 6108). Moreover, the thickness of the solidified steel shell was measured, and a thickness map of the shell was generated. A good correlation was observed between the thickness of the solidified shell

and the temperature of the mold, as regions with higher and lower temperatures in the thermal profile of the mold corresponded to thicker and thinner areas on the shell, respectively. The dip testing experiments demonstrate that RBS-based fiber-optic sensing is a feasible and effective method for generating information-rich thermal maps of caster molds. The information obtained from thermal maps can be useful for improving the quality of the metal and productivity of the metal casting process.

Keywords: Caster mold, distributed sensing, fiber-optic sensing, metal casting, optical frequency domain reflectometry, Rayleigh scattering, thermal mapping.

1. INTRODUCTION

Temperature measurement in continuous casting molds is an effective tool to monitor process stability and quality of cast metal. The thermal response of a mold provides valuable insights into the solidification behavior of molten metal [1]. In the continuous casting of steel, various quality defects such as longitudinal cracks and stickers (sticker: a layer of metal adhered to a mold surface) originate at the meniscus [2]. These quality defects can lead to cast breakouts if appropriate and timely actions are not taken. It has been demonstrated that longitudinal cracks and stickers cause non-uniform heat flux from the metal to the mold. The non-uniform heat flux induces localized temperature variations at the surface of the mold. Real-time temperature monitoring of the mold can help in the early detection of such quality defects and the prevention of cast breakouts [3]. Moreover, it has been reported that inadequate mold lubrication also causes a substantial deviation in heat flux [2]. The thermal response of a caster mold provides data that can be used to

improve mold lubrication and produce high-quality steel products. The meniscus flow velocity of the molten steel in the continuous casting process is another important parameter that has a significant impact on steel quality [4], [5]. Measuring and controlling flow velocity is crucial for ensuring high-quality yield. The thermal profile of a caster mold can be used to estimate flow velocity [6]. Feedback from the temperature measurement system of the mold can be used to adjust flow velocity using a flow control system. In addition to a tool for quality assurance, real-time temperature monitoring of caster molds helps to improve production efficiency. Under extreme cases of casting defects, breakouts may occur, which leads to catastrophic damage to equipment, which results in production downtime. Early detection of cast defects and prevention of breakouts can ensure uninterrupted operation. Therefore, real-time temperature monitoring of caster molds provides information that can be useful to improve both quality and productivity.

Conventionally, thermocouples are widely used to perform temperature measurements in caster molds [2], [7]–[10]. However, the inability of thermocouples to perform spatially-distributed measurements with high spatial resolution limits their utility in the thermal mapping of caster molds. Furthermore, the instrumentation of caster molds with thermocouples requires machining of the molds to accommodate the probes. Given the sizes of these probes, the machining of the molds introduces problematic unaccounted measurement disturbances. To keep the integrity of the mold intact, the number of thermocouples integrated into the mold plates is limited. The large spacing between temperature measurement points creates dead zones on the mold surface. Localized temperature features appearing in those dead zones cannot be captured. Therefore, many quality defects on the solidified shell go undetected. The measurements from

thermocouples are also affected by electromagnetic systems, such as electromagnetic braking and stirring used for flow control in the continuous casting process. Recently, ultrasonic sensors have been reported for thermal mapping of molds in billet casters [11]. The sensors are mounted on the water jacket, and they can measure mold temperatures in the meniscus region. Although the ultrasonic sensors are non-intrusive, they cannot generate information-rich thermal maps due to a limited number of temperature measurement points. Infrared (IR) cameras are also used for temperature measurements in various steelmaking processes, such as slag detection [12] and steel rolling [13]. However, the accuracy of temperature measurements using an IR camera is affected by variations in the emissivity of the target surface. Besides, the hot face of a caster mold is not accessible to an IR camera; therefore, thermal mapping of mold surfaces using an IR camera is not easily achievable.

Alternatively, fiber-optic temperature sensors have been explored to achieve high-density thermal mapping of caster molds [6], [14]–[19]. Fiber-optic sensors offer various advantages over conventional sensors, such as the miniaturized size of the optical fiber, immunity to electromagnetic interferences, low thermal capacity, little intrusion into the system, multiplexing capability, remote operation, and the ability to withstand harsh environments. The distinct feature that makes fiber-optic sensors an exciting prospect for thermal mapping of caster molds is the innate capability of fiber-optic sensors to perform distributed sensing. Various fiber-optic sensors were reported for temperature measurements. These sensors include interferometers [20]–[22], fiber Bragg gratings (FBGs) [23], and scattering-based sensors [24], [25]. FBGs attracted considerable interest for thermal mapping of caster molds due to a quasi-distributed sensing capability with a

reasonable spatial resolution (~1 cm), high-temperature resolution (~0.1 °C), and fast measurement rates (up to a few kHz). Commercial implementations of mold monitoring systems based on FBGs include the HD (high-definition) mold and the OptiMold systems [6], [17]. In the HD mold, 120 FBG sensors, fabricated on 12 optical fibers, were embedded in the copper plate of the mold [15]. Krasilnikov et al. reported results using the HD mold [16]. Temperature measurements, recorded during the continuous casting of steel, were used to calculate local heat flux densities. The thickness profile of the solidified shell was subsequently calculated using heat flux measurements. Lieftucht et al. reported temperature measurements recorded with the HD mold during the continuous casting of steel [17]. Temperature measurements were used to calculate local heat flux readings over the mold height. Heat flux readings were used to calculate mold levels. The calculated mold levels were compared with steel level readings measured manually. In the OptiMold system, 38 optical fibers, each with 70 FBG sensors, were embedded in the upper half of a copper mold plate [18]. The embedded sensors provided a total of 2660 temperature measurement points. Seden et al. reported results using the OptiMold system in the continuous casting of steel [6]. The thermal profile of the mold was used to estimate the meniscus shape. Additionally, the thermal response of the mold was used to control the flow symmetry of the mold. Spierings et al. used thermal data of the mold, collected by the OptiMold system, to investigate mold fluid flow and properties of mold powder [19].

Although FBGs enjoy commercial success, they have some limitations pointed out hereafter. FBGs can only afford quasi-distributed sensing, so they have measurement dead zones along optical fibers that contain FBGs. Additionally, optical fibers need to be modified to fabricate gratings, which increases the cost of the optical fibers. Moreover, the

number of FBGs that can be interrogated along a single continuous optical fiber are limited. Therefore, the thermal mapping of caster molds may require multiple optical fibers. For example, 12 optical fibers were used in the HD mold to achieve 120 FBGs [17], and 38 optical fibers were used in the OptiMold to achieve 2260 FBGs [19]. Multiple lead-in optical fibers require complicated cable management. In addition, multiple optical fibers may require multiple light sources and detectors. For example, 3 broadband light sources were used to illuminate the optical fibers embedded in the OptiMold.

As opposed to quasi-distributed sensors where index modifications are artificially created inside optical fibers, truly distributed sensors rely on light scattering in unaltered optical fibers. Distributed fiber-optic sensors (DFOS) are mainly based on three types of scattering—Raman, Brillouin, and Rayleigh. The most commonly employed techniques to interrogate light scattering in optical fibers are optical time-domain reflectometry (OTDR) [26], optical time-domain analysis (OTDA) [27], and optical frequency-domain reflectometry (OFDR) [28]–[30]. DFOS based on Raman and Brillouin OTDR are suitable for temperature measurements in large structures, such as dams and bridges, due to the extended range of the sensors (kilometers). However, the low spatial resolution of such sensors (~ 1 m) makes them less suited for applications in steelmaking, where thermal mappings in compact structures are highly desirable. Considering the fact that sensors based on Raman and Brillouin OTDR and OTDA have low spatial resolution, DFOS based on Rayleigh OFDR were investigated for the thermal mapping of caster molds. The sensing method provides spatially continuous measurements along single-mode optical fibers [31]–[37]. The RBS-based sensing approach provides high spatial resolution (~0.5 mm), fast measurement rates (a few hundred Hz), and a reasonable sensing length of optical fiber (a

few tens of meters). RBS-based temperature sensors were reported for various settings, such as energy generation systems [38], [39] and high-temperature applications in the steel industry [34], [40]. RBS-based sensing could be an exciting prospect for the thermal mapping of caster molds. The ability to provide spatially continuous temperature measurements along an optical fiber can be useful in achieving thermal maps of a caster mold using a single continuous optical fiber, thus making cable management and interrogation a lot easier. Moreover, information-rich thermal maps of caster molds, achieved due to the sub-millimeter spatial resolution of the fiber-optic measurement system, can be instrumental in detecting closely spaced and rapid thermal events occurring at the meniscus.

In this paper, RBS-based sensing was used for thermal mapping in a caster mold. An instrumentation method was devised to embed an optical fiber in a copper mold plate for spatially-distributed temperature measurements. A high-numerical-aperture optical fiber, with high macrobending loss-resistance, was used to instrument a compact mold plate using a single continuous looped optical fiber. The instrumented mold plate was immersed in cast-iron melt (C 3.10%, Si 1.87%, Mn 0.5%, Cr 0.16%) at 1450 ℃ and in steel melt (C 0.2%, Si 2.0%, Mn 0.07%, Al 0.08%) at 1600 ℃. The silica optical fibers used in the mold instrumentation cannot withstand such high temperatures. Therefore, the optical fibers were protected from direct exposure to the molten metal. The work reported here was intended to measure temperatures in the mold as a result of transient heat transfer from metal to the mold during immersion and solidification. The maximum temperatures recorded by the embedded fiber-optic sensors were 469 ℃ and 388 ℃ in the cast-iron and steel dip tests, respectively. In both the cases, the metered temperatures remained well

below the maximum temperature measurement capability of RBS-based fiber-optic sensors, which is approximately 700–750 ℃ for unmodified silica optical fibers [41]. Thermal maps of the mold, generated during the immersion of the mold into the molten metal and solidification of the shell against the mold wall, provided valuable insights into the solidification behavior.

2. RBS-BASED TEMPERATURE MEASUREMENTS AND OFDR INTERROGATION

RBS-based sensing is a distributed sensing method that provides spatially continuous temperature measurements along single-mode optical fibers. The RBS effect derives from the scattering of light from fluctuations in refractive index in an optical fiber. The RBS-based temperature measurements rely on the fact that temperature variations cause shifts in the RBS spectra. The shifts in the RBS spectra are attributed to changes in the refractive index and the length of an optical fiber as a result of changes in temperature. The RBS shift ($\Delta\lambda$) caused by a change in temperature (ΔT) is given as:

$$\Delta\lambda = \lambda\,(\alpha + \zeta)\,\Delta T \tag{1}$$

where λ is the operating wavelength, α is the thermal expansion coefficient (0.55×10^{-6} /℃), and ζ is the thermo-optic coefficient (8.5×10^{-6} /℃) of the optical fiber.

A commercially available OFDR interrogator (LUNA ODiSI 6108) was used to interrogate RBS signals obtained from the optical fiber under test. The interrogator used a tunable laser source with a 50 nm tuning range (1515–1565 nm) and a 1000 nm/s tuning speed. The highest spatial resolution achieved using the interrogator was 0.65 mm (for a fiber length of up to 2.5 m with a measurement acquisition rate of 62 Hz). The maximum

measurement acquisition rate provided by the interrogator was 250 Hz (for a fiber length of up to 2.5 m with a spatial resolution of 2.6 mm). The measurement acquisition rate varies depending on the length of the sensing fiber and the spatial resolution used in the measurements. For a given spatial resolution, the measurement acquisition rate decreases with an increase in sensing fiber length. Similarly, for a given length of the sensing fiber, the measurement acquisition rate decreases with an increase in spatial resolution. The interrogator automatically adjusts the measurement acquisition rate based on the length of the sensing fiber used in the experiment and the value of spatial resolution selected for the measurements. The interrogator can perform distributed temperature measurements along a single-mode optical fiber over distances of up to 50 m.

3. EXPERIMENTAL SETUP FOR THE DIP TEST

The thermal mapping of a caster mold has great value in metal casting. As discussed earlier, real-time temperature monitoring of a mold has a significant role in improving the quality and productivity of the cast. The potential of RBS-based fiber-optic temperature measurement for real-time thermal mapping of the caster mold was demonstrated in a dip test. An instrumentation method was devised to embed optical fibers in copper mold plates. The objective was to conduct a dip test with an instrumented mold and generate thermal maps of the mold plate during immersion and solidification. Figure 1 shows a schematic of the experimental setup used to conduct the dip test with a mold instrumented with optical fibers. The dip test was conducted in a 200 lb induction furnace in the Missouri S&T foundry laboratory. A copper mold plate (100 mm × 50 mm × 12 mm thick) was

instrumented with an optical fiber for temperature measurements. The mold plate was housed in a metal casing to protect fiber loops from the molten metal during the dip test. One end of the optical fiber, used in the instrumentation of the mold plate, was connected to the OFDR interrogator. The other end of the optical fiber was placed inside the metal casing. The following sections present more details about the mold instrumentation and the experimental setup of the dip test.

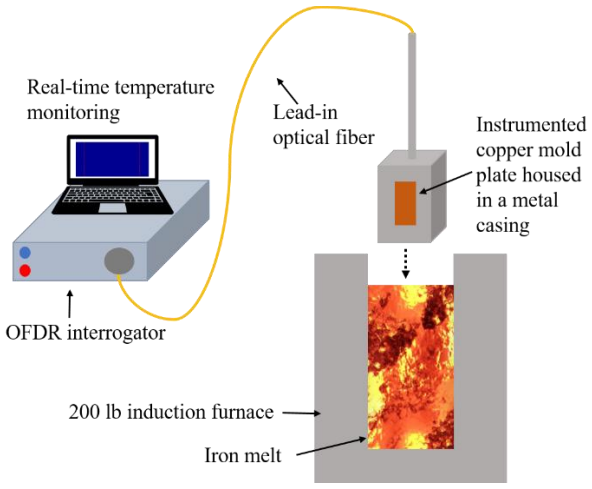

Figure 1. Schematic overview of the experiment setup of the dip test using a copper mold instrumented with distributed fiber-optic temperature sensors.

3.1. A HIGH-NA FIBER AS A SENSING DEVICE

The RBS-based temperature measurement system exploits an unmodified single-mode optical fiber as a sensing device. The optical fiber commonly used for the RBS-based measurements is a communication grade standard single-mode optical fiber (SMF). To instrument a mold plate using a single continuous optical fiber, the optical fiber needs to be looped, making multiple sensing paths. However, the compact mold plate requires sharp bending of the optical fiber for the embedding process. The standard SMF exhibits

significant attenuation in the RBS signal due to sharp bends. The attenuation in the RBS signal deteriorates the signal-to-noise ratio (SNR) and leads to the failure of OFDR measurements [42]. An optical fiber with a high numerical aperture (NA) was used to address the issue of signal attenuation due to bending. An optical fiber with a high NA diminishes macrobending loss and allows multiple sharp bends of the fiber under test [43]. The single-mode high-NA optical fiber used to instrument the mold was the UHNA1 from Nufern (East Grandby, CT). The UHNA1 fiber has a core diameter of 2.5 μm, NA of 0.28, mode field diameter of 4.8 ± 0.3 μm at the wavelength of 1550 nm, and a cladding diameter of 125 ± 1 μm. The high-NA fiber can be wrapped to a radius of a few millimeters without experiencing significant attenuation in the RBS signal.

3.2. TEMPERATURE COEFFICIENTS FOR THE HIGH-NA FIBER

The frequency shift response of the fiber-optic measurement system, as a result of changes in temperature, was measured and calibrated before the mold instrument was fitted with the fiber. In order to conduct a temperature-ramp experiment, a section of a high-NA optical fiber was placed in a tube furnace (Thermo scientific TF55030A-1). One end of the fiber was connected to the OFDR interrogator, and the other end was spliced to a coreless fiber positioned outside the furnace. The coreless fiber was used to reduce reflections from the end face of the high-NA optical fiber. A K-type thermocouple, connected to a data logger (Graphtec GL220), was placed together with the optical fiber for temperature measurements at a single position in the furnace. In order to compare a frequency shift profile recorded using the OFDR interrogator to the temperature profile measured with the thermocouple system, a position on the optical fiber, close to the tip of the thermocouple

probe, was identified using a point heating source before the experiment. The temperature inside the furnace was increased from room temperature (22 ℃) to 740 ℃ at an average ramp-up rate of 20 ℃/min. The power to the furnace was then turned off, and the furnace was allowed to cool down. When the temperature dropped to 400 ℃, the power was turned on again. The temperature was increased from 400 ℃ to 740 ℃. During the entire duration of the temperature-ramp experiment, the OFDR interrogator measured shifts in Rayleigh spectra along the length of the optical fiber with an update rate of 1 Hz. The thermocouple system measured temperature at a single position with an update rate of 1 Hz. Figure 2 shows measurements from both the fiber-optic and the thermocouple systems during the temperature-ramp experiment. The frequency shift and temperature measurements recorded during the first ramp-up (22 ℃ to 740 ℃) were used for the calibration. The frequency shift data was converted into temperature using a second-order polynomial fitting, as shown in Figure 2(a). The coefficients of the second-order polynomial (p1, p2, and p3) that relate frequency shift (F) to temperature (T) are provided in Figure 2(a). The same calibration coefficients were used to convert frequency shift measurements into temperature measurements for the two successive temperature ramp-down and ramp-up processes. The measurements recorded with the OFDR interrogator and thermocouple systems exhibited good agreement for the entire duration of the temperature-ramp experiment, as evident from Figure 2(b). The experiment not only provided calibration coefficients but also demonstrated the reliability of OFDR measurements, using a high-NA fiber as a sensing device, for temperatures up to 740 ℃.

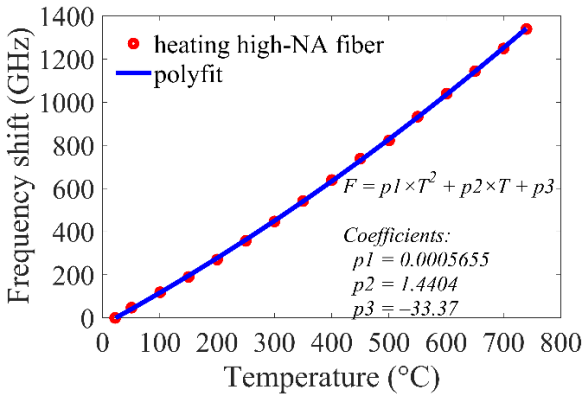

(a)

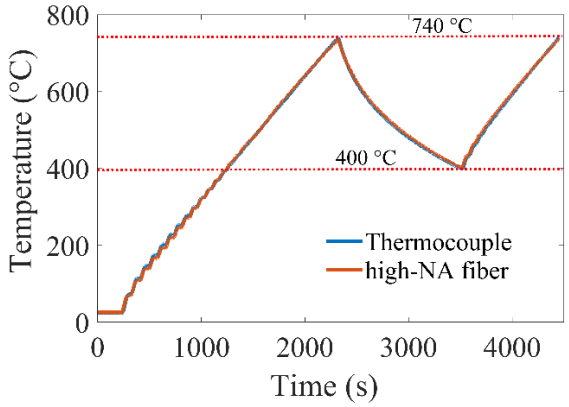

(b)

Figure 2. The responses of the fiber-optic and the thermocouple systems during temperature ramp-up and ramp-down processes. (a) A plot of the frequency shift response, recorded by the fiber-optic system, for various temperatures metered by the thermocouple placed in the furnace. Frequency shift data was converted into temperature data using a second-order polynomial fitting. F: frequency shift, T: temperature, p1, p2, and p3: coefficients of the second-order polynomial. (b) Fiber-optic and thermocouple temperature measurements during temperature ramp-up and ramp-down processes.

3.3. INSTRUMENTING A COPPER MOLD PLATE WITH OPTICAL FIBERS

A copper plate (100 mm × 50 mm × 12 mm thick) was used to machine a mold that was instrumented with optical fibers. The dimensions of the plate were selected so that the dip test could be conducted in a 200 lb induction furnace in a foundry laboratory. The

objective of the test was to generate 2D thermal maps of the mold plate in real-time using an embedded fiber-optic sensor during immersion of the mold into the molten metal and subsequent solidification of the metal shell against the mold surface. An optical fiber should maintain good thermal contact with the hot face to measure temperature variations at the surface of the mold. An optical fiber bonded to the surface of the mold can experience thermally-induced strains due to the mismatch of the coefficient of thermal expansions (CTEs) of the optical fiber (fused silica CTE: 0.55×10^{-6} /°C) and the material of the mold plate (copper CTE: 17×10^{-6} /°C). Therefore, the optical fiber should be thermally connected to, but mechanically decoupled from, the hot face of the mold. Moreover, an embedded fiber should minimally interfere with the heat flow inside the mold. An embedding scheme was devised to achieve the aforementioned objectives. Figure 3 shows a schematic of an EDM-machined (EDM: electrical discharge machining) copper mold plate and a photograph of the plate after instrumentation with an optical fiber. Twelve deep slots (each 350 μm wide) were machined longitudinally from the back face of the mold plate to within 1 mm of the hot face using wire EDM as shown in Figure 3(a). The separation between two neighboring slots was 2 mm. Figure 3(b) shows a photograph of the mold instrumented with an optical fiber. A high-NA single-mode optical fiber was used to instrument all twelve slots. The high macrobending loss-resistance of the high-NA fiber enabled the instrumentation of all twelve slots using a single continuous optical fiber with multiple return loops. For each slot, a section of the optical fiber was loosely placed at the base of the slot. The slot was backfilled with copper powder (325 mesh) up to a height of 2 mm from the base of the slot. The remaining space in the slot was filled by inserting a thin copper sheet (100 mm × 9 mm × 0.32 mm thick) into the slot. The use of thin machined

slots from the back face of the mold plate minimized interference with the hot face heat flow in the mold, providing a more uniform surface exposed to the molten metal. The deep slots ensured that the optical fiber close to the hot face allows the capture of rapid thermal events. The loose fiber surrounded by copper powder provided improved heat flow uniformity while ensuring that no thermally induced strain was transferred to the optical fiber from the copper mold plate as the mold plate was heated. The thin copper sheets, inserted into the slots, improved heat flow inside the mold.

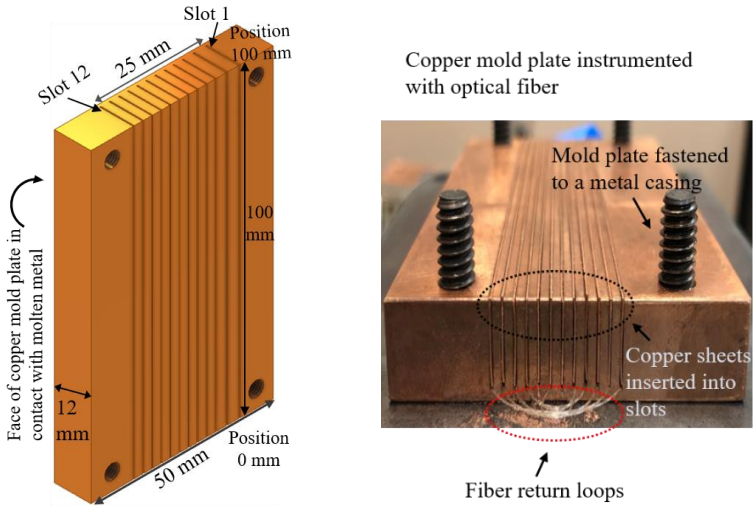

(a) (b)

Figure 3. A schematic of the EDM-machined copper mold plate and a photograph of the same after instrumentation with an optical fiber. (a) A schematic of the copper mold plate (100 mm × 50 mm × 12 mm) used in the dip test. Twelve slots, each 350 μm wide, were machined from the back face of the mold plate to within 1 mm of the front face. (b) A photograph of the instrumented mold plate. The slots on the copper mold plate were instrumented with a single continuous optical fiber configured with multiple return loops at both ends of the mold plate. The slots were backfilled with copper powder and copper sheets. The mold plate was fastened to a metal casing.

3.4. CASING FOR THE MOLD

A mild steel (AISI 1018 grade) casing was designed to protect the optical fiber loops and the copper mold plate's cold end from direct contact with the molten metal. Figure 4 includes a schematic and a photograph of the EDM machined copper mold plate housed in the metal casing. The casing consists of two parts, a 3 mm thick, 155 mm × 100 mm front plate to which the instrumented copper mold plate was fastened, and a 52 mm thick, 155 × 100 mm container that housed the return loops and the lead-out optical fiber. The fiber was then passed through a ¾-npt pipe and connected to the interrogator. With the inner wall of the test casing lined with an alumino-silicate ceramic fiber paper, heat transfer was predominantly confined to one direction only, from metal to the hot face of the mold. The steel casing was coated with an alcohol-based zircon wash to facilitate the easy recovery of the solidified shell.

3.5. THE TEST ASSEMBLY AND THE RBS SIGNAL FROM THE FIBER UNDER TEST

In order to keep the OFDR interrogator at a safe distance from the high-temperature environment of the induction furnace, a 4.3 m long lead-in standard SMF was used. The standard SMF was spliced to a 2.4 m long high-NA fiber using a fusion splicer (Fujikura 70S). The other end of the high-NA fiber was spliced to a 30 cm long coreless fiber to reduce reflections from the high-NA fiber’s end face. The copper mold plate was instrumented with the high-NA fiber, as discussed earlier in section III(C). Figure 5 shows the RBS signal obtained from the lead-in standard SMF and the high-NA fiber. The RBS signal was recorded after the mold was instrumented with the fiber.

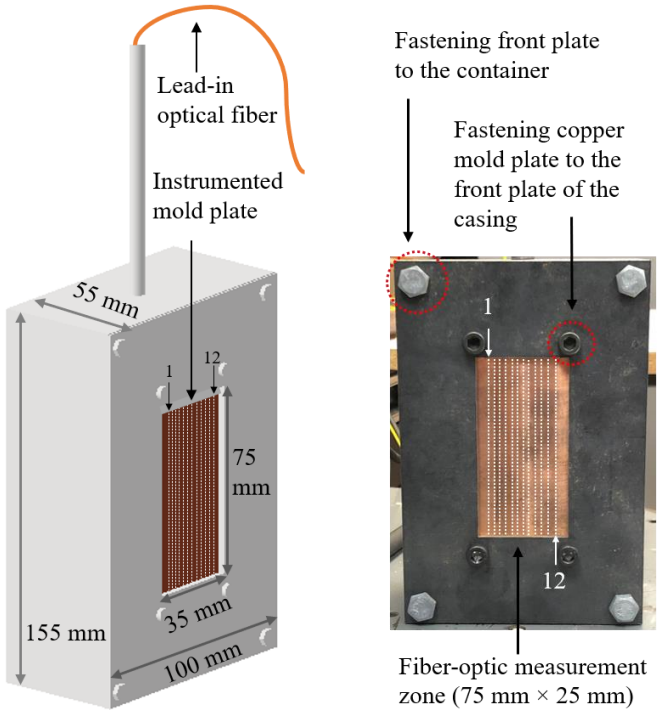

(a) (b)

Figure 4. A schematic and a photograph of the instrumented copper mold plate housed in a metal casing (a.k.a. the test paddle). (a) A schematic of the mold plate housed in a metal casing. The instrumented mold plate was attached to the front metal plate of the casing. The front plate was then fixed to the casing. The casing protected the back face of the mold plate and fiber loops from direct exposure to the molten metal during the dip test. Twelve white dotted lines represent the twelve embedded fiber sections. (b) A photograph of the front face of the metal casing mounted to the instrumented copper mold plate.

A higher dopant concentration in the core and improved capture fraction due to the high numerical aperture of the fiber may account for the ~6 dB enhancement in the RBS signal obtained from the fiber [44]. To instrument twelve slots using a single continuous high-NA fiber, eleven return loops of the fiber were configured. The bending radii of the fiber loops ranged from as large as 30 mm down to as small as 5 mm. It is evident from Figure 5 that the SNR for the looped high-NA fiber is better than the SNR of the straight lead-in standard SMF.

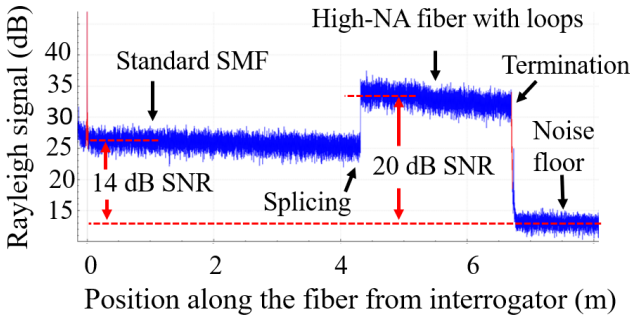

Figure 5. The relative intensity of the Rayleigh backscattering signal along the lead-in SMF and the embedded high-NA fiber. The low macrobending loss of the high-NA fiber ensured good signal strength despite having multiple permanent sharp bends in the fiber resulting from the embedding process.

4. THE DIP TEST

The dip test procedure involved induction melting of a grey cast iron charge (C 3.10%, Si 1.87%, Mn 0.5%, Cr 0.16%) in a 200 lb coreless induction furnace. The temperature of the melt was measured using a handheld temperature probe with a platinum-based thermocouple (Heraeus Digilance V). When the temperature of the melt was 1450 °C, the test paddle was slowly lowered into the melt crucible and held for 4 seconds before withdrawal. An iron shell was formed on the mold wall. Temperature measurements were performed continuously throughout the immersion and solidification process. The spatially-distributed temperatures along the length of the optical fiber were metered with a 0.65-mm spatial resolution. The measurements were recorded with an update rate of 25 Hz. The width of the mold plate, where temperature points were measured, was 25 mm. There were 1380 distinct temperature measurement points over an area of 75 mm × 25 mm. To the best of our knowledge, such a high-density thermal mapping scheme for a metal casting mold has not been reported previously. The high density of measurements provides

a very detailed thermal response of the mold as the mold transfers heat from the molten metal during solidification.

5. RESULTS AND DISCUSSION

Figure 6 shows a schematic of the test paddle used in the dip test and spatially distributed temperature profiles along embedded fiber sections. The machining and instrumentation of the mold plate, shown in Figure 6(a), was discussed in section III(C). Figure 6(b) shows a thermal map of the mold surface during the dip test (when the mold was fully immersed). The spatially distributed temperature measurements were used to generate thermal maps of the mold surface at 1 mm from the hot face where the fiber sections were embedded. Temperature values were sampled with 0.65 mm resolution along the y-axis (corresponding to the spatial resolution of the OFDR interrogator) and with 2 mm resolution along the x-axis (corresponding to the spacing between adjacent optical fiber sections). The thermal maps were generated by MATLAB R2018b using pseudocolor plots with bilinear interpolation, and the colors represent a range of temperatures. The jet color scheme with 1024 color levels was used to obtain smoother transitions between colors. Figure 6(c) shows spatially distributed temperature profiles along twelve fiber sections embedded in the mold plate. The temperature profiles are shown at four times during the dip test, labeled t1–t4. t1= 0 s: before immersing the mold into the molten metal; t2 = 1 s: when the mold was partially immersed into the molten metal; t3 = 3.5 s: when the mold was fully immersed; and t4 = 8 s: after the mold was taken out of the crucible with a metal shell solidified on the mold wall. Before the immersion, at time t1, all twelve

embedded fiber sections uniformly registered room temperature (~25 ℃). A temperature rise was observed during immersion, and a temperature gradient was also observed along the length of the mold. The lower part of the mold registered a higher temperature, while the upper part registered a lower temperature because the mold was partially immersed at that time. The temperature profiles along the embedded fiber sections exhibited a similar trend in the temperature gradients when the mold was fully immersed. The lower part was hotter than the upper part of the mold. Temperature gradients began to dissipate shortly after the mold was removed from the molten metal due to the redistribution of heat on the mold surface, as depicted by temperature profiles at time t4 = 8 s. The high spatial resolution (0.65 mm) and fast measurement rate (25 Hz) of the fiber-optic temperature measurement system made it possible to monitor a detailed thermal response of the mold during the immersion and solidification process. The information-rich thermal history of the mold provided useful insights into the casting process.

Figure 7 shows thermal maps of the mold surface at different time instances during the dip test. The thermal maps indicate that the temperature began increasing at the bottom of the mold plate, which agrees with the test procedure because the immersion into the molten metal started at the bottom of the test paddle mold plate. When the mold was fully immersed, the entire area of the mold showed a temperature rise. However, a significant temperature difference was observed between the lower and the upper parts of the mold. The heating rate of the mold was attributed to solidification kinetics and, subsequently, the solidified shell profile. The solidified shell morphology correlated well with the thermal profile, as regions with higher temperatures in the thermal profile corresponded to areas on the shell that were thicker.

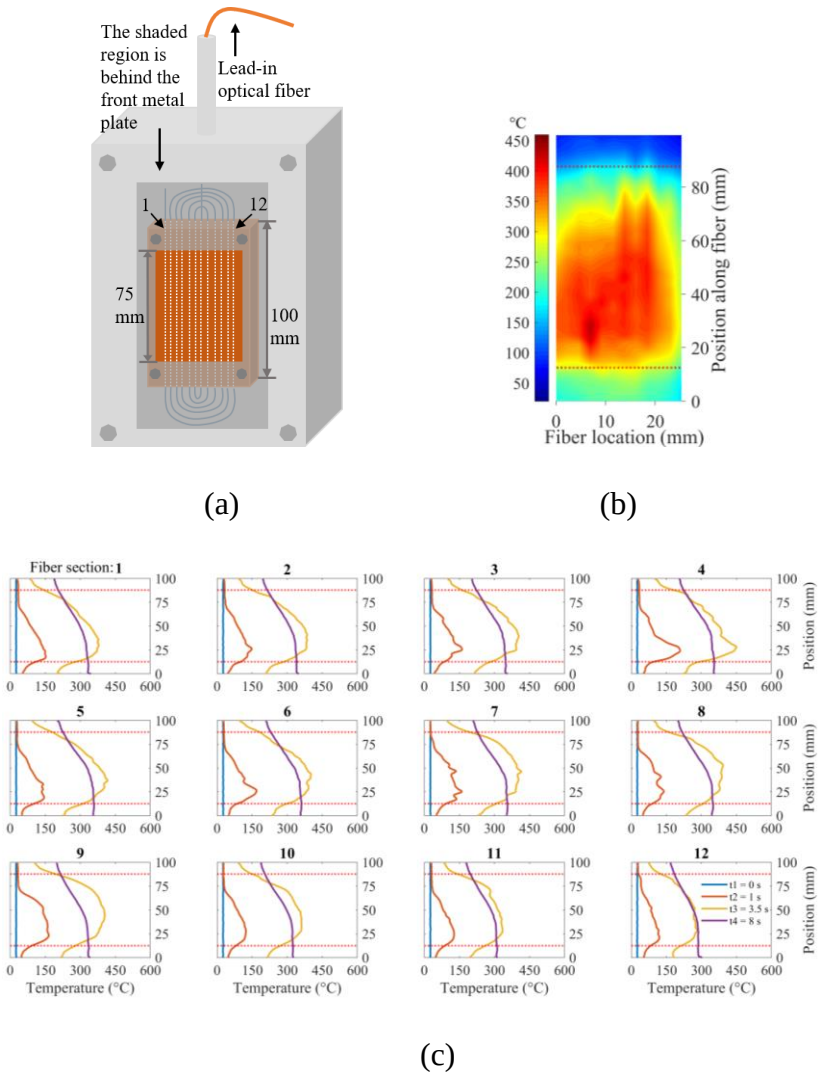

Figure 6. A schematic of the test paddle and spatially distributed temperature profiles along embedded optical fiber sections. (a) A schematic of the instrumented mold plate housed in a metal casing. The optical fiber sections embedded in the mold plate and optical fiber return loops at the top and bottom of the mold are shown. b) A thermal map of the mold plate during the dip test. The length between the two red dotted lines corresponds to the 75-mm long surface of the 100-mm long mold plate, which was exposed to the molten metal (c) Spatially-distributed temperature profiles along 12 adjacent embedded optical fiber sections at four instances of time during the immersion and solidification process. t1 = 0 s: a time before immersing the mold into the molten metal, t2 = 1 s: during immersion when the mold was partially immersed into the molten metal, t3 = 3.5 s: when the mold was fully immersed, t4 = 8 s: after the mold was taken out of the crucible with a shell solidified against the face of the mold. The graph labeled "Fiber section: **1**" shows temperature profiles along the left-most embedded optical fiber section (viewed from the top surface of the mold plate, which was exposed to the molten metal), and the graph labeled **12** corresponds to the right-most embedded optical fiber section.

The temperature profile suggests that the solidification of the metal shell was non-uniform, which agreed with direct observations of the shell thickness. The use of thermal maps in this manner will help identify areas where thinning of the shell may likely occur.

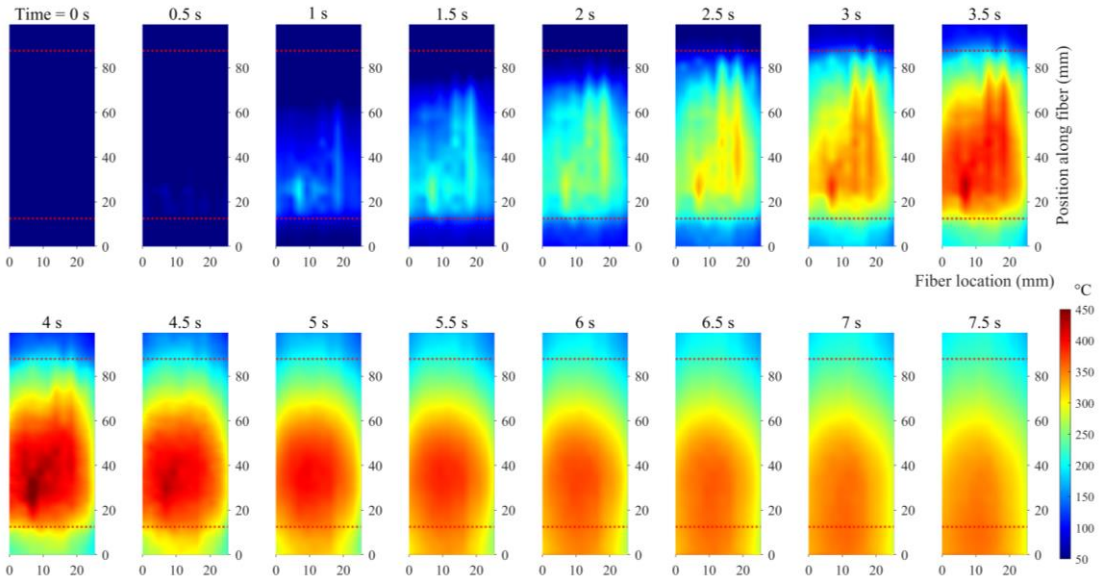

Figure 7. Thermal maps of the copper mold plate during the immersion and solidification process of a dip test. The immersion started at t = 0.5 s. At t = 2 s, the mold was fully immersed in the molten metal. The mold plate remained immersed for 4 seconds until t = 6 s. At t = 7.5 s, the mold was out of the crucible with a shell solidified against the face of the mold.

The generally higher temperature at the lower part of the mold was the result of the slightly longer residence time in the molten iron due to the finite speed of immersion into and withdrawal from the bath. The lower temperature at the top of the mold was due to its slightly shorter residence time in the molten iron bath. The low-temperature zone on the mold surface indicated a reduced heat flux from the shell to the mold. Another possible cause for the reduced heat flux in the upper part of the mold is the formation of an air gap between the shell and the mold surface during shell growth, caused by shell distortion. The

reduced heat flux resulted in reduced shell thickness, which could eventually lead to cast breakout. Figure 8 shows a spatial-temporal thermal map for one of the embedded fiber sections, the fiber section embedded in slot 6, numbered from the left of the mold. Slot 6 was close to the midplane of the mold. The spatially distributed temperature profile along the 75-mm length of the fiber (the length of the mold exposed to molten metal) is shown during the immersion of the mold and during solidification and cooling of the shell. The temperature rise from the bottom to the top of the mold during immersion is clearly visible. Moreover, the spatial-temporal profile illustrates that the temperature in the upper part remained lower than the temperature in the lower part of the mold. Similarly, spatial-temporal thermal profiles for the remaining eleven sections of the fiber can be obtained to investigate the thermal behavior of other zones of the mold.

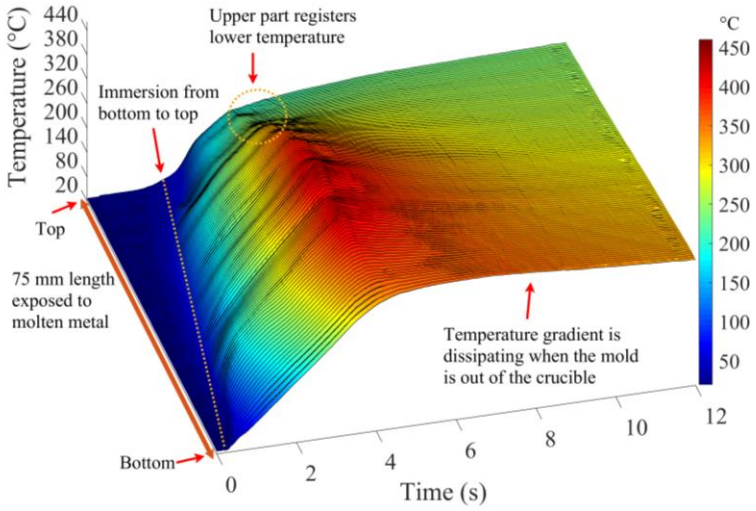

Figure 8. Spatially distributed temperature profile along one of the embedded fiber sections (the fiber section embedded in slot 6, numbered from the left of the mold) during the immersion and solidification process.

Another dip test was conducted in a steel bath using the same experimental setup. Thermal profiles of the mold plate were measured continuously throughout the immersion and solidification process. A steel shell (C 0.2%, Si 2.0%, Mn 0.07%, Al 0.08%) was formed on the mold wall. A complete 3D scan of the solidified shell was performed using a 40-µm point resolution blue light scanner (OptimScanTM-5M) to measure the thickness profile of the shell. The scanned data was processed in MATLAB R2019a to generate a thickness map of the shell. Figure 9 shows a photograph of the solidified shell, the thickness map of the shell, and a thermal map of the mold during the solidification process.

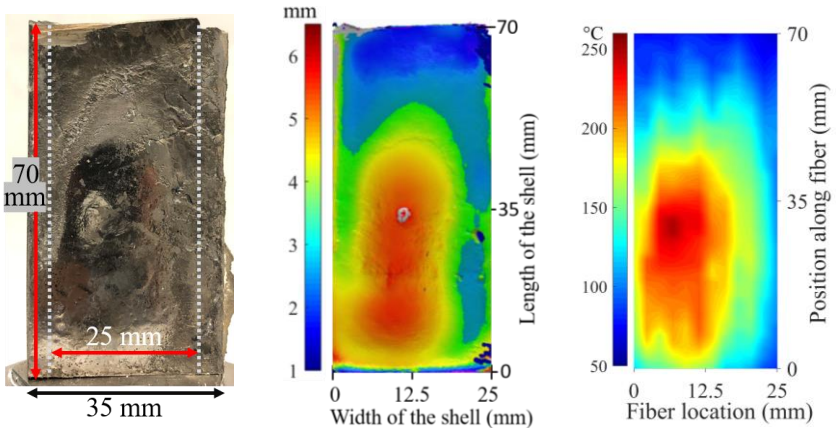

(a) (b) (c)

Figure 9. A side-by-side comparison of a photograph of the solidified steel shell, the thickness map of the shell, and a thermal map of the mold plate. (a) A photograph of the mold face side of the shell (70 mm × 35 mm). The photograph was flipped horizontally to make the orientation of the shell the same as the orientations of the thickness map of the shell and the thermal map of the mold. The width between the two white dotted lines is the 25-mm wide surface of the 35-mm wide shell, which corresponds to the 25-mm wide surface of the mold plate where fiber sections were embedded for temperature measurements. (b) Thickness map (millimeters) of the solidified steel shell. (c) A thermal map of the mold plate during solidification.

Figure 9(a) shows a photograph of the mold face side of the shell (70 mm × 35 mm). The width between the two white dotted lines is the 25-mm wide surface of the 35-mm wide shell, which corresponds to the 25-mm wide surface of the mold plate where fiber sections were embedded for temperature measurements. A good correlation was observed between the thickness map of the solidified shell (Figure 9(b)) and the thermal map of the mold (Figure 9(c)). The regions reporting higher temperatures in the thermal profile corresponded to areas on the shell that were thicker. The lower temperature regions on the mold surface corresponded to the thinner areas of the shell. The correlation between the thickness map of the solidified shell and the thermal map of the mold demonstrates that RBS-based fiber-optic temperature measurements are very useful for real-time thermal mapping of the caster mold.

6. CONCLUSION

We reported and demonstrated a method to embed Rayleigh backscattering-based (RBS-based) fiber-optic temperature sensors into a copper mold plate to generate thermal maps of the mold during the metal casting process. Deep slots were machined into the mold, using a wire EDM, from the back face of the mold to within 1 mm of the front face (hot face) to accommodate sensor installation into the mold plate. All slots were instrumented using a single continuous optical fiber with multiple return loops at both ends of the mold plate. A single optical fiber was used, providing for simple cable management and interrogation of the fiber sensor under test conditions. The instrumented mold plate was used to conduct a cast-iron dip test and a steel dip test in a 200 lb induction furnace.

Two-dimensional thermal maps of the mold plate were generated during the immersion of the mold into the crucible and the solidification of a metal shell against the mold wall. The localized and rapid temperature features observed for the mold wall were successfully mapped using a fiber-optic sensor that was embedded close to the mold surface (at a depth of 1 mm). RBS-based measurements were performed with a high spatial resolution (0.65 mm) and a fast measurement rate (25 Hz). The information obtained from the thermal maps provided valuable insights into the solidification behavior. The thickness map of the solidified steel shell was compared to a thermal map of the mold plate, and good correlations of features were observed between the two measurements. The dip test experiments demonstrated that RBS-based fiber-optic sensing is an effective method for real-time temperature monitoring of caster molds. Investigating the information-rich thermal response of the mold can be useful for improving the quality of the metal and the productivity of the casting process.

ACKNOWLEDGMENTS

This research was sponsored in-part by the Kent D. Peaslee Steel Manufacturing Research Center (PSMRC) at Missouri S&T and the Leonard Wood Institute (project LWI-2018-006) in cooperation with the U.S. Army Research Laboratory and was accomplished under Cooperative Agreement Number W911NF-14-2-0034.

REFERENCES

[1] B. G. Thomas, M. S. Jenkins, and R. B. Mahapatra, “Investigation of strand surface defects using mould instrumentation and modelling,” *Ironmak. Steelmak.*, vol. 31, no. 6, pp. 485–494, 2004.

[2] S. Carless, A. Kamperman, A. Westendorp, and J. Brockhoff, “Optimization of surface quality through mold thermal monitoring,” *Iron Steel Technol.*, vol. 8, no. 7, pp. 84–92, 2011.

[3] W. H. Emling and S. Dawson, “Mold instrumentation for breakout detection and control,” in *Steelmaking Conference Proceedings*, 1991, pp. 161–181.

[4] S. M. Cho *et al.*, “Measurement of Transient Meniscus Flow in Steel Continuous Casters and Effect of Electromagnetic Braking,” in *Sensors, Sampling, and Simulation for Process Control*, John Wiley and Sons, 2011, pp. 59–66.

[5] Q. He, Z. Su, Z. Xie, Z. Zhong, and Q. Yao, “A novel principle for molten steel level measurement in tundish by using temperature gradient,” *IEEE Trans. Instrum. Meas.*, vol. 66, no. 7, pp. 1809–1819, 2017.

[6] M. Sedén et al., “Development of Enhanced Mold Flow Control in Slab Casting”, Proceedings, SCANMET V, Luleå (2016).

[7] G. Xia *et al.*, “Investigation of mould thermal behaviour by means of mould instrumentation,” *Ironmak. Steelmak.*, vol. 31, no. 5, pp. 364–370, 2004.

[8] M. Suzuki et al, “Analysis of Heat Transfer and Solidifying Shell Deformation in Mold in High Speed Continuous Casting of Peritectic Medium Carbon Steels,” Steelmaking Proc., pp. 165–171, 1998.

[9] T. T. Natarajan, S. R. Story, T. J. Piccone, and K. D. Van Ness, “Peritectic Range Study Using Mold Thermocouple Data,” *AISTech 2017 Proc.*, no. 412, pp. 1645–1654, 2017.

[10] B. G. Thomas, M. A. Wells, and D. Li, “Monitoring Of Meniscus Thermal Phenomena with Thermocouples in Continuous Casting Of Steel,” in *Sensors, Sampling, and Simulation for Process Control*, John Wiley and Sons, 2011, pp. 119–126.

[11] I. Mazza, S. Miani, G. Schiavon, and S. Spagnul, “Real-time and Contactless Mold Thermal Monitoring: Improving Metallurgy, Quality and Productivity of Billets and Blooms.” *BHM Berg- und Hüttenmännische Monatshefte*, vol. 165, no. 1, pp. 11–18, 2020.

[12] R. Strąkowski, K. Pacholski, B. Więcek, R. Olbrycht, W. Wittchen, and M. Borecki, “Estimation of FeO content in the steel slag using infrared imaging and artificial neural network,” *Measurement*, vol. 117, pp. 380–389, Mar. 2018.

[13] R. Usamentiaga, D. F. Garcia, and J. M. Perez, “High-Speed Temperature Monitoring for Steel Strips Using Infrared Line Scanners,” *IEEE Trans. Ind. Appl.*, vol. 56, no. 3, pp. 3261–3271, 2020.

[14] B. G. Thomas, M. K. Okelman,. Implementation Of Temperature and Strain Micro-Sensors into a Casting Mold Surface. in Sensors, Sampling, and Simulation for Process Control (pp. 127–134). John Wiley and Sons. 2011.

[15] J. Wans, D. Lieftucht, C. Geerkens, M. Arzberger, and M. Reifferscheid, “HD mold - Caster assistance system to increase product quality,” *AISTech - Iron Steel Technol. Conf. Proc.*, vol. 2, no. May 2013, pp. 1385–1391, 2013.

[16] A. Krasilnikov *et al.*, “Online shell thickness calculation operating in a new fibre-optical based Mould Monitoring System,” *ICS 2012, 5th Int. Congr. Sci. Technol. Steelmak. Dresden, Ger*, pp. 1–9, October 2012.

[17] D. Lieftucht, M. Reifferscheid, T. Schramm, A. Krasilnikov, and D. Kirsch, “HD Mold – A New Fiber-Optical-Based Mold Monitoring System," *Iron and Steel Technology*. 10. 87-95, 2013.

[18] G. Hedin et al., “Exploring opportunities in mold temperature monitoring utilizing fiber Bragg gratings,” ScanMet V: *5th International conference on process development in iron and steelmaking*. June 2016.

[19] T. Spierings, A. Kamperman, H. Hengeveld, J. Kromhout, and E. Dekker, “Development and Application of Fiber Bragg Gratings for Slab Casting,” *AISTech 2017 Proc.*, no. May, pp. 1655–1664, 2017.

[20] C. Zhu, Y. Zhuang, B. Zhang, R. Muhammad, P. P. Wang, and J. Huang, “A Miniaturized Optical Fiber Tip High-Temperature Sensor Based on Concave-Shaped Fabry-Perot Cavity,” *IEEE Photonics Technol. Lett.*, vol. 31, no. 1, pp. 35–38, 2019.

[21] X. G. Li, Y. Zhao, L. Cai, and X. Zhou, “Measurement of magnetic field and temperature based on fiber-optic composite interferometer,” *IEEE Trans. Instrum. Meas.*, vol. 66, no. 7, pp. 1906–1911, 2017.

[22] C. Han, H. Ding, Q. Zhang, and C. Zhao, “Miniature Fizeau Interferometric Thermometer,” *IEEE Trans. Instrum. Meas.*, vol. 69, no. 11, pp. 9237–9242, 2020.

[23] R. Gassino, G. Perrone, and A. Vallan, “Temperature monitoring with fiber bragg grating sensors in nonuniform conditions,” *IEEE Trans. Instrum. Meas.*, vol. 69, no. 4, pp. 1336–1343, 2020.

[24] A. Ukil, H. Braendle, and P. Krippner, “Distributed temperature sensing: Review of technology and applications,” *IEEE Sensors Journal*, vol. 12, no. 5. pp. 885–892, 2012.

[25] C. Zhu, R. E. Gerald, and J. Huang, “Progress Toward Sapphire Optical Fiber Sensors for High-Temperature Applications,” *IEEE Trans. Instrum. Meas.*, vol. 69, no. 11, pp. 8639–8655, 2020.

[26] M. K. Barnoski and S. M. Jensen, “Fiber waveguides: a novel technique for investigating attenuation characteristics,” *Appl. Opt.*, vol. 15, no. 9, p. 2112, 1976.

[27] Y. Dong, H. Zhang, L. Chen, and X. Bao, “2 cm spatial-resolution and 2 km range Brillouin optical fiber sensor using a transient differential pulse pair,” *Appl. Opt.*, vol. 51, no. 9, pp. 1229–1235, Mar. 2012.

[28] Z. Yao, T. Mauldin, Z. Xu, G. Hefferman, and T. Wei, “An Integrated OFDR System Using Combined Swept-Laser Linearization and Phase Error Compensation,” *IEEE Trans. Instrum. Meas.*, vol. 70, 2021.

[29] G. M. Ma *et al.*, “High-Resolution Temperature Distribution Measurement of GIL Spacer Based on OFDR and Ultraweak FBGs,” *IEEE Trans. Instrum. Meas.*, vol. 69, no. 6, pp. 3866–3873, 2020.

[30] B. J. Soller, D. K. Gifford, M. S. Wolfe, and M. E. Froggatt, “High resolution optical frequency domain reflectometry for characterization of components and assemblies,” *Opt. Express*, vol. 13, no. 2, p. 666, 2005.

[31] Y. Du, S. Jothibasu, Y. Zhuang, C. Zhu, and J. Huang, “Unclonable Optical Fiber Identification Based on Rayleigh Backscattering Signatures,” *J. Light. Technol.*, vol. 35, no. 21, pp. 4634–4640, 2017.

[32] C. Zhu, Y. Zhuang, and Y. Chen, “Distributed fiber-optic pressure sensor based on Bourdon tubes metered by optical frequency-domain reflectometry,” *Opt. Eng.*, vol. 58, no. 07, p. 1, 2019.

[33] S. Jothibasu *et al.*, “Spatially continuous strain monitoring using distributed fiber optic sensors embedded in carbon fiber composites,” *Opt. Eng.*, vol. 58, no. 07, p. 1, 2019.

[34] M. Roman *et al.*, "A Spatially Distributed Fiber-Optic Temperature Sensor for Applications in the Steel Industry," *Sensors*, vol. 20, no. 14, p. 3900, Jul. 2020.

[35] Y. Du, Q. Yang, and J. Huang, "Soft Prosthetic Forefinger Tactile Sensing via a String of Intact Single Mode Optical Fiber," *IEEE Sens. J.*, vol. 17, no. 22, pp. 7455–7459, 2017.

[36] Y. Du, S. Jothibasu, Y. Zhuang, C. Zhu, and J. Huang, "Rayleigh backscattering based macrobending single mode fiber for distributed refractive index sensing," *Sensors Actuators, B Chem.*, vol. 248, pp. 346–350, 2017.

[37] Y. Du, Y. Chen, Y. Zhuang, C. Zhu, R. Gerald, and J. Huang, "A Uniform Strain Transfer Scheme for Accurate Distributed Optical Fiber Strain Measurements in Civil Structures," *Inventions*, vol. 3, no. 2, p. 30, 2018.

[38] S. Rizzolo *et al.*, "Vulnerability of OFDR-based distributed sensors to high γ-ray doses," *Opt. Express*, vol. 23, no. 15, p. 18997, 2015.

[39] S. Rizzolo *et al.*, "Real time monitoring of water level and temperature in storage fuel pools through optical fibre sensors," *Sci. Rep.*, vol. 7, no. 1, pp. 1–10, 2017.

[40] M. Roman, D. Balogun, R. E. Gerald II, L. Bartlett, J. Huang, and R. J. O'Malley, "Peritectic Behavior Detection in the Fe-C-Mn-Al-Si Steel System Using Fiber Optic Temperature Mapping," *AISTech - Iron Steel Technol. Conf. Proc.*, 2020.

[41] K. M. McCary, B. A. Wilson, A. Birri, and T. E. Blue, "Response of Distributed Fiber Optic Temperature Sensors to High-Temperature Step Transients," *IEEE Sens. J.*, vol. 18, no. 21, pp. 8755–8761, 2018.

[42] K. Naeem, Y. S. Kwon, Y. Chung, and I. B. Kwon, "Bend-Loss-Free Distributed Sensor Based on Rayleigh Backscattering in Ge-Doped-Core PCF," *IEEE Sens. J.*, vol. 18, no. 5, pp. 1903–1910, 2018.

[43] M. Roman, C. Zhu, R. J. O'Malley, R. E. Gerald, and J. Huang, "Distributed Fiber-Optic Sensing with Low Bending Loss Based on Thin-Core Fiber," *IEEE Sens. J.*, vol. 21, no. 6, pp. 7672–7680, 2021.

[44] P. S. Westbrook *et al.*, "Enhanced Optical Fiber for Distributed Acoustic Sensing beyond the Limits of Rayleigh Backscattering," *iScience*, vol. 23, no. 6, p. 101137, 2020.

SECTION

3. CONCLUSIONS AND RECOMMENDATIONS

3.1. CONCLUSIONS

In conclusion, Rayleigh backscattering-based (RBS-based) distributed fiber-optic sensors (DFOS) were investigated, developed, and deployed for various applications in the steel industry. The spatially continuous temperature measurements at sub-millimeter spatial resolution and at milliseconds sampling speeds provided useful insights into the steelmaking processes, which otherwise could not be achieved using conventional sensors. Fiber embedding methods were devised to achieve reliable temperature measurements by protecting optical fibers from external stresses, ensuring continuous thermal contact of optical fibers with the target surfaces, and eliminating thermally induced strains. The distributed measurement capability of the fiber-optic system was tested, in a series of experiments, in the Missouri S&T foundry laboratory. The silica optical fibers were directly immersed in molten aluminum to monitor aluminum solidification. The temperature profiles at the metal-mold interface were also recorded. Furthermore, a steel casting mold, with embedded fiber-optic sensors, was designed and developed. A compact copper mold plate was instrumented with a high bending-loss resistant thin-core optical fiber. A novel dip testing paddle was developed employing the instrumented mold plate and was used to perform dip tests for various steel compositions. The effects of non-uniform shell growth on the thermal history of the mold were investigated. The dip testing apparatus can be very effective to investigate various steel compositions in a lab setting.

The information-rich temperature measurements, combined with shell measurements, can assist in the development of advanced high-strength steels. The present study demonstrated that Rayleigh backscattering-based fiber-optic sensors can be transformative to the steel industry by enabling efficient process control, reducing energy and maintenance costs, improving the safety of equipment and workers, and enhancing the quality and yield of metal products.

3.2. RECOMMENDATIONS

We successfully demonstrated that RBS-based DFOS are very effective for temperature measurements in the steel industry. Although the maximum temperature measurement capability of an RBS-based fiber-optic system, employing unmodified single-mode optical fibers, is approximately 700–750 ℃, the sensors can still be very useful in metal casting processes. Various applications, where temperatures remain below the maximum measurable temperature of the RBS-based DFOS, can benefit greatly from continuously monitoring temperatures at high spatial resolution. For example, the aluminum sand casting experiment provided spatial-temporal temperature data that can be used to calculate local solidification time across the entire mold cavity. The local solidification time can be used to estimate the secondary dendrite arm spacing (SDAS) of the solidified metal, and consequently, the mechanical properties of castings can be predicted. Moreover, temperature gradients at the metal-mold interface during metal solidification can be used to quantify interfacial heat transfer. The experimental data can be useful for improving the accuracy of interfacial heat transfer models, which in turn will help design molding systems that will produce high-quality castings. The efforts are

underway to replicate sand mold experiments using permanent molds. The silica optical fibers employed in the RBS-based fiber-optic system cannot be directly exposed to molten steel for monitoring temperatures during steel solidification, unlike aluminum, because the melting temperature of steel is much higher than the maximum temperature measurement capability of the RBS-based fiber-optic system. However, silica optical fibers can still be very useful in steel casting processes. For example, as we demonstrated in the dissertation, optical fibers were embedded in the mold plate for real-time thermal mapping of the mold plate during steel casting. A novel dip testing paddle was developed employing the instrumented mold plate. The mold instrumentation method employing RBS-based DFOS can be scaled up to the continuous casting mold. The high-resolution sensors embedded in continuous casting mold can provide temperature data that can help detect shell thinning and crack formation. Besides being a quality control tool, the dip testing paddle can be useful for the investigation of the fundamental reactions occurring in a continuous casting mold. The ongoing research investigates various steel compositions using real-time thermal profiles of the mold. The dip testing method, which generates information-rich thermal maps of the mold, can assist in the development of advanced high-strength steels. Other potential applications for DFOS in the steel industry can be temperature measurements in refractory linings of furnace, ladle, and tundish. The strategically placed silica optical fibers can provide information on heat losses and refractory wear of furnace, ladle, and tundish.

We anticipate that our work will inspire researchers to expand the utilization of RBS-based DFOS to the aforementioned potential applications in the steel industry. We point out a few aspects of the RBS-based fiber-optic sensors that require more work to

facilitate the deployment of DFOS in various steelmaking settings and to improve the performance of the measurement system. One such aspect that requires researchers' attention is the fiber termination. In the RBS based OFDR system, one end of the optical fiber is connected to the interrogator. The other end of the fiber needs to be terminated to reduce reflections from the fiber's end face. The undesired reflection from the end face of an optical fiber interferes with the Rayleigh backscattering signals and degrades the signal-to-noise ratio (SNR) of the measurements. The fiber termination is usually achieved by splicing a coreless fiber to the fiber under test. Other methods include applying index matching gel at the end face of the fiber, making sharp loops in the optical fiber close to the end face, and splicing a special fiber to the fiber under test that can absorb light. However, all such methods require that the termination part of the fiber is kept outside the high-temperature environment because exposing termination to high temperatures can compromise the effectiveness of the termination. This requirement often poses challenges for the deployment of optical fibers in test configurations. Therefore, fiber termination methods that can effectively maintain low back reflection at high temperatures are highly desirable. The stability of RBS-based OFDR measurements at elevated temperatures is another area that requires attention. The stability of temperature measurements degrades at temperatures exceeding 700 ℃. The degradation is due to the smoothening effects of density fluctuations in optical fiber, which reduces the strength of RBS signals. Another possible cause for performance degradation is the diffusion of dopants at elevated temperatures. The dopant diffusion introduces drift in temperature measurements and degrades measurement accuracy. Heat treatments of optical fibers can partially solve the problem by annealing the fibers. The annealed fibers exhibit significantly low drifts at

elevated temperatures. However, fiber annealing does not help in improving the strength of RBS signals. The strength of RBS signals can be improved by artificially creating index modifications in optical fibers. Femtosecond laser irradiated index modifications have shown tremendous potential for high-temperature RBS-based measurements. The femtosecond laser-irradiated index modifications have higher stability at elevated temperatures compared to the naturally occurring fluctuations in the refractive index profile of optical fiber. By employing optical fibers with femtosecond laser-enhanced Rayleigh backscattering, the maximum temperature measurement capability of the RBS based OFDR system can be extended to temperatures beyond 750 C (maximum measurement capability employing unaltered fibers), which can open more opportunities in steelmaking processes.

BIBLIOGRAPHY

[1] "Energy Intensity of Major Steelmaking Units", AISI Steel Works Site, March 2017.

[2] https://www.automation.com/en-us/articles/december-2020/impacting-energy-through-smart-manufacturing. Accessed on October 23, 2021.

[3] S. Carless, A. Kamperman, A. Westendorp, and J. Brockhoff, "Optimization of surface quality through mold thermal monitoring," Iron Steel Technol., vol. 8, no. 7, pp. 84–92, 2011.

[4] G. Xia et al., "Investigation of mould thermal behaviour by means of mould instrumentation," Ironmak. Steelmak., vol. 31, no. 5, pp. 364–370, 2004.

[5] M. Suzuki et al, "Analysis of Heat Transfer and Solidifying Shell Deformation in Mold in High Speed Continuous Casting of Peritectic Medium Carbon Steels," Steelmaking Proc., pp. 165–171, 1998.

[6] T. T. Natarajan, S. R. Story, T. J. Piccone, and K. D. Van Ness, "Peritectic Range Study Using Mold Thermocouple Data," AISTech 2017 Proc., no. 412, pp. 1645–1654, 2017.

[7] B. G. Thomas, M. A. Wells, and D. Li, "Monitoring Of Meniscus Thermal Phenomena with Thermocouples in Continuous Casting Of Steel," in Sensors, Sampling, and Simulation for Process Control, John Wiley and Sons, 2011, pp. 119–126.

[8] R. Strąkowski, K. Pacholski, B. Więcek, R. Olbrycht, W. Wittchen, and M. Borecki, "Estimation of FeO content in the steel slag using infrared imaging and artificial neural network," Measurement, vol. 117, pp. 380–389, Mar. 2018.

[9] R. Usamentiaga, D. F. Garcia, and J. M. Perez, "High-Speed Temperature Monitoring for Steel Strips Using Infrared Line Scanners," IEEE Trans. Ind. Appl., vol. 56, no. 3, pp. 3261–3271, 2020.

[10] S. Jothibasu et al., "Spatially continuous strain monitoring using distributed fiber optic sensors embedded in carbon fiber composites," Opt. Eng., vol. 58, no. 07, p. 1, 2019.

[11] José Miguel López-Higuera, Luis Rodriguez Cobo, Antonio Quintela Incera, and Adolfo Cobo, "Fiber Optic Sensors in Structural Health Monitoring," J. Lightwave Technol. 29, 587-608 2011.

[12] Y. Zhuang, Y. Chen, C. Zhu, R. E. Gerald, Y. Tang, and J. Huang, "A High-Resolution 2-D Fiber Optic Inclinometer for Structural Health Monitoring Applications," IEEE Transactions on Instrumentation and Measurement, vol. 69, no. 9, pp. 6544-6555, 2020.

[13] C. Zhu, R. E. Gerald and J. Huang, "Metal-Organic Framework Materials Coupled to Optical Fibers for Chemical Sensing: A Review," in *IEEE Sensors Journal*, vol. 21, no. 18, pp. 19647-19661, 15 Sept.15, 2021, doi: 10.1109/JSEN.2021.3094092.

[14] Chen Zhu, Rex E. Gerald, Yizheng Chen, Jie Huang, Metal-organic framework portable chemical sensor, Sensors and Actuators B: Chemical, Volume 321, 2020, 128608, ISSN 0925-4005.

[15] Pospíšilová, Marie, Gabriela Kuncová, and Josef Trögl. "Fiber-Optic Chemical Sensors and Fiber-Optic Bio-Sensors" Sensors 2015, no. 10: 25208-25259.

[16] G. C. Kahandawa, J. Epaarachchi, H. Wang, and K. Lau, "Use of FBG sensors for SHM in aerospace structures," Photonic Sensors, vol. 2, no. 3, pp. 203-214, 2012.

[17] V. Latini, V. Striano, G. Coppola, and I. Rendina, "Fiber optic sensors system for high-temperature monitoring of aerospace structures," in Photonic Materials, Devices, and Applications II, 2007, vol. 6593: International Society for Optics and Photonics, p. 65930S.

[18] S. Minakuchi and N. Takeda, "Recent advancement in optical fiber sensing for aerospace composite structures," Photonic Sensors, vol. 3, no. 4, pp. 345-354, 2013.

[19] A. Dandridge and G. B. Cogdell, "Fiber optic sensors for navy applications," IEEE LCS, vol. 2, no. 1, pp. 81-89, 1991.

[20] Y. Zhuang et al., "Fiber optic sensor embedded smart helmet for real-time impact sensing and analysis through machine learning," Journal of neuroscience methods, vol. 351, p. 109073, 2021.

[21] A. Beisenova et al., “Multi-fiber distributed thermal profiling of minimally invasive thermal ablation with scattering-level multiplexing in MgO-doped fibers,” Biomed. Opt. Express, vol. 10, no. 3, p. 1282, 2019.

[22] R. Correia, S. James, S. W. Lee, S. P. Morgan, and S. Korposh, “Biomedical application of optical fibre sensors,” J. Opt. (United Kingdom), vol. 20, no. 7, 2018.

[23] P. Roriz, S. Silva, O. Frazão, and S. Novais, “Optical fiber temperature sensors and their biomedical applications,” Sensors (Switzerland), vol. 20, no. 7, 2020.

[24] C. Zhu, Y. Zhuang, B. Zhang, R. Muhammad, P. P. Wang, and J. Huang, “A Miniaturized Optical Fiber Tip High-Temperature Sensor Based on Concave-Shaped Fabry-Perot Cavity,” IEEE Photonics Technol. Lett., vol. 31, no. 1, pp. 35–38, 2019.

[25] X. G. Li, Y. Zhao, L. Cai, and X. Zhou, “Measurement of magnetic field and temperature based on fiber-optic composite interferometer,” IEEE Trans. Instrum. Meas., vol. 66, no. 7, pp. 1906–1911, 2017.

[26] C. Han, H. Ding, Q. Zhang, and C. Zhao, “Miniature Fizeau Interferometric Thermometer,” IEEE Trans. Instrum. Meas., vol. 69, no. 11, pp. 9237–9242, 2020.

[27] J. Huang, X. Lan, Y. Song, Y. Li, L. Hua, and H. Xiao, “Microwave interrogated sapphire fiber michelson interferometer for high temperature sensing,” IEEE Photonics Technol. Lett., vol. 27, no. 13, pp. 1398–1401, 2015.

[28] J. Hsu, W. Zheng, J. Chen, C. Lee and J. Horng, "Temperature Fiber Sensors Based on Mach–Zehnder Interferometer With Sturdy Structure," in *IEEE Sensors Journal*, vol. 15, no. 12, pp. 6995-7000, Dec. 2015, doi: 10.1109/JSEN.2015.2469670.

[29] K. Krakenes and K. Blotekjaer, "Comparison of fiber-optic Sagnac and Mach-Zehnder interferometers with respect to thermal processes in the fiber," in *Journal of Lightwave Technology*, vol. 13, no. 4, pp. 682-686, April 1995, doi: 10.1109/50.372481.

[30] Guan, B.-O.; Tam, H.Y.; Tao, X.-M.; Dong, X.-Y. Simultaneous strain and temperature measurement using a superstructure fiber Bragg grating. IEEE Photonics Technol. Lett. 2000, 12, 675–677.

[31] Zhang, B.; Kahrizi, M. High-Temperature Resistance Fiber Bragg Grating Temperature Sensor Fabrication. IEEE Sens. J. 2007, 7, 586–591.

[32] Chen Zhu, Dinesh Alla, and Jie Huang, "High-temperature stable FBGs fabricated by a point-by-point femtosecond laser inscription for multi-parameter sensing," OSA Continuum 4, 355-363 (2021)

[33] J. Wans, D. Lieftucht, C. Geerkens, M. Arzberger, and M. Reifferscheid, “HD mold - Caster assistance system to increase product quality,” AISTech - Iron Steel Technol. Conf. Proc., vol. 2, no. May 2013, pp. 1385–1391, 2013.

[34] A. Krasilnikov et al., “Online shell thickness calculation operating in a new fibre-optical based Mould Monitoring System,” ICS 2012, 5th Int. Congr. Sci. Technol. Steelmak. Dresden, Ger, pp. 1–9, October 2012.

[35] D. Lieftucht, M. Reifferscheid, T. Schramm, A. Krasilnikov, and D. Kirsch, “HD Mold – A New Fiber-Optical-Based Mold Monitoring System," Iron and Steel Technology. 10. 87-95, 2013.

[36] G. Hedin et al., “Exploring opportunities in mold temperature monitoring utilizing fiber Bragg gratings,” ScanMet V: 5th International conference on process development in iron and steelmaking. June 2016.

[37] M. K. Barnoski and S. M. Jensen, “Fiber waveguides: a novel technique for investigating attenuation characteristics,” Appl. Opt., vol. 15, no. 9, p. 2112, 1976.

[38] Y. Dong, H. Zhang, L. Chen, and X. Bao, “2 cm spatial-resolution and 2 km range Brillouin optical fiber sensor using a transient differential pulse pair,” Appl. Opt., vol. 51, no. 9, pp. 1229–1235, Mar. 2012.

[39] Z. Yao, T. Mauldin, Z. Xu, G. Hefferman, and T. Wei, “An Integrated OFDR System Using Combined Swept-Laser Linearization and Phase Error Compensation,” IEEE Trans. Instrum. Meas., vol. 70, 2021.

[40] B. J. Soller, D. K. Gifford, M. S. Wolfe, and M. E. Froggatt, “High resolution optical frequency domain reflectometry for characterization of components and assemblies,” Opt. Express, vol. 13, no. 2, p. 666, 2005.

[41] Y. Du, S. Jothibasu, Y. Zhuang, C. Zhu, and J. Huang, “Unclonable Optical Fiber Identification Based on Rayleigh Backscattering Signatures,” J. Light. Technol., vol. 35, no. 21, pp. 4634–4640, 2017.

[42] K. M. McCary, B. A. Wilson, A. Birri, and T. E. Blue, “Response of Distributed Fiber Optic Temperature Sensors to High-Temperature Step Transients,” IEEE Sens. J., vol. 18, no. 21, pp. 8755–8761, 2018.

[43] M. Roman et al., “A Spatially Distributed Fiber-Optic Temperature Sensor for Applications in the Steel Industry,” Sensors, vol. 20, no. 14, p. 3900, Jul. 2020.

[44] M. Roman, D. Balogun, R. E. Gerald II, L. Bartlett, J. Huang, and R. J. O’Malley, "Peritectic Behavior Detection in the Fe-C-Mn-Al-Si Steel System using Fiber Optic Temperature Mapping," Proceedings of the AISTech 2020 (2020, Cleveland, OH), pp. 822-833, Association for Iron & Steel Technology (AIST), Sep 2020.

[45] D. Balogun, M. Roman, R. E. Gerald II, L. Bartlett, J. Huang, and R. J. O’Malley, “A Fiber Optic Distributed Temperature Mapping Technique to Characterize Shell Solidification in Peritectic Grade Steels,” Proceedings of the AISTech 2021 (2021, Nashville, TN), pp. 471-479, Association for Iron & Steel Technology (AIST), June 2021.

[46] M. Roman, C. Zhu, R. J. O'Malley, R. E. Gerald, and J. Huang, "Distributed Fiber-Optic Sensing with Low Bending Loss Based on Thin-Core Fiber," IEEE Sens. J., vol. 21, no. 6, pp. 7672–7680, 2021.

[47] M. Roman, D. Balogun, C. Zhu, L. Bartlett, R. J. O'Malley, R. E. Gerald, and J. Huang, "Thermal Mapping of Metal Casting Mold using High Resolution Distributed Fiber-Optic Sensors," in *IEEE Transactions on Instrumentation and Measurement*, doi: 10.1109/TIM.2021.3121500.

[48] D. Balogun, M. Roman, R. E. Gerald, J. Huang, L. Bartlett, and R. O'Malley, "Shell Measurements and Mold Thermal Mapping Approach to Characterize Steel Shell Formation in Peritectic Grade Steels," Steel Res. Int., vol. 2100455, pp. 1–11, 2021.

VITA

Muhammad Roman was born in Khanpur, Pakistan. He completed his undergraduate program at the University of Engineering and Technology Peshawar, Pakistan in 2010 with a Bachelor of Science in Electrical Engineering. In 2011, he joined the University of Engineering and Technology Taxila (UET Taxila), Pakistan as a research scholar. He earned his Master of Science in Electrical Engineering from UET Taxila in 2013. He worked as a lecturer in the electrical engineering department at the Wah Engineering College and the COMSATS Institute of Information Technology, Wah Cantt, Pakistan prior to joining Dr. Jie Huang's Lightwave Technology Lab at Missouri University of Science and Technology (Missouri S&T) in 2017. He earned his Doctor of Philosophy in Electrical Engineering from Missouri S&T in May 2022.